U-RQR/65-2
Copy No. 231

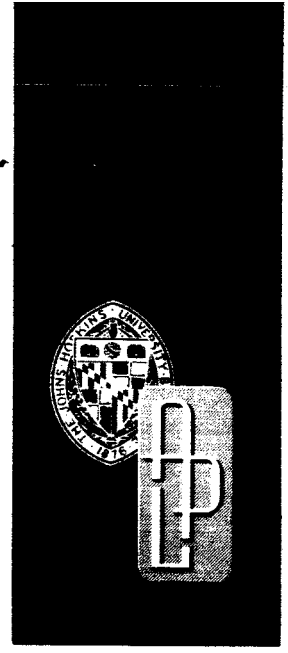

Quarterly Report

RESEARCH and DEVELOPMENT PROGRAMS

APRIL–JUNE 1965

Page VII/4 of this document, URQR/65-2
relates to NASA Contract R-21-009-006

THE JOHNS HOPKINS UNIVERSITY • APPLIED PHYSICS LABORATORY

U-RQR/65-2

Quarterly Report

RESEARCH and DEVELOPMENT PROGRAMS

APRIL—JUNE 1965

THE JOHNS HOPKINS UNIVERSITY ▪ APPLIED PHYSICS LABORATORY
8621 Georgia Avenue, Silver Spring, Maryland 20910

Operating under Contract NOw 62-0604-c, Bureau of Naval Weapons, Department of the Navy

FOREWORD

The Applied Physics Laboratory issues this Quarterly Report series to provide a useful record of its activities for the Bureau of Naval Weapons and the defense establishment. This series of reports is organized in six volumes by major Laboratory program and security classification, as follows:

Programs	Unclassified No.	Classified No.
Weapon Systems		
Surface Missile Systems		WQR/65-2A
Polaris Support		WQR/65-2B
Research and Development	U-RQR/65-2	C-RQR/65-2
Space Programs	U-SQR/65-2	C-SQR/65-2

This numbering system for the six basic volumes uses the following nomenclature. The designator for Quarterly Report, "QR," is preceded by a letter indicating the scope of the report (i.e., "W" for Weapon Systems, "R" for Research and Development, and "S" for Space Program. The scope designator is preceded by "C" or "U" to indicate "Classified" or "Unclassified," respectively, when both a classified and an unclassified volume are issued. Following the QR designator is the year indicator (e.g., "65") and then a number from 1 to 4 to designate the appropriate quarter of the calendar year. When a volume must be further subdivided to facilitate appropriate distribution, the quarter-designating number is followed by an arbitrary letter (A, B, C, ...) to distinguish between different subtitles.

The Quarterly Reports use the format originated for the APL/JHU Aeronautics Division Quarterly Review in which each topic is presented on a single sheet of paper and each is keyed to its proper program, technical instruction, Laboratory group, and supporting agency. Using the pages printed for the basic QR's, the Laboratory is able to prepare Division quarterlies and other special-purpose reports as required. Each such special-purpose report has its own scope indicator letter preceding the QR but uses a classification indicator only if it is divided into classified and unclassified volumes.

Lists approved by the Bureau of Naval Weapons for the initial distribution of these documents external to the Applied Physics Laboratory are printed in the back of each Quarterly Report volume. Distribution is made by the Distribution Project of the APL Technical Reports Group.

TABLE OF CONTENTS

Section II
POLARIS SUPPORT

Polaris High Impulse Booster and Thrust Augmentation--The feasibility of augmenting the thrust of first-stage rockets by supersonic afterburning of ram-collected air with fuel-rich exhaust gases is being investigated with studies based on the Polaris A3 and similar vehicles. Present studies are concerned with a 26-inch-diameter booster, as it has been suggested that five 26-inch-diameter missiles could be used in each missile tube aboard a submarine to increase potential distribution of weapons.

To provide data needed to design air inlets and other aerodynamic devices located at the aft end of the missile configuration, additional analysis was made of the boundary-layer characteristics on long cylindrical missiles at supersonic speeds, using boundary-layer profile measurements supplied by NASA (II/8).

Arc Research--Arc heater development is aimed at obtaining higher enthalpy operation to simulate more closely the environmental conditions encountered during re-entry at high Mach number. Forty-four runs were made with the all-copper arc; twenty were tests of ablation materials (II/11).

POLARIS SUPPORT 11/8
High Impulse Booster and Thrust Augmentation
P61BBA
Support: SP-001, Special Projects Office (Polaris)
R. H. Cramer January - June 1965

BOUNDARY LAYERS ON LONG CYLINDRICAL MISSILES AT SUPERSONIC SPEEDS

It is common practice to estimate boundary-layer characteristics on long cylindrical missile shapes by appeal to flat-plate theory and results, using the geometric distance measured from the nose as the length appropriate to insert in the Reynolds number formula. Undisturbed, free-stream conditions are often used as the engineering approximations for the velocity and kinematic viscosity which enter the Reynolds number determination. In order to execute a rational design for many aft-lying aerodynamic components pertinent to long slender missile configurations, it is patently clear that confirmation is required in regard to the accuracy and applicability of such crude engineering models for the real flow. In particular, it is highly desirable to know how to estimate the boundary-layer thickness at aft locations where an air inlet may be positioned. In fact, many fluid-mechanic devices, such as control surfaces or bleed-scoops, owe their effectiveness to the extent of the boundary layer and the state of the flow internal to and immediately outboard of the edge of the boundary-layer. Precise prediction of such boundary-layer characteristics, under realistic conditions, is often of crucial importance in the aerodynamic design of long slender missiles. Although theory and the few tests that have been made tend to indicate that there should be a minimum of discrepancy between flat-plate results and cylindrical-body findings, provided the nose is not too blunt, and provided the radius of the body of revolution is many times larger than the boundary-layer thickness, substantiation is needed to establish that the extensive body of information concerned with flat-plate boundary layers really is applicable to cylinders under commonly met circumstances.

SUMMARY AND CONCLUSIONS

Boundary-layer profiles have been measured by NASA (see Ref. 1) for 174 sets of conditions on three long slender-body configurations consisting of a circular cylinder preceded by (a) a sharp cone of 10° half angle, (b) a hemispherically blunted cone of 22.5° half angle, with radius of the hemisphere one-half of that of the cylinder, and (c) a full hemispherical head-cap to the cylinder. Four alternate types of trip were used to convert the boundary layer to the turbulent type (although all trips appear to give nearly the same action). The Mach numbers, M_∞, ranged from 1.44 to 4.55 and the Reynolds numbers, N_{Re}, (determined as mentioned above) ranged from 1.10 to 9.97 x 10^6. The flow outside of the boundary layer was found to be homentropic for the sharp cone, but the entropy gradient caused by the blunter noses was plainly evident. Typical profiles, representative of the three nose shapes, are shown in Fig. 1. It should be noted that the velocity-defect law (giving a straight line variation on a semi-log plot) holds for the boundary layer, regardless of nose shape and induced entropy gradients in the external field.

BACKGROUND AND CONCLUSIONS

The Ames Laboratory of NASA has provided APL with boundary-layer-profile measurements (Ref. 1) made at the aft end of a long cylinder (fineness ratio = 9) for adiabatic test conditions. The reservoir temperature was approximately 560°R in all cases, while the pressures ranged from 6 to 55 lb/in^2. Survey stations were located 9.5 and 11.1 inches downstream of the juncture between the nose and the cylinder. The local Reynolds number based on the geometric distance x, measured from the tip of the nose, and allowing the velocity and kinematic viscosity to have their free-stream values, ranged from 1.10 to 9.97 x 10^6, while the free-stream Mach number varied between 1.44 and 4.55. Three different nose shapes were used as described under Summary and Conclusions. Such a systematic series of boundary-layer measurements on cylinders in the Mach number and Reynolds number range of immediate interest to missile designers is not to be found elsewhere.

All the data followed the velocity-defect law, regardless of the influence of the entropy changes occasioned by the passage of the flow through the different kinds of nose-shock. The previous report (Ref. 2) on these profiles indicated the adherence to this law of three cases representative of the three different nose shapes; i.e., when plotted on a semi-log scale, all profiles, regardless of nose shape,

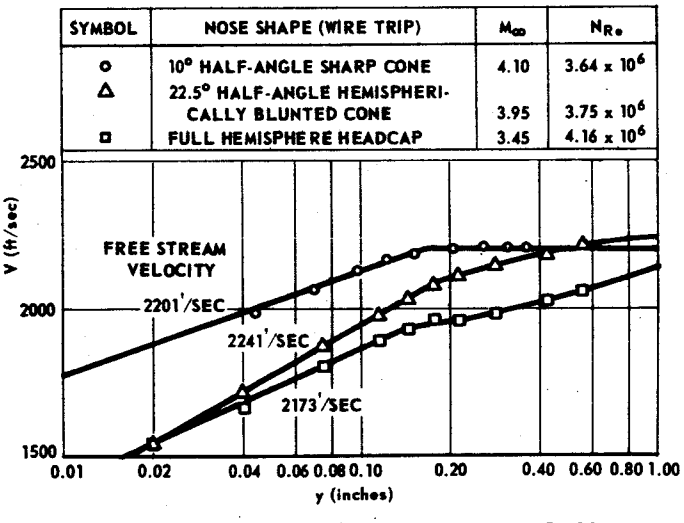

Fig. 1 Comparison of Turbulent Flow Velocity Profiles, Far Aft on Fineness-Ratio-9.0 Cylinder, with Variant Noses. (76537)

showed a straight line trend within the boundary layer. This illustration is repeated here now (Fig. 1) with correct numbers, to rectify a computational slip made previously (however, nothing needs to be altered in the numerical determination of the boundary layer thickness, δ, nor in the power-law profile index, n, as reported previously).

Since only a very small effort was devoted to this project recently, no significantly new results have been obtained. Routine analysis, however, has provided the values of n in the power-law profile defined as

$$U/U_e = (y/\delta)^{1/n}$$

where U is the velocity within the boundary layer, at the fractional distance y/δ from the wall, out toward the edge of the boundary layer, where the external velocity is U_e.

The complete assemblage of such values of n indicates that n increases as a function of M_∞ when Reynolds number is held constant; in fact, at an average Reynolds number and average M_∞ for these tests the value of n is about 8.8, so that, under such conditions, the following law holds approximately:

$$n = 4.44 + 1.53\ M_\infty$$

where the average value of M_∞ for these tests is about 2.87.

This behavior of n as a function of M_∞ for a constant Reynolds number is contrary to that predicted by D. A. Spence in Ref. 3, for a flat plate. The velocity profiles used by Spence to support his statement were obtained on the sidewalls of the NOL two-dimensional Tunnel No. 4 at hypersonic speeds ($5 < M_\infty < 8$). Recent data obtained by NASA (Ref. 4) indicate that boundary layers obtained on two-dimensional tunnel walls are far from being two-dimensional; thus, it appears unsafe to infer the trend of n from such tunnel wall measurements. The value of the present data, taken on an isolated long body, is enhanced because these boundary layers are free of cross-flow contamination, while curvature effects are practically nonexistent.

FUTURE PLANS

Boundary-layer thicknesses, δ, have been determined as described above, so attempts will be made to predict these thicknesses as functions of Mach number and Reynolds number, using the information on how n varies as a function of Mach number and Reynolds number. Such a correlation should not be difficult to establish because (see Ref. 5):

$$\delta/x = \left(\frac{(n+1)(n+2)}{2n} + 0.272\ M_\infty^2\right) C_F$$

where C_F is the average skin friction coefficient, and where adiabatic flow is assumed. The ratio of compressible to incompressible skin friction coefficient generally is considered to be unaffected by Reynolds number variation; consequently, a simple engineering result, for adiabatic flow conditions, as experienced in these tests, is (see Ref. 6):

$$C_F/C_{F_{inc}} = (1 + 0.128\ M_\infty^2)^{-0.67} .$$

Thus, a combination of these equations should provide the means for making a correlation of boundary layer thickness, δ, on a logical basis. The alternative, for engineering estimates, is to use an empirical result, obtained simply by plotting the measured thicknesses (for a selected M_∞) as a function of Reynolds number, as obtained in the present tests.

REFERENCES

1. Letter of June 29, 1964 from S. J. DeFrance of NASA to W. H. Avery of APL/JHU, transmitting unpublished velocity-profile measurements made in conjunction with research reported by D. M. Kuehn in NASA Technical Report R-117, 1961.
2. R. H. Cramer, "Boundary Layer Characteristics at Rear End of Long Cylindrical Configurations," Section II/11, Research and Development Programs Quarterly Report, October-December 1964, APL/JHU U-RQR/64-4.
3. D. A. Spence, "Velocity and Enthalpy Distributions in the Compressible Turbulent Boundary Layer on a Flat Plate," J. Fluid Mech., Vol. 8, 1960, pp. 368-387.
4. M. W. Jackson, K. R. Czarnecki, and W. J. Monta, Turbulent Skin Friction at High Reynolds Numbers and Low Supersonic Velocities, NASA TN D-2687, March 1965.
5. R. E. Wilson, "Viscosity Effects," Vol. 5, Section 13, Handbook of Supersonic Aerodynamics, NAVWEPS Report 1488 (to be published).
6. W. A. McIntosh, G. Hebert, and H. Dershin, The Effect of Aerodynamic Heating on Skin Friction Drag, Convair/Pomona TM-349-13 (issued in revised form as APL/JHU CM-971, 1 October 1959).

POLARIS SUPPORT 11/8
High Impulse Booster and Thrust Augmentation
P61BBA
Support: SP-001, Special Projects Office (Polaris)
R. H. Cramer January - June 1965

BOUNDARY LAYERS ON LONG CYLINDRICAL MISSILES AT SUPERSONIC SPEEDS

It is common practice to estimate boundary-layer characteristics on long cylindrical missile shapes by appeal to flat-plate theory and results, using the geometric distance measured from the nose as the length appropriate to insert in the Reynolds number formula. Undisturbed, free-stream conditions are often used as the engineering approximations for the velocity and kinematic viscosity which enter the Reynolds number determination. In order to execute a rational design for many aft-lying aerodynamic components pertinent to long slender missile configurations, it is patently clear that confirmation is required in regard to the accuracy and applicability of such crude engineering models for the real flow. In particular, it is highly desirable to know how to estimate the boundary-layer thickness at aft locations where an air inlet may be positioned. In fact, many fluid-mechanic devices, such as control surfaces or bleed-scoops, owe their effectiveness to the extent of the boundary layer and the state of the flow internal to and immediately outboard of the edge of the boundary-layer. Precise prediction of such boundary-layer characteristics, under realistic conditions, is often of crucial importance in the aerodynamic design of long slender missiles. Although theory and the few tests that have been made tend to indicate that there should be a minimum of discrepancy between flat-plate results and cylindrical-body findings, provided the nose is not too blunt, and provided the radius of the body of revolution is many times larger than the boundary-layer thickness, substantiation is needed to establish that the extensive body of information concerned with flat-plate boundary layers really is applicable to cylinders under commonly met circumstances.

SUMMARY AND CONCLUSIONS

Boundary-layer profiles have been measured by NASA (see Ref. 1) for 174 sets of conditions on three long slender-body configurations consisting of a circular cylinder preceded by (a) a sharp cone of 10° half angle, (b) a hemispherically blunted cone of 22.5° half angle, with radius of the hemisphere one-half of that of the cylinder, and (c) a full hemispherical head-cap to the cylinder. Four alternate types of trip were used to convert the boundary layer to the turbulent type (although all trips appear to give nearly the same action). The Mach numbers, M_∞, ranged from 1.44 to 4.55 and the Reynolds numbers, N_{Re}, (determined as mentioned above) ranged from 1.10 to 9.97 x 10^6. The flow outside of the boundary layer was found to be homentropic for the sharp cone, but the entropy gradient caused by the blunter noses was plainly evident. Typical profiles, representative of the three nose shapes, are shown in Fig. 1. It should be noted that the velocity-defect law (giving a straight line variation on a semi-log plot) holds for the boundary layer, regardless of nose shape and induced entropy gradients in the external field.

BACKGROUND AND CONCLUSIONS

The Ames Laboratory of NASA has provided APL with boundary-layer-profile measurements (Ref. 1) made at the aft end of a long cylinder (fineness ratio = 9) for adiabatic test conditions. The reservoir temperature was approximately 560°R in all cases, while the pressures ranged from 6 to 55 lb/in^2. Survey stations were located 9.5 and 11.1 inches downstream of the juncture between the nose and the cylinder. The local Reynolds number based on the geometric distance x, measured from the tip of the nose, and allowing the velocity and kinematic viscosity to have their free-stream values, ranged from 1.10 to 9.97 x 10^6, while the free-stream Mach number varied between 1.44 and 4.55. Three different nose shapes were used as described under Summary and Conclusions. Such a systematic series of boundary-layer measurements on cylinders in the Mach number and Reynolds number range of immediate interest to missile designers is not to be found elsewhere.

All the data followed the velocity-defect law, regardless of the influence of the entropy changes occasioned by the passage of the flow through the different kinds of nose-shock. The previous report (Ref. 2) on these profiles indicated the adherence to this law of three cases representative of the three different nose shapes; i.e., when plotted on a semi-log scale, all profiles, regardless of nose shape,

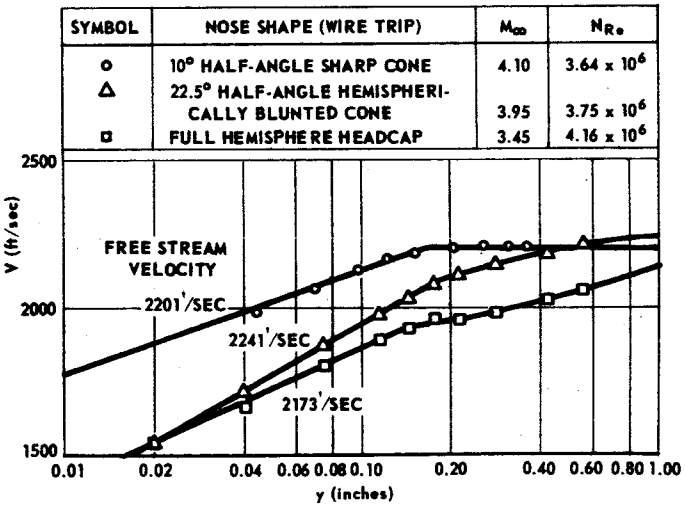

Fig. 1 Comparison of Turbulent Flow Velocity Profiles, Far Aft on Fineness-Ratio-9.0 Cylinder, with Variant Noses. (76537)

showed a straight line trend within the boundary layer. This illustration is repeated here now (Fig. 1) with correct numbers, to rectify a computational slip made previously (however, nothing needs to be altered in the numerical determination of the boundary layer thickness, δ, nor in the power-law profile index, n, as reported previously).

Since only a very small effort was devoted to this project recently, no significantly new results have been obtained. Routine analysis, however, has provided the values of n in the power-law profile defined as

$$U/U_e = (y/\delta)^{1/n}$$

where U is the velocity within the boundary layer, at the fractional distance y/δ from the wall, out toward the edge of the boundary layer, where the external velocity is U_e.

The complete assemblage of such values of n indicates that n increases as a function of M_∞ when Reynolds number is held constant; in fact, at an average Reynolds number and average M_∞ for these tests the value of n is about 8.8, so that, under such conditions, the following law holds approximately:

$$n = 4.44 + 1.53\ M_\infty$$

where the average value of M_∞ for these tests is about 2.87.

This behavior of n as a function of M_∞ for a constant Reynolds number is contrary to that predicted by D. A. Spence in Ref. 3, for a flat plate. The velocity profiles used by Spence to support his statement were obtained on the sidewalls of the NOL two-dimensional Tunnel No. 4 at hypersonic speeds ($5 < M_\infty < 8$). Recent data obtained by NASA (Ref. 4) indicate that boundary layers obtained on two-dimensional tunnel walls are far from being two-dimensional; thus, it appears unsafe to infer the trend of n from such tunnel wall measurements. The value of the present data, taken on an isolated long body, is enhanced because these boundary layers are free of cross-flow contamination, while curvature effects are practically nonexistent.

FUTURE PLANS

Boundary-layer thicknesses, δ, have been determined as described above, so attempts will be made to predict these thicknesses as functions of Mach number and Reynolds number, using the information on how n varies as a function of Mach number and Reynolds number. Such a correlation should not be difficult to establish because (see Ref. 5):

$$\delta/x = \left(\frac{(n+1)(n+2)}{2n} + 0.272\ M_\infty^2\right) C_F$$

where C_F is the average skin friction coefficient, and where adiabatic flow is assumed. The ratio of compressible to incompressible skin friction coefficient generally is considered to be unaffected by Reynolds number variation; consequently, a simple engineering result, for adiabatic flow conditions, as experienced in these tests, is (see Ref. 6):

$$C_F/C_{F_{inc}} = (1 + 0.128\ M_\infty^2)^{-0.67} .$$

Thus, a combination of these equations should provide the means for making a correlation of boundary layer thickness, δ, on a logical basis. The alternative, for engineering estimates, is to use an empirical result, obtained simply by plotting the measured thicknesses (for a selected M_∞) as a function of Reynolds number, as obtained in the present tests.

REFERENCES

1. Letter of June 29, 1964 from S. J. DeFrance of NASA to W. H. Avery of APL/JHU, transmitting unpublished velocity-profile measurements made in conjunction with research reported by D. M. Kuehn in NASA Technical Report R-117, 1961.
2. R. H. Cramer, "Boundary Layer Characteristics at Rear End of Long Cylindrical Configurations," Section II/11, Research and Development Programs Quarterly Report, October-December 1964, APL/JHU U-RQR/64-4.
3. D. A. Spence, "Velocity and Enthalpy Distributions in the Compressible Turbulent Boundary Layer on a Flat Plate," J. Fluid Mech., Vol. 8, 1960, pp. 368-387.
4. M. W. Jackson, K. R. Czarnecki, and W. J. Monta, Turbulent Skin Friction at High Reynolds Numbers and Low Supersonic Velocities, NASA TN D-2687, March 1965.
5. R. E. Wilson, "Viscosity Effects," Vol. 5, Section 13, Handbook of Supersonic Aerodynamics, NAVWEPS Report 1488 (to be published).
6. W. A. McIntosh, G. Hebert, and H. Dershin, The Effect of Aerodynamic Heating on Skin Friction Drag, Convair/Pomona TM-349-13 (issued in revised form as APL/JHU CM-971, 1 October 1959).

POLARIS SUPPORT 11/11
Arc Research P61BPF
Support: SP-001, Special Projects Office (Polaris)
E. A. Bunt
January - June 1965

ARC RESEARCH

This report covers that part of the continuing arc heater development which is now directed towards obtaining higher enthalpy operation in order to more nearly simulate the environmental conditions encountered in reentry at high Mach number.

SUMMARY AND CONCLUSIONS

All-Copper Arc Running--The first runs were made on this unit, designated Arc XII (to a total of 44, of which the latter 20 were Polaris tests referred to below). Reliability expectations have been borne out, necessary design changes being relatively few. In comparison to the performance of steel cased arcs, the most significantly different features of operation are, firstly, a new V-i characteristic, which intersects the old at about 13.9 kA. Since this new characteristic is nearly flat, at least over a range 8<i<32 kA, stability is much improved in the light of Kaufmann's criterion (Ref. 1)

$$\partial V/\partial i\big|_{arc} + R > 0 ,$$

where R is the slope of the load line. This is attributed to the greater rigidity of the double-overlap form of electrodes. Secondly, a further operating improvement resides in the use of parallel connections to these electrodes in order to avoid causing the arc column to surmount a voltage barrier (associated with high erosion) at the oncoming limb of the gaps.

Polaris Tests--A program of testing ablation materials in a sonic turbulent duct coupled to Arc XII was undertaken in conjunction with the Lockheed Missiles and Space Division and is approximately half completed. The test duct is similar to that used in the previous set of tests (see Aeronautics Quarterly, July-September 1962, Arc Research, for photograph of equipment). For these tests the arc unit was equipped with a special starting device; 'skirts' were added to the bases of the electrode supports to shield the insulators from arc radiation; and the inside of the unit was coated with zirconia deposited on nickel. Testing requirements were (a) high shear stress and (b) enthalpy in excess of 3000 Btu/lb (as measured by heat balance), in that order. Table I lists the data obtained, the results of the longer runs also being shown on Fig. 1.

High Enthalpy Considerations--Further consideration has been given to the requirements attending high enthalpy operation (Ref. 2). In addition, five runs were made on a modified Arc III unit (now designated Arc X) at approximately constant values of input power/mass flow to check the proportional reduction of heat losses below those of larger units (Ref. 3). However, the fact that the typical efficiency was only slightly greater than for the large arc unit led to a consideration of the connection between efficiency and rotational velocity.

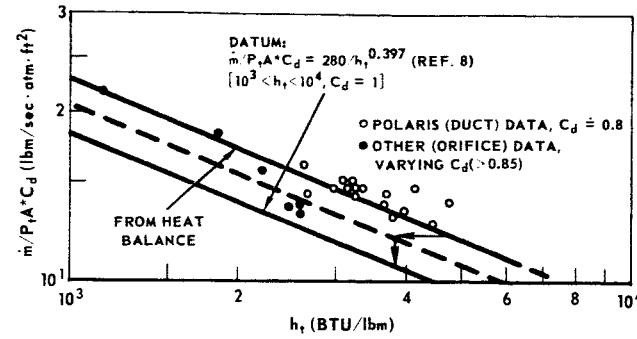

Fig. 1 Enthalpy Data. (76513)

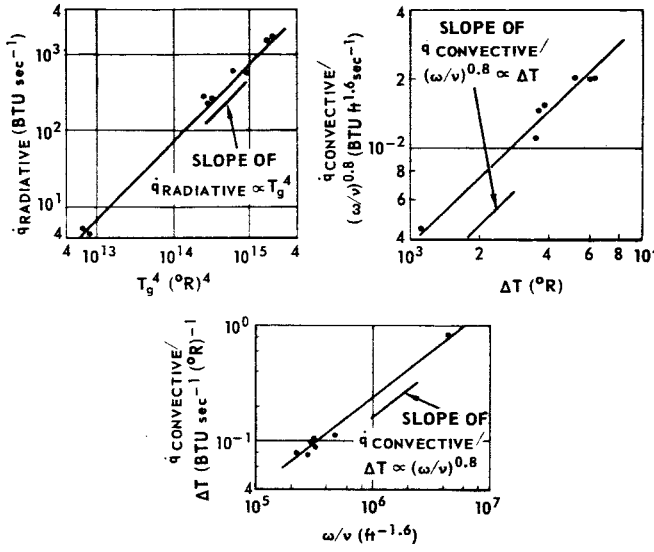

Fig. 2 Certain Solutions for Proportion of Radiative and Convective Flux for Copper Arc Body. (76514)

FUTURE PLANS

These include: (a) completion of Polaris ablation tests, (b) further low mass flow (high enthalpy) runs in Arc XII, (c) operation of Arc XII at maximum pressure (aided, if need be, by series inductance), (d) operation of multiple electrode systems in Arc XII (in anticipation of eventual power augmentation), and (e) operation of a restricted-arc high-enthalpy device to determine the maximum possible nonrotated arc current and the minimum individual ballast for arcs running in parallel.

BACKGROUND

In the light of earlier arc experience, a DC arc unit was designed to serve as a heater for a Mach 7 to 10 propulsion tunnel. As the laboratory pressure, power, and voltage limits have progressively been raised, an extension of arc capabilities has been sought in order to meet the requirements of the supporting research program.

PROGRESS DURING QUARTER

Distribution of Wall Heat Flux Between Convective and Radiative Forms--This distribution is important not only from the point of view of the efficiency of operation of present units but also because it has a strong bearing on the design of higher enthalpy units, particularly since the chamber gases radiate much more strongly than air uncontaminated by electrode materials. An attempt has therefore been made to distinguish between convective (c) and radiative (r) losses by solving for

Table I

Arc Parameters Used in Polaris Ablation Tests

Date	Run Number	$\dot{m}$ (lbm/sec)	P_t (psia)	i (amps)	V (volts)	Power (MW)	Run time, t (sec)	Heat Loss (Btu/sec)	Total Enthalpy (Btu/lbm)	Eff. (percent)	Duct Opening (in^2)	Remarks
5/19/65	25 - 1P	0.65	175	12,900	405	5.23	8	3137	3124	36.6	0.625	Calibration
5/21/65	26 - 2P	0.309	81	8,660	325	2.81	8	776	2634	29.1	0.625	"
5/21/65	27 - 3P	0.308	85	9,480	338	3.20	12	2079	3244	31.6	0.625	"
5/24/65	28 - 4P	0.303	190	8,300	413	3.43	-	1861	-	-	0.625	Highest pressure+
		0.303	62.5	10,000	295	2.98	3	1861	3324	34.2	-	End of test
5/24/65	29 - 5P	0.299	43	10,800	250	2.70	5	1711	2964	33.2	1.25	
5/24/65	30 - 6P	0.305	87.5	11,420	312	3.57	-	2406	3314	28.8	0.625	Highest pressure
		0.305	71	11,920	273	3.26	15	2406	2366	22.2	-	End of ablation
5/24/65	31 - 7P	0.307	90	14,340	300	4.30	-	2979	3694	26.9	0.625	Highest pressure
		0.307	72.5	15,000	265	3.97	14	2979	2669	20.8	-	End of ablation
5/24/65	32 - 8P	0.307	86	14,440	285	4.12	15	2998	3094	23.3	0.625	
5/24/65	33 - 9P	0.308	85	14,460	285	4.12	7	2818	3674	28.0	0.625	
5/24/65	34 -10P	0.306	90	14,240	288	4.10	12	2940	3224	24.4	0.625	
5/26/65	35 -11P	0.292	94	14,240	325	4.63	-	3020	3794	26.2	0.625	Highest pressure
		0.292	73	14,960	275	4.12	15	3020	3174	22.7	-	End of ablation
5/26/65	36 -12P	0.293	86	14,420	310	4.48	-	3102	4014	26.9	0.625	Highest pressure
		0.293	81.5	14,680	300	4.41	9	3102	3804	25.8	-	End of ablation
5/26/65	37 -13P	0.291	81.5	14,240	300	4.27	25	3146	3194	22.1	0.625	
5/26/65	38 -14P	0.595	88	14,080	333	4.69	20	2939	2664	34.0	0.625x	
5/26/65	39 -15P	0.304	94	13,820	318	4.40	-	3103	3634	25.6	0.625	Highest pressure
		0.304	78.5	14,240	295	4.20	10	3103	3024	22.1	-	End of ablation
6/1/65	40 -16P	0.305	87.5	13,920	322.5	4.49	-	3008	4114	29.1	0.625	Highest pressure
		0.305	75.5	14,500	290	4.21	14	3008	3331	24.5	-	End of ablation
6/1/65	41 -17P	0.296	93	14,120	310	4.38	-	3006	3985	27.5	0.625	Highest pressure
		0.296	75	14,680	283	4.15	15	3006	3273	23.7	-	End of ablation
6/3/65	41 -18P	0.294	97.5	13,640	350	4.77	-	3252	4454	28.13	0.625	Highest pressure
		0.294	76.0	14,200	305	4.33	15	3252	3025	20.78	-	End of ablation
6/3/65	42 -19P	0.292	88.5	14,000	350	4.90	-	3280	4799	29.39	0.625	Highest pressure
		0.292	78.5	14,340	305	4.37	11	3280	3090	20.89		End of ablation

+Model (cork) dislodged, causing temporary blockage of exit duct.

xModel (boron nitride) dislodged at t = 1 second, leaving opening of 1.25 in^2.

first-power heat flux dependence on temperature difference with the walls, and then by comparing the former with a vortex model of gas behavior. Writing equations for all runs, m, and surfaces, n, for which a heat flux measurement is available:

$$\dot{q}_{1n} = x_r f_r (T_1)_n + x_c f_c (T_1)_n$$
$$\vdots \qquad \vdots \qquad \vdots$$
$$q_{mn} = x_f f_r (T_m)_n + x_c f_c (T_m)_n ,$$

where $f_r(T) = T_g^4$, $f_c(T) = (T_g - T_w)(\omega/\nu)^{0.8}$

$x_r = 2\sigma V (\epsilon/\ell) A_n/A_{total}$, and

x_c = constant $(Pr)^{0.33}$, the constant taking into account the geometry of the particular surface.

Results of runs for which a solution has so far been worked out have been plotted in Fig. 2.

Polaris Tests--Although undertaken for the purpose of testing ablation models under specified conditions, these runs have provided valuable data on arc operation at mass flows of ~ 0.3 pps. To suppress convective losses, rotation rates were held down by keeping currents below 14 kA. In Fig. 1, a standard enthalpy curve (C_d = 1) (Ref. 4) has been inserted to illustrate the degree to which the enthalpies derived from the heat balance may be high. The use of this curve is valuable in setting arc operating points and in determining design characteristics of new arcs. Data points in Fig. 1 were calculated using various cold flow values of discharge coefficients, and are seen to lie above the datum enthalpy curve. The discrepancy between these curves may be resolved if the following is taken into consideration: (a) the measured losses are undoubtedly minimal, hence the true enthalpy values should be shifted to an arbitrary curve (shown dashed in Fig. 1); (b) the values of C_d used were 'cold' values, while 'hot' values are expected to be greater. The departure from the datum curve is thus a measure of uncertainty in the 'hot' value of C_d which, if taken into account, resolves the discrepancy.

REFERENCES

1. J. D. Cobine, Gaseous Conductors, New York, Dover Publications, 1958, p. 208.
2. E. A. Bunt, "Further Considerations Related to the Design of a High Enthalpy Arc Unit," APL/JHU BPF-65-44, 14 May 1965.
3. E. A. Bunt, "Summary of Arc X Runs to date (3/29/65 through 4/23/65)," APL/JHU BPF-65-41, 7 May 1965.
4. W. Winovich, On the Equilibrium Sonic-Flow Method for Evaluating Elecric-Arc Air Heater Performance, NASA TN D-2132, March 1964.
5. E. A. Bunt, "Similarity Considerations Applied to the Transition from Normal Rising Flow to Full Flow in Bell-Mouthed Intakes," to be published by J. of the Institute of Civil Engineers, London.
6. E. A. Bunt, "Alternative Settings for Arc Runs in TC 2," APL/JHU BPF-65-18, 8 March 1965.

Section III
EXPLORATORY DEVELOPMENT

Landing Force Support Weapon (LFSW)--A mobile semi-trailer van has been fitted out as an operations center for the SIGS/Sergeant flight test series (III/3).

Adaptive Systems Design and Analysis--A digital simulation of the boundary-tracking optical perception system has been evaluated and some resultant design changes initiated (III/7).

Airframe Structures - Hypersonic Flight--An analysis has been made of the various thermal stress components that arise in radomes as a result of aerodynamic heating (III/8a). Studies of the transient deformation of a titanium alloy under rapidly changing conditions of stress and temperature indicate that the actual strain lags behind predicted values during such periods (III/8b).

Aeroelastic Research and Development--Studies of the frequencies of free vibration of elastic structures and structural elements were continued, with emphasis on determining the effectiveness of lower bound calculation techniques (III/9).

Thermal Studies--Use of a temperature-difference method for obtaining convective heat transfer approximations has resulted in significant errors at high temperatures. To estimate the magnitude of the error to be expected, a comparison was made between results using a temperature-difference method and an enthalpy-difference method for computing convective heat transfer on a flat plate (III/10).

Radome Structures--The study to define the environmental limitations of the three basic radome materials, Pyroceram 9696, fused silica, and aluminum for four bands (S,C,X, and K) was continued (III/11a). Techniques for computing thermal stresses in laminated radomes have been reviewed; the method based on concentric thick-walled-cylinder theory was selected as the most appropriate, and it is being programmed for machine computation (III/11b).

Research and Development in Masers--A new flux melt process for the preparation of iron-doped sapphire single crystals has been evaluated, and construction of two new furnaces has been started (III/12).

Flame Attenuation Studies--While the available literature is being searched for relevant flame-attenuation data, APL has also conducted experiments to measure changes in the levels of C- and X-band signals propagating through the exhaust of a rocket motor proposed for use in the Standard Missile (III/14).

Thin Film Microelectronics--The continuous-life-test results on thin film transistors indicate that the semiconductor-dielectric-interface parameters must be better understood before stable devices of this type can be built (III/15a). An automatic thermal pulser for trimming thin-film resistors to specified tolerances has been fabricated, and a precision resistor probe for use with the pulser has been designed (III/15b). One direct-coupled operational amplifier has been built and placed in operation; others are currently being manufactured (III/15c). A new technique has been developed for reducing the encroachment that occurs during evaporation mask electroforming (III/15d). Several microelectronic circuits contracted from General Electric were received and tested (III/15e).

Semiconductor Microelectronics--The first volume of the Microelectronics Engineering Handbook is scheduled for printing during July (III/16a). Work toward the development of a semiconductor microelectronic frequency divider using micropower circuitry is continuing (III/16b).

Radiation Damage Studies--Studies have been made of the effects of radiation on insulated-gate, thin-film, cadmium selenide transistors (III/17).

Advanced Warhead Supporting Research--In the analysis of guidance and fuzing, an attempt was made to improve the relevance of effectiveness analysis by reviewing the performance of guidance and warhead fuzing systems of the Terrier, Talos, and Tartar missiles, using data obtained during missile test firings. The limitations of the information gathering techniques preclude obtaining satisfactory descriptions of guidance and fuzing error functions from this source (III/19a). Exploding wires are being considered for use as initiators of intermediate and secondary explosives. Experiments have been planned to study the shock waves from exploding wires (III/19e). Long exploding wires are being considered as a means of line initiation of explosives to avoid the use of sensitive explosives as initiators, achieve directional explosive patterns, and generally improve initiation and detonation of explosive warheads. Experiments are under way to determine the amount of energy required to just melt and also to just vaporize copper wires of various lengths (III/19f).

Adaptive Stabilization Computer--A new procedure has been developed for predicting an unknown stationary process (III/23).

RESEARCH AND EXPLORATORY DEVELOPMENT III/3
LFSW System Studies A22BMT
Support: RM-2 (BuWeps)
D. M. Michaud
April - June 1965

SIGS MOBILE OPERATION AND SUPPORT CENTER

Certain operational and handling difficulties which became evident during preparations for the March flight test, resulted in the decision to integrate all SIGS support equipment into a semi-trailer to serve as a mobile operation center for SIGS/Sergeant tests (Fig. 1). The SIGS support van contains all SIGS support consoles, a SIGS flight test package (SIGS mounted in sergeant warhead) on a specially designed pneumatic dolly, cable reels to stow three 600 foot cables, and working and office space. The forward section of the trailer was partitioned off and equipped with a communication network which serves as SIGS operations and flight control center. The intent was to be as self sufficient as possible and provide the capability of moving from one location to another with minimum time and effort.

SUMMARY

The van used for this purpose is 319 inches long, 96 inches wide, and 93 inches high. The floor plan showing the installed equipment is presented in Fig. 2. It is equipped with air conditioners, heaters, and florescent lighting. The trailer was delivered to APL in early April and by mid-May SIGS operations were being conducted from the van after the following modifications and provisions had been incorporated:

1. Reworked the air conditioners and provided a "squirrel cage" fan for compressor cooling to decrease noise level. Further soundproofing was provided by completely enclosing all air conditioning units.
2. Partitioned off the forward section of the van for an operation and flight control center which provides a desk, file, and communication center.
3. Modified all fluorescent lighting to operate on 60 cps.
4. Installed 60 and 400 cycle power fusing and distribution.
5. Installed and shock mounted all of SIGS support consoles:
   a. Alignment Console (Norden built).
   b. Instrument Console and Fire Control Computer (APL built).
   c. Power Supply Console (APL built).
   d. Monitor Console (APL built), which contains a digital/analog clock for time correlating the data gathered.
6. Installed three cable reels to stow external cables while in transit.
7. Designed, fabricated, and installed a 1 ton crane capable of loading and unloading the SIGS flight test package and dolly.
8. Designed and fabricated a special four wheel pneumatic dolly for handling the SIGS flight test package.
9. Designed, fabricated, and installed a communication system consisting of speakers, headsets, and a "master control" with a microphone capable of providing voice communication among four stations up to 500 feet.

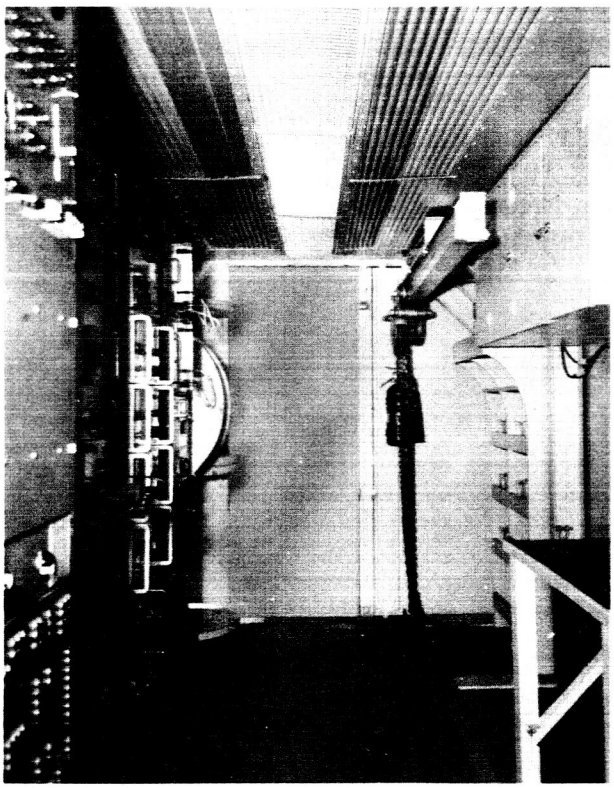

Fig. 1 SIGS Mobile Support Van. (76558)

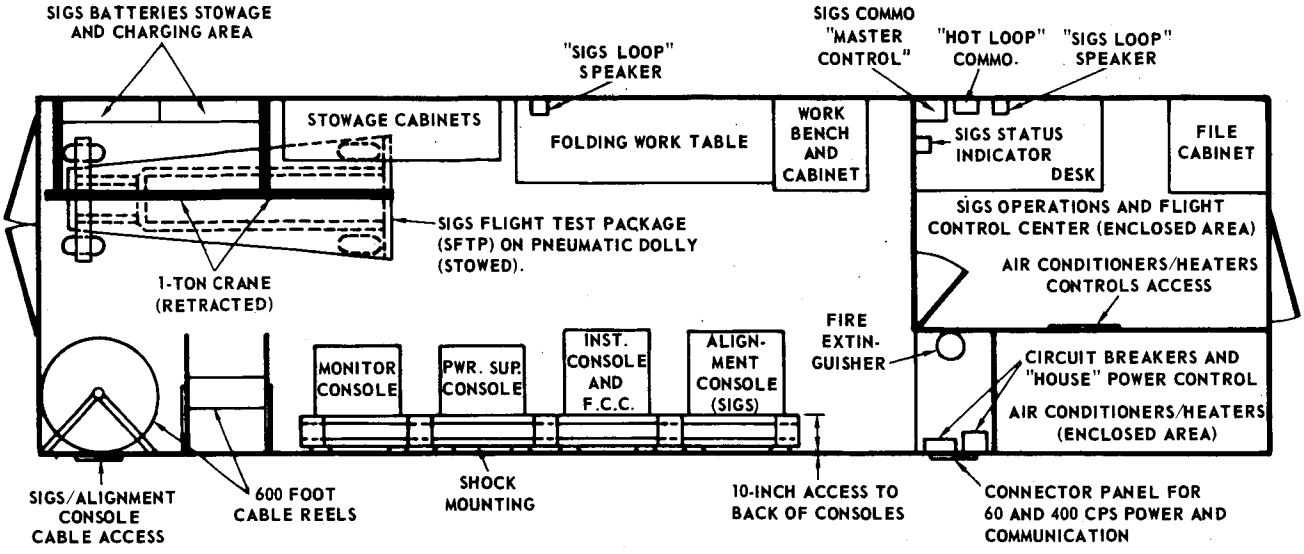

Fig. 2 Top View of SIGS Support Van. (76559)

FUTURE PLANS

The van has thus far successfully supported SIGS operations at APL and Sperry Utah in Salt Lake City, Utah. Future plans for the SIGS support van are to support a SIGS flight aboard a Sergeant missile at WSMR in July.

BACKGROUND

The requirements for a SIGS support van became evident as a result of operations that took place in February and March of this year at Sperry Utah and WSMR. In late March, it was decided to conduct a major proportion of the next flight preparation work at APL. Because of the schedule and number of places different phases of the operation would take place, it was decided that a self contained, mobile unit containing SIGS and all support hardware would be very desirable. This van satisfies the above-mentioned requirements. Setting up the van upon arrival at a site is relatively simple, consisting only of hooking up van prime power, and unreeling and connecting the three 600-foot cables between the SIGS flight test package and the SIGS alignment console.

RESEARCH AND EXPLORATORY DEVELOPMENT 111/7
Adaptive Systems Design and Analysis A32CLM
Support: RMGA (BuWeps)
H. R. Bittner
April - June 1965

ADAPTIVE SYSTEMS

The adaptive mechanisms program is one of research directed toward improved methods of data processing with special emphasis on use of techniques found in living organisms.

SUMMARY

All experimental development work has been concentrated on the boundary tracking optical perception system. The solid state resolver mentioned in the previous report has been reduced to practice as a single quadrant resolver. An adequate video signal has been achieved, and video processing circuitry is being developed to accumulate the first moment of lighted area around the two axes of the video raster. These moments will be used as rotational commands for the solid state resolver. The resolver will, in turn, rotate the raster until the moments of lighted area are nulled.

Information from the digital computer simulation of the boundary tracking process has been received, and evaluated. The conclusions form the basis for some system design changes that are being initiated.

In the sequence recognition network portion of the system, a basic network element has been developed that is not sensitive to the time spacing of sequential events. Time sensitivity was the shortcoming of the first design, and further development was continued. This basic network element has been tested and accepted as a functional standard to be used in the system. Circuit design considerations are being made to simplify the hardware requirement and maintain the standard performance of the element.

FUTURE PLANS

During the next quarter, experimental development of a number of the basic network elements connected to form some simple sequence recognition networks will be pursued. A digital computer simulation of sequence recognition networks will be continued. The purpose of this simulation is to study the criteria proposed for sequence recognition with the intent of optimizing the number of network elements required to recognize various patterns.

Continuing efforts on the boundary tracking system will include development of video processing circuitry and the logic circuitry necessary to recycle the single quadrant raster resolver. A logic technique for translating the video raster has been proposed, and the feasibility of using this technique will be considered.

BACKGROUND

Boundary Tracking Optical-Perception System--In the previous report, mention was made of a solid state resolver technique to be used to combine the deflection voltages that rotate the video raster. During this reporting period, this method of raster rotation has been reduced to practice for a single quadrant made up of eight characteristic angles. Thirty-two angular positions will be obtained by recycling the "single quadrant" resolver. Using this solid state resolver requires switching and summing deflection coil voltages of positive and/or negative polarities. These deflection voltages were large in amplitude owing to the deflection coil time constants, and switching of these bipolar voltages became a definite limitation. The decision was made to decrease the raster line rate from 20,000 lines per second to 2000 lines per second in order to allow lower amplitude deflection voltages to be used. This alteration reduced the amount of circuitry to be used for switching and summing the deflection voltages within the solid state resolver. The reduction in raster line rate also increased the average pattern recognition time by an unfavorable factor of ten. Plans are being made to speed up this time by using fewer raster frames for processing the video signal into rotation and/or translation commands.

The deflection circuitry has been reduced to practice, and a lower focus field intensity has been determined for the lower raster line rate (2000 lines per second). Adequate video signal has been achieved, and circuit design considerations are being worked out for the video processing section of the system. In this section, first moments of lighted area about axes parallel and perpendicular to the raster lines must be computed from the video signal. These moments will be used as feedback to the single quadrant resolver and to the logic that calls for translation of the video raster with respect to the object boundary.

A digital computer simulation of the boundary tracking process is near completion. A set of criteria for translation and rotation has been selected which makes the chance of losing acquisition low and provides sufficient data for identification of the pattern most of the time. Of eleven patterns tested, all can be identified with reliabilities of 74 to 100. Seven of these patterns can be identified for size scalings of one-half size to full size of the sensitive area of the vidicon mosaic. Five of these identifications have reliabilities close to 100 percent, the other two being 85 and 92 percent. The remaining four pat-

terns were identified at maximum size scaling with reliabilities of 74, 80, 92 and 100 percent. It was found that tracking is simplified if rotation and translation of the video raster are allowed simultaneously, and if rotation by increments larger than 11.25° are used to null the larger moments. These techniques are being considered as part of the system design.

During this reporting period, a basic network element has been developed that is nonsensitive to time spacing of events. Time-spacing independence was achieved by using a three-bit up-down counter as a memory device to accumulate preceding event stimulation. This method provides eight levels of input information to which a different width output pulse of standard amplitude is assigned. Six of these basic network elements have been fabricated to be used in the development of basic sequence recognition networks. A digital computer simulation of sequence recognition networks is being pursued for the purpose of optimizing the number of basic network elements needed in recognizing a given sequence of events. This computer simulation, which is based on a simplified representation of the basic network element, will also be used to test the criteria set up for sequence recognition. It has been recognized that if the number of basic network elements required to recognize a sequence can not be minimized, then the number of active components and size of these basic elements will be an objectionably large part of the system. This possibility has encouraged further development of the basic network element to include a simplified circuit design and maintain all of the features of the standard element now in use.

RESEARCH AND EXPLORATORY DEVELOPMENT 111/8a
Airframe Structures - Hypersonic Flight A33BBE
Support: RMGA (BuWeps)
M. B. Tate
April - June 1965

RADOME NOSECAP THERMAL STRESSES

Because it furnishes the initial conditions that play such an important role in the overall behavior of a radome, the radome nosecap is being studied as part of the investigation of thermal stresses in radomes. The principal structural questions around the tip are concerned with stress concentration, body restraints that affect subsequent parts of the radome, and the removal of analytical discontinuities that distort numerical results.

SUMMARY

Component thermal inputs were analyzed and reported in Refs. 1 to 9 inclusive. Definitions for dimensions and displacements are shown in Fig. 1, and typical results are plotted in Figs. 2 and 3. The orthogonal components of stress are denoted by σ_R, σ_ψ, σ_θ, and the displacements by u and w. Their positive directions are shown in Figs. 1 and 3. To obtain nondimensional curves, the results are plotted as the ratios σ_R/σ_o, σ_ψ/σ_o, σ_θ/σ_o, u/u_{no}, and w/u_{no}, where $\sigma_o = E\epsilon_o$ and $u_{no} = R_n\epsilon_o$ with E being the tensile modulus of elasticity (psi) and ϵ_o the thermal expansion at the nose (in/in).

It is necessary to obtain a synthesis of these solutions in conjunction with the results for the radome wall to determine the interaction between the two parts. The effects vary continuously along the span to the joint between the radome wall and the missile body, which imposes further restraint that must be evaluated in order to compute the critical stress and deformation governing the usable strength of the radome.

FUTURE PLANS

It is planned to combine the solutions thus far obtained with those that describe the wall and body-joint structural behavior. In this way, the stresses at any point can be examined and the maxima ascertained to provide design criteria as well as means to review strength and displacement requirements.

BACKGROUND

The high temperatures and thermal gradients to which guided-missile radomes are exposed have proved to be a continuing problem in radome design and strength assessment. Both theoretical and experimental programs have been proposed or are under way in efforts to meet the recurring need as faster missiles and larger vehicles enter the development phase, or as altered missions and new operational requirements are devised for existing weapons.

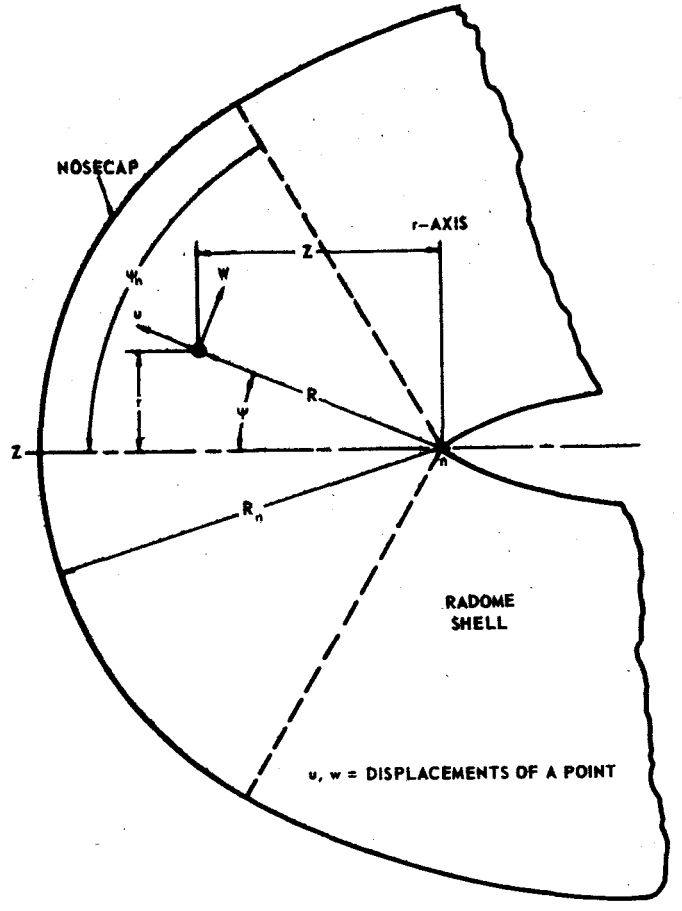

Fig. 1 Nosecap Dimensions. (76515)

DISCUSSION

In the study of stresses induced by intensive heat that changes considerably along the length of a radome owing to aerodynamic factors, it was found that several solutions are needed in order to define adequately the arbitrary temperature variations that must be included.

The contribution that changes through the thickness without lengthwise variation is examined in Ref. 1; the classical solution for axial symmetry is described in Ref. 2.

The temperature variation along the radius of any cross section is treated in Ref. 3,

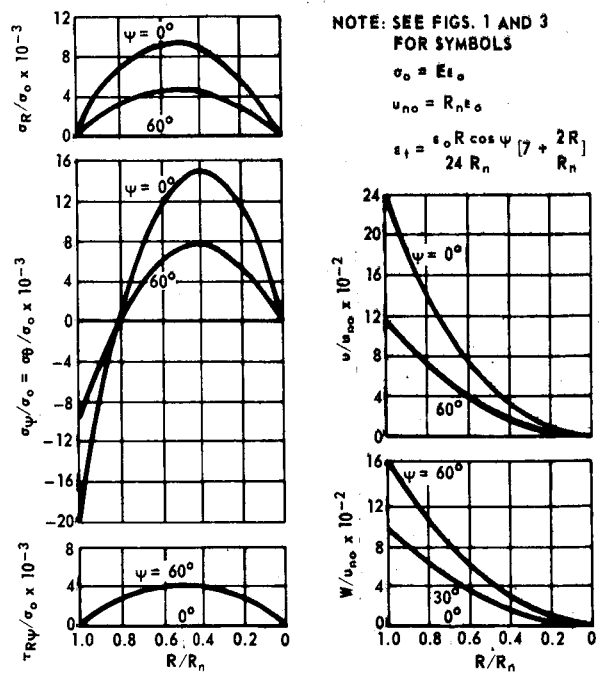

Fig. 2 Ratios of Normal and Shear Stresses and Displacements. (76516)

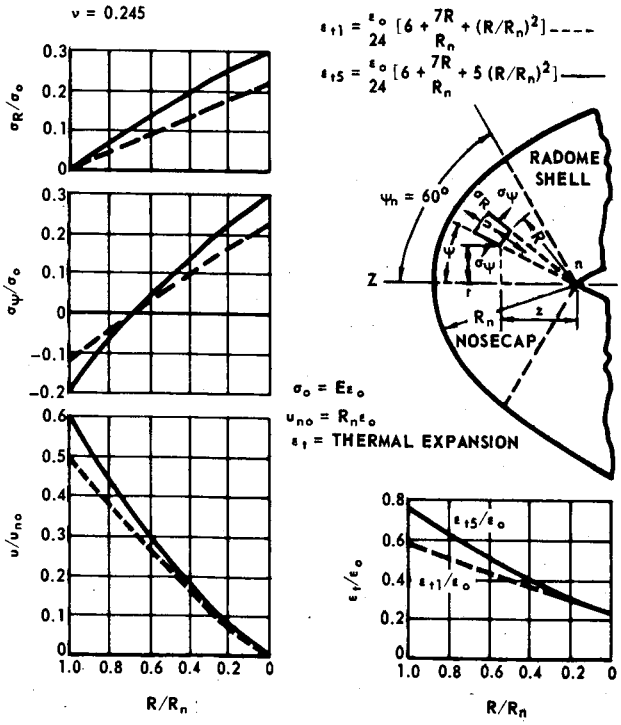

Fig. 3 Comparison of Stresses and Displacements. (76517)

while the case when the longitudinal stresses are paramount is dealt with in Ref. 4. A self-contained solution is found in Ref. 5 for distributions that vary in any fashion through the thickness and have a cosine variation along the span.

The problem that presents the greatest analytical difficulty is approached with the error-collocation method in Ref. 6. Exact solutions were later developed for this problem in Refs. 7 and 8. The first of these (Ref. 7) is numerically easy to apply in the first half of the angular range (between 0° and 45°), whereas the second one (Ref. 8) is convenient for numerical work in the second half (from 45° to 90°).

Reference 9 was derived to include definition of the causative thermal expansion within the formulas for stresses and displacements. This solution also is self-contained, and two expansions were compared graphically in the report. These results are shown here in Fig. 3.

REFERENCES

1. M. B. Tate, "Radially Symmetric Thermal Stresses in a Radome Nosecap" (Unclassified), APL/JHU EM-3950, 1965.
2. M. B. Tate, "Axially Symmetric Thermal Stresses in a Radome Nosecap" (Unclassified), APL/JHU EM-3951, 1965.
3. M. B. Tate, "Cross-Sectionally Symmetric Thermal Stresses in a Radome Nosecap" (Unclassified), APL/JHU EM-3953, 1965.
4. M. B. Tate, "Cylindrically Symmetric Thermal Stresses in a Radome Nosecap" (Unclassified), APL/JHU EM-3957, 1965.
5. M. B. Tate, "Spherically Anti-Symmetric Thermal Stresses in a Radome Nosecap" (Unclassified), APL/JHU EM-3964, 1965.
6. M. B. Tate, "Semi-Symmetric Thermal Stresses in a Radome Nosecap" (Unclassified), APL/JHU EM-3966, 1965.
7. M. B. Tate, "Sinusoidal Semi-Symmetric Thermal Stresses in a Radome Nosecap" (Unclassified), APL/JHU EM-3967, 1965.
8. M. B. Tate, "Cosinusoidal Semi-Symmetric Thermal Stresses in a Radome Nosecap" (Unclassified), APL/JHU EM-3968, 1965.
9. M. B. Tate, "Generalized Radially Symmetric Thermal Stresses in a Radome Nosecap" (Unclassified), APL/JHU EM-3969, 1965.

RESEARCH AND EXPLORATORY DEVELOPMENT III/8b
Airframe Structures - Hypersonic Flight A33BBE
Support: RMGA (BuWeps)
J. F. George
April - June 1965

STRUCTURAL DEFORMATION BEHAVIOR AT HIGH TEMPERATURES

Peformance requirements of hypersonic missiles impose severe environments on the airframe structure, while at the same time they require high structural efficiency to minimize weight. Under these conditions, it is necessary to consider structural behavior in a more complete manner than is often done. The current studies are aimed at a better understanding of the transient deformation that takes place under rapidly varying stress and temperature conditions and the effect these transients have on the load-carrying capability of the structure.

SUMMARY

Over fifty specimens of the titanium alloy Ti-13V-11Cr-3Al have been tested to study high-temperature structural behavior. Thermal expansion characteristics, instantaneous stress-strain relationships, and time-dependent deformation behavior (creep) were measured for temperatures up to 2500°F. Additional tests measured specimen deformation under conditions of varying stress and temperature.

The results of the four thermal expansion tests are shown in Fig. 1. The average value for the coefficient of expansion is 7.5 x 10^{-6} in/in/°F. This is approximately one third higher than other published information (Ref. 1). The possible reasons for this difference are being checked.

Results of a typical set of creep tests are shown in Fig. 2. Similar sets of creep tests were run for temperatures between 500° and 2500°F. For the very short times used in these tests it is possible to express the creep rate as a function of temperature, stress, and accumulated creep strain.

Figure 3 shows the conditions of varying temperature and stress that were used to study transient deformation. The results of 12 tests are shown in Fig. 4, where the total measured deformation is made up of elastic, plastic, time-dependent, and thermal strain. The material characteristics of thermal expansion, stress-strain relations, and creep behavior are being used to correlate predicted and measured deformation. Thus far the results of these studies show that the actual strain lags behind predicted values during periods of changing temperature and stress. This behavior could be important in determining maximum values of stress in airframe structures.

FUTURE PLANS

Analysis of the transient conditions will continue in order to verify differences in the

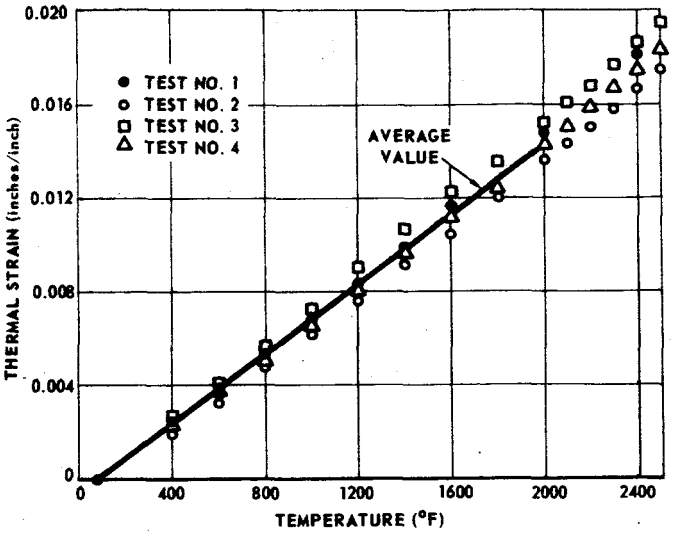

Fig. 1 Thermal Expansion Tests for Titanium Alloy - Ti-13V-11Cr-3Al. (76522)

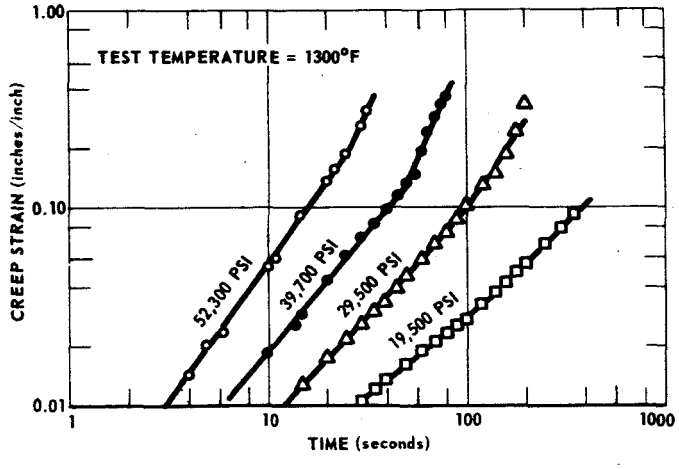

Fig. 2 Typical Creep Test Results for Titanium Alloy - Ti-13V-11Cr-3Al. (76523)

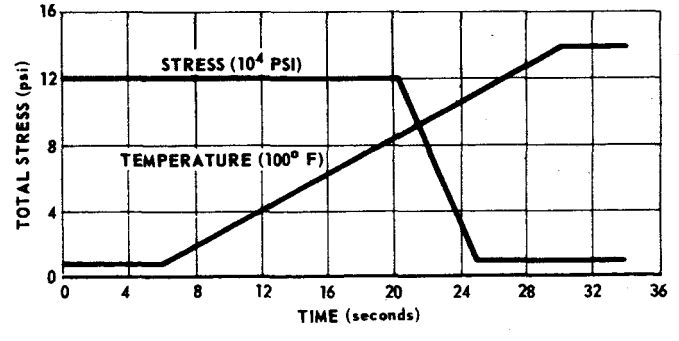

Fig. 3 Temperature and Stress Histories for Transient Deformation Tests. (76524)

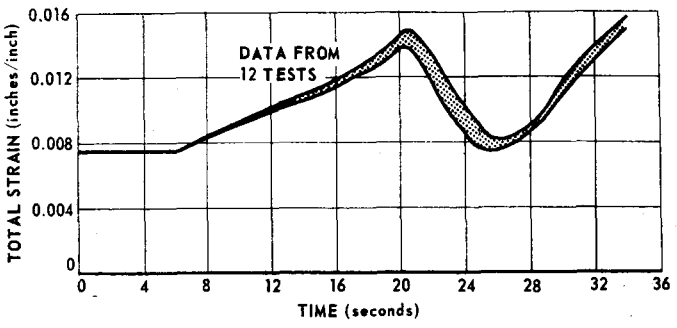

Fig. 4 Total Measured Strain Resulting from Variable Stress and Temperature Tests. (76525)

predicted and actual materials behavior. Documentation of these results will include examples of the effect of these differences on thermal stress in typical airframe structures and will make recommendations as to the type of materials testing required to perform complete structural analysis.

BACKGROUND

The high-performance missiles of the next generation will require more efficient structural systems. In addition, internal and external profiles will be extremely critical with respect to change in shape. It will be necessary, therefore, to conduct a more complete structural analysis of the missile airframe and to consider many more modes of behavior in order to design a vehicle to meet these requirements. Such analysis requires complete information on the behavior of the structural materials to be used and a mathematical theory that is compatible with this behavior.

There is now a wealth of experimental data on the mechanical properties of common engineering materials, and many solutions exist for the stress analysis of complex structures. Difficulties exist, however, in the actual solution of practical problems, for most of the data and analysis techniques are geared toward solution of elastic, linear, and equilibrium problems. The problems associated with the high-performance vehicles encompass inelastic behavior, nonlinear load and material characteristics, transient environmental conditions, and time-dependent material properties.

Since even the simplified approaches to the solution of these problems for complex structures are quite time consuming, it is important that the limitations on the accuracy of such solutions be understood and, in fact, the method of analysis must be tailored to yield acceptable results for the particular problem. In order to do this, knowledge must exist, at least in a general way, of the behavior of structures and materials under conditions similar to the actual problem. This is true even if an exact mathematical solution is not available to use these data. The current studies are designed to yield information on the general behavior of structures subjected to rapidly varying states of stress and temperature.

PROGRESS DURING QUARTER

All data for the current studies were obtained during a materials test program at the Pomona Division of General Dynamics the previous year. These raw data have been reduced, digitalized, and punched on IBM data cards. This facilitates automatic plotting of creep data and enables the computer to assemble data from different tests and to develop and plot isochronous stress-strain curves. Creep strain histories have been plotted for 22 tests, ranging from 1000° to 2500°F, and isochronous stress-strain curves have been prepared for five temperatures in this range. Plots of $\log_{10}$ (creep strain) versus $\log_{10}$ (time) have been prepared for 1000°, 1300°, 1700°, and 2100°F (see Fig. 2).

Using strain data recorded during the initial loading period of the creep tests, the instantaneous stress-strain characteristics of the material have been determined from room temperature to 2500°F. These characteristics are used in predicting the elastic response of the material to stress and temperature changes. The coefficient of thermal expansion has been determined for use up to 2000°F.

The data from 12 tests of varying temperature and stress levels have been plotted, and the common portions of the plots have been correlated to yield a comparative range of experimental results (see Fig. 4). Numerical analyses are being made in an attempt to generate the observed values of deformation by applying the known stress and temperature histories to the measured material characteristics of thermal expansion, stress-strain relations, and creep strain behavior.

DISCUSSION

At the present time, there is a question as to why the thermal expansion test data do not agree with previously published data for this alloy (Ref. 1). The source of these data is being checked to see if there are any significant differences in the alloy used or in the test procedures. The data recorded during the initial heat-up for the creep tests are consistent with the data taken for the thermal expansion coefficient measurement.

The creep test data shown in Fig. 2 are readily usable in predicting creep strain rates for material stressed at a temperature of 1300°F. Similar tests were run at temperatures of 500°, 1000°, 2100°, and 2500°F. Though some sets of these data are not as uniform in pattern as the 1300°F set, it has been possible to smooth the data by cross-plotting on an isochronous stress-strain diagram. Thus, for known values of stress and temperature, the creep strain rate can be estimated based on the amount of accumulated plastic strain.

In using the previously developed data to generate total strain histories for variable stress and temperature tests, it may be seen that all of the deformation processes do not go on simultaneously. That is, there are lags in certain phases of the deformation while the material goes through "incubation" periods (Ref. 2). These lags have the effect of changing the maximum values of the total strain and changing the total strain rate. Future plans are to study the effect of these changes on the load carrying capability of the structure.

REFERENCES

1. R. A. Wood and H. R. Ogden, "The All-Beta Titanium Alloy (Ti-13V-11Cr-3Al)" (Unclassified), Defense Metals Information Center, Battelle Memorial Institute DMIC Report No. 110, April 1959.
2. R. P. Carreker, J. G. Leschen, and J. D. Lubahn, "Transient Plastic Deformation" (Unclassified), Trans. AIMME, Vol. 180, 1949, pp. 139-146.

RESEARCH AND EXPLORATORY DEVELOPMENT 111/9
Aeroelastic Research and Development A33BBE
Support: RMGA (BuWeps)
J. T. Stadter
April - June 1965

VIBRATION STUDIES

In guided missile development, it is important to know the frequencies of free vibration of elastic structures and structural elements with good precision. For a missile as a whole, the frequencies and mode shapes in bending and torsion have a strong influence on control system performance. Those of other structural components such as wings, fins, and panels are crucial for aeroelastic (flutter) behavior in flight.

The free vibration of only the most elementary structural elements can be analyzed "exactly," and approximation methods must be used to estimate the vibration characteristics of all others. The object of these vibration studies is to develop suitable approximation techniques and to apply them to problems of elastic structural vibration.

The most useful approximation methods are those which give upper and lower bounds to the true (but unknown) frequencies. With such bounds, it is possible to state, for example, that the lowest frequency of a structure is 18.7 ± 0.1 cps; and with the use of approximate mode shapes generated in the approximating procedures, it is also possible to give similar estimates for the accuracy of the calculated mode shapes themselves.

For upper bounds to frequencies the most effective procedure is the well-known Rayleigh-Ritz technique. For lower bounds, the problem is much more difficult. However, recently, Bazley and Fox have developed a family of methods which have a wide range of applicability in vibration problems of structural mechanics. The vibration studies are concentrated on the further development of these techniques and their exploitation in structural vibration problems.

SUMMARY AND CONCLUSIONS

In the period covered, the bounding procedures have been applied to a variety of problems. Among these is an ordinary differential eigenvalue problem used by Collatz (Ref. 1), Weinstein (Ref. 2), and Fichera as a test problem for the effectiveness of lower bound calculation techniques. These results, given in Tables I and II, demonstrate how effectively the method of truncation (Ref. 3) can be employed in problems of this type. The program DETMT has been used to verify the calculations for bounds to frequencies of vibration of free rectangular plates, and the report describing these results has been prepared. The calculation of bounds for frequencies of beams on partial elastic foundations has been continued with excellent results, and a calculation program (Ref. 4) to implement a method given in Ref. 5 has been written and tested.

FUTURE PLANS

The digital computation programs continue to be used to estimate the frequencies of elastically clamped beams and shafts. From this basis, the investigation will be extended to include elastically clamped plates.

Theoretical studies will continue with the aim of developing and extending procedures for estimating eigenvalues (frequencies), eigenfunctions (mode shapes), and related quantities for problems in structural vibration.

A newly developed method for improving rigorous estimates for eigenvalues of continuous elastic systems will be applied to a variety of problems. Preliminary calculations indicate that this method should prove quite effective.

The approximation procedures will be applied to plates of skew and other planforms and to beams and shafts with attached masses.

BACKGROUND

The frequencies of free vibration of elastic structures are obtained as the eigenvalues of the differential system describing the structure. In many cases this eigenvalue problem cannot be solved exactly, and approximation procedures must be used to estimate the eigenvalues. The Rayleigh-Ritz method yields estimates which are upper bounds to the eigenvalues. In order to know the error in any approximation, it is necessary to have both lower and upper bounds. Techniques developed by Bazley and Fox provide a means for obtaining lower bounds to eigenvalues.

In applying these lower bound techniques, one obtains a base problem, which can be resolved exactly and which has eigenvalues below those of the given problem. From the base problem, one constructs a series of intermediate problems in such a way that each intermediate problem can be solved exactly and has eigenvalues which are larger than the eigenvalues of the base problem but smaller than those of the given problem. The eigenvalues of the intermediate problems are the desired lower bounds. These are obtained as the roots of

Table I
Bounds to Eigenvalues of the Differential Equation:
$-u'' - \lambda(1 + a \sin x)\, u = 0, \quad u(0) = u(\pi) = 0$
Even Symmetry Class, $u(\frac{\pi}{2} + x) = u(\frac{\pi}{2} - x)$; $a = 1.00$

	Intermediate Lower Bounds Intermediate Order 15 Truncation Order 25	Rayleigh-Ritz Upper Bounds Order 15
1	0.54031_9	0.54031_9
2	5.4486_4	5.4486_4
3	15.312_6	15.312_6
4	30.115_0	30.115_0
5	49.853_3	49.853_3
6	74.526_8	74.526_8
7	104.13_5	104.13_5
8	138.67_9	138.67_9
9	178.15_7	178.15_7
10	222.57_0	222.57_1

finite matrices, usually on a digital computer. The lower bounds can be improved (i.e., made larger) by calculating with a matrix of larger size.

Once sufficiently good upper and lower bounds to eigenvalues have been found, it is then possible to use this in other methods, e.g., Ref. 6, to obtain even better bounds.

DISCUSSION

An ordinary differential eigenvalue problem which is frequently used as a test problem for the effectiveness of lower bound procedures is given by

$$- u''(x) - \lambda(1 + a \sin x)\, u(x) = 0, \quad 0 < x < \pi$$

$$u(0) = u(\pi) = 0 ,$$

where prime denotes differentiation with respect to x, λ denotes the eigenvalues, and a is a nonnegative parameter. The even and odd symmetry classes have been considered separately. Solutions which are in the even symmetry class satisfy

$$u(\tfrac{1}{2}\pi - x) = u(\tfrac{1}{2}\pi + x) ,$$

and solutions in the odd symmetry class satisfy

$$u(\tfrac{1}{2}\pi - x) = - u(\tfrac{1}{2}\pi + x) .$$

The base problem used in the lower bound procedure is

$$- u''(x) - \lambda u(x) = 0 , \quad 0 < x < \pi$$

$$u(0) = u(\pi) = 0$$

with the additional condition

$$u(\tfrac{1}{2}\pi - x) = u(\tfrac{1}{2}\pi + x)$$

for the even symmetry class, and

$$u(\tfrac{1}{2}\pi - x) = - u(\tfrac{1}{2}\pi + x)$$

for the odd symmetry class. The eigenvalues and normalized eigenfunctions of the base problem are given by

$$\lambda_i^o = (2i - 1)^2 \quad \text{and}$$

$$u_i^o = \sqrt{\frac{2}{\pi}} \sin (2i - 1)x$$

for the even symmetry class, and

$$\lambda_i^o = (2i)^2 \quad \text{and}$$

$$u_i^o = \sqrt{\frac{2}{\pi}} \sin 2ix$$

for the odd symmetry class.

This base problem was used in applying the method of truncation (Ref. 3) to give the lower bounds which are listed in Tables I and II. After the formulas for the necessary matrices had been derived, they were programmed for the computer and used in conjunction with the program DETMT to solve the matrix problem and thus yield the lower bounds.

The upper bounds were obtained using the Rayleigh-Ritz procedure. In this procedure, it is necessary to perform a matrix diagonalization. The digital computer was used for this operation. The matrix which had to be diagonalized is denoted by (R), and the formula for the element in the ith row and the jth column is

$$(R)_{ij} = K_i^2\, \delta_{ij} + \frac{8a}{\pi} \frac{1}{[1-(K_i-K_j)^2][(K_i+K_j)^2-1]} ,$$

where δ_{ij} is Kronecker's delta,

a is the parameter from the original problem,

K_i = 2i-1 for the even symmetry class,

and K_i = 2i for the odd symmetry class.

Table I gives bounds for the first ten eigenvalues corresponding to eigenfunctions in the even symmetry class, and Table II gives bounds for the first ten eigenvalues corresponding to eigenfunctions in the odd symmetry class for the parameter value a = 1. The lower bounds were obtained from a 15th order intermediate problem using a 25th order truncation. The upper bounds were obtained from a 15th order Rayleigh-Ritz procedure. In these tables, the numbers have been rounded to six figures and the last figure is depressed to indicate the rounding.

REFERENCES

1. L. Collatz, Eigenwertprobleme und ihre Numerische Behandlung, Chelsea Publishing Co., 1948, p. 187.
2. A. Weinstein, "On the Sturm-Liouville Theory and the Eigenvalues of Intermediate Problems, Numerische Mathematik, Vol. 5, 1963, pp. 238-245.
3. N. W. Bazley and D. W. Fox, "Truncations in the Method of Intermediate Problems for Lower Bounds to Eigenvalues," J. Research Nat. Bur. Standards, Vol. 65B, 1961. Also APL/JHU TG-609, pp. 24-33.
4. N. Rubinstein, A Digital Procedure for Use of the Method of Extensions and Restrictions of Quadratic Forms, APL/JHU TG-706, 1965.
5. N. W. Bazley and D. W. Fox, Methods for Lower Bounds to Frequencies of Continuous Elastic Systems, APL/JHU TG-609, 1964, pp. 34-41.
6. N. W. Bazley and D. W. Fox, "Improvement of Bounds to Eigenvalues of Operators of the Form T*T, J. Research Nat. Bur. Standards, Vol. 68B, 1964.

Table II

Bounds to Eigenvalues of the Differential Equation:

$- u'' - \lambda(1 + a \sin x)\, u = 0, \quad u(0) = u(\pi) = 0$

Odd Symmetry Class, $u(\frac{\pi}{2} + x) = - u(\frac{\pi}{2} - x)$; a = 1.00

	Intermediate Lower Bounds Intermediate Order 15 Truncation Order 25	Rayleigh-Ritz Upper Bounds Order 15
1	2.3717_9	2.3717_9
2	9.7629_7	9.7629_7
3	22.096_7	22.096_7
4	39.367_2	39.367_2
5	61.573_1	61.573_1
6	88.714_1	88.714_2
7	120.79_0	120.79_0
8	157.80_1	157.80_1
9	199.74_7	199.74_7
10	246.62_7	246.62_8

RESEARCH AND EXPLORATORY DEVELOPMENT 111/10
Thermal Studies A33BBE
Support: RMGA (BuWeps)
L. B. Weckesser
April - June 1965

EVALUATION OF A METHOD OF COMPUTING CONVECTIVE HEAT TRANSFER

On many occasions, convective heat transfer approximations are made using a temperature difference method. Use of this method at high temperatures has been found to result in significant errors. Thus, an estimation of the magnitude of this error to be expected at various temperatures is desirable.

SUMMARY

A comparison has been made between the results found using a temperature difference method for computing convective heat transfer on a flat plate and the results found using the familiar and reliable enthalpy difference method. In making this comparison, equations used in the two methods were combined. Upon combining the equations, it was found that the ratio of convective heat transfer as found by the two methods was equal to a ratio of specific heats, i.e.,

$$\frac{q_T}{q_i} = \frac{c_p^*}{Z} .$$

The definitions of the symbols are presented in the nomenclature which follows. When $Z = c_p^*$, the heat transfer computed by the two methods is equal. A comparison of c_p^* and Z at different temperature levels will indicate the variations to be expected between the two methods of computing heat transfer.

Taking the temperature difference $(T_r - T_w)$ as a parameter, values of Z may be determined for different mean temperatures. Considering all temperature-to-enthalpy conversions for 1 atmosphere of pressure, the values of Z and c_p were determined and are presented in Fig. 1. Since the ratio of c_p to Z indicates the heat transfer variation between the two methods, this ratio was determined and is plotted in Fig. 2. The data of Fig. 2 indicate that for a mean temperature of 4000°R, the variation in heat transfer results may exceed 30 percent for large differences between T_r and T_w. Surprisingly, this is not true for a mean temperature of 5000°R. Also, in the lower mean temperature range (below 3000°R) the two methods appear to agree within 5 percent for all values of $(T_r - T_w)$ considered.

BACKGROUND

Much work has been performed to demonstrate the accuracy of the reference enthalpy method using an enthalpy difference to compute convective heat transfer. However, the writer is not aware of any work that presents a comparison of results obtained using this method to those using a temperature difference method. Even

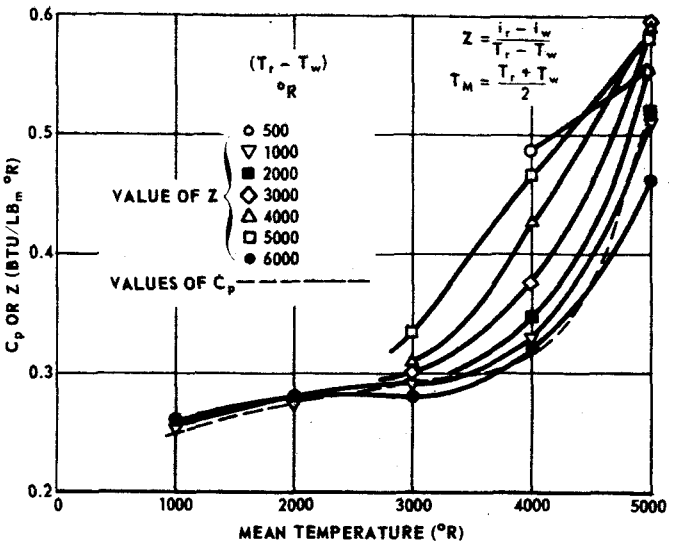

Fig. 1 c_p and Z versus Mean Temperature (T_m). (76520)

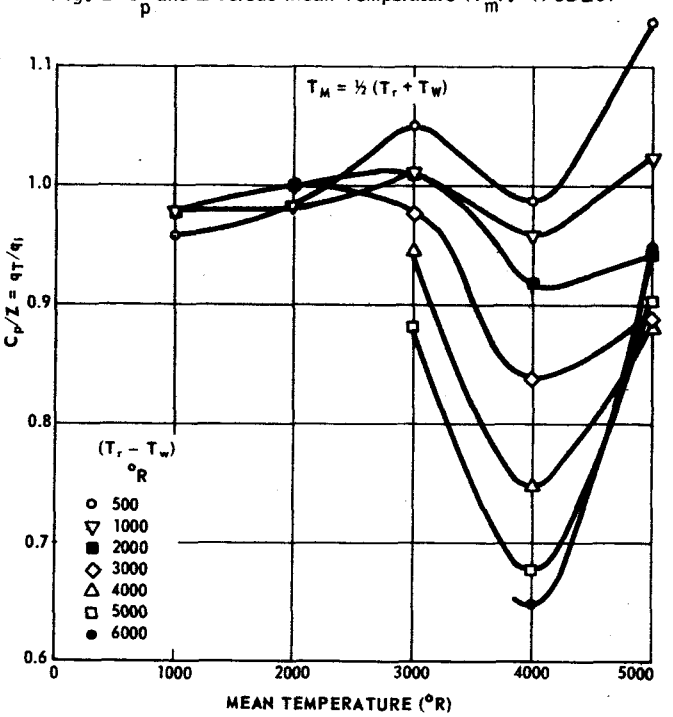

Fig. 2 Ratio of Heat Transfer Based on Temperature to Heat Transfer Based on Enthalpy versus Mean Temperature (T_m). (76521)

though it is somewhat academic to make this comparison, in some cases temperature differences are used to make approximations of the convective heating and an estimate of the error involved in such approximations would be valuable. Therefore, an attempt was made to compare the results obtained by the two methods.

DISCUSSION

The study presented below was performed using flat-plate laminar boundary layer equations since they are the most familiar and easiest with which to work. A similar procedure could be used to define errors associated with the turbulent boundary layer equations. The two methods of computing the convective heat transfer are presented, followed by a combination of equations from the two methods to arrive at one expression for comparing results.

Temperature Difference Method--The temperature difference method of computing convective

heat transfer to a surface is based on the equation:

$$q_T = h_T (T_r - T_w) . \quad (1)$$

In this equation, the recovery temperature, T_r, is determined from a recovery enthalpy, and the local static pressure using the data of Hansen (Ref. 1). The recovery enthalpy is computed from the equation:

$$i_r = i_1 + r \frac{V_1^2}{2gJ} , \quad (2)$$

where r, the recovery factor, is determined from

$$r = \sqrt{Pr^*} .$$

The convective heat transfer coefficient, h_T, of Eq. (1) is computed from the expression:

$$h_T = 0.332 (Re^*)^{0.5} (Pr^*)^{0.333} \frac{k^*}{x} , \quad (3)$$

which is for laminar flow over a flat plate and is derived in Ref. 2. Here the values followed by the superscript * are evaluated at a reference temperature which is determined from a reference enthalpy defined as:

$$i^* = 0.5\, i_w + 0.28\, i_1 + 0.22\, i_r . \quad (4)$$

Using the values described above, the convective heat transfer can be computed by Eq. (1).

Enthalpy Difference Method--The enthalpy difference method of computing convective heat transfer may be described in a similar manner. It is based on the equation:

$$q_i = h_i (i_r - i_w) . \quad (5)$$

The recovery enthalpy is found using Eq. (2) and the recovery factor is again computed by

$$r = \sqrt{Pr^*} .$$

The convective heat transfer coefficient is computed by:

$$h_i = 0.332 (Re^*)^{0.5} (Pr^*)^{0.333} \frac{k^*}{xc_p^*} \quad (6)$$

which is also for laminar flow over a flat plate and is derived in Ref. 2. Again the starred values are evaluated at a reference temperature which is based on the reference enthalpy defined by Eq. (4). With the above method the convective heat transfer can be computed using Eq. (5).

Combination of Methods--The variations between results obtained from the above described methods can best be studied by first combining Eqs. (3) and (6):

$$\frac{h_T}{h_i} = c_p^* . \quad (7)$$

Define Z as:

$$Z = \frac{i_r - i_w}{T_r - T_w} \quad (8)$$

which has the appearance of a constant specific heat. Next, Eqs. (1) and (5) can be combined to give

$$\frac{q_T}{q_i} = \frac{h_T}{h_i} \frac{(T_r - T_w)}{(i_r - i_w)} . \quad (9)$$

Substituting Eqs. (7) and (8) in (9) results in

$$\frac{q_T}{q_i} = \frac{c_p^*}{Z} . \quad (10)$$

Equation (10) shows that when $Z = c_p^*$ the heat transfer computed by the two methods is equal. Therefore, a comparison of c_p^* and Z at different temperature levels will indicate the variations to be expected between q_T and q_i.

A problem arises in attempting to compare Z and c_p^* in that there is no common temperature upon which these values depend. The factor c_p^* is obtained from the reference temperature determined from the reference enthalpy of Eq. (4). The factor Z, on the other hand, is dependent on only i_r and i_w since $T_r = f(i_r)$ and $T_w = f(i_w)$. Therefore, a comparison between c_p^* and Z can only be made if some restriction is placed on T_1 or i_1. If the assumption is made that the local temperature T_1 equals the recovery temperature T_r, (which is approximately true in stagnation regions) then under like pressure conditions $i_1 = i_r$ and

$$i^* = 0.5\, i_w + 0.5\, i_r$$

or

$$i^* = i_m \text{ and } T^* = T_m .$$

Now, taking $(T_r - T_w)$ as a parameter, values of Z can be determined for different values of T_m. Considering all temperature to enthalpy conversions for one atmosphere of pressure, the values of Z and c_p were determined and are presented in Fig. 1. Since the ratio of c_p to Z indicates the heat transfer variation between the two methods, this ratio was determined and is plotted in Fig. 2. The very large differences at 4000°R may possibly be explained by the large change which occurs in c_p above this temperature (see dashed curve in Fig. 1); however, no explanation is available for the results found for 5000°R.

Nomenclature

- c_p Specific heat of air (Btu/lb_m°R)
- g Acceleration due to gravity (32.2 ft/sec^2) (lb_m/lb_f)
- h Convective heat transfer coefficient (Btu/ft^2sec°R)
- i Enthalpy (Btu/lb_m)
- i_m Mean enthalpy = $\frac{i_r + i_w}{2}$ (Btu/lb_m)
- J Joule's constant (778 ft lb_f/Btu)
- k Thermal conductivity (Btu/ft sec°R)
- q Convective heat transfer (Btu/ft^2sec)
- r Recovery factor
- T Temperature (°R)
- T_m Mean temperature = $\frac{T_r + T_w}{2}$ (°R)
- V Velocity (ft/sec)
- x Reference length (feet)
- Re Reynolds number = $\frac{\rho V x}{\mu}$
- Pr Prandtl number = $\frac{\mu c_p}{k}$
- Z $\frac{i_r - i_w}{T_r - T_w}$.

Subscripts

- T Values used in the temperature difference method
- i Values used in the enthalpy difference method
- r Recovery
- w Wall condition
- 1 Local condition
- * Reference condition.

REFERENCES

1. C. F. Hansen, Approximations for the Thermodynamic and Transport Properties of High Temperature Air, NASA-TR-R-50, 1959.
2. L. B. Weckesser, "Evaluation of a Temperature Difference Method of Computing Convective Heat Transfer," APL/JHU EM-3965, 14 May 1965.

RESEARCH AND EXPLORATORY DEVELOPMENT I II/IIa
Radome Structures A33GBBE
Support: RMGA (BuWeps)
R. P. Suess
April - June 1965

LIMITATIONS OF RADOME MATERIALS

Although considerable data are available on radome materials, any many radomes have been constructed, the overall environmental limitations of various radome materials are at the present time unknown. In the context of ever-increasing speed, and thus increasingly severe environments, the problem assumes added importance. A systematic study to establish the limits of existing radome materials will thus be a valuable contribution.

SUMMARY

A study to define the environmental limitations of the three basic radome materials, Pyroceram 9606, fused silica, and alumina for four bands (S, C, X, and K) has been continued and considerably advanced over the past several months. Work during this period has encompassed two areas:

1. Maximum temperature studies defining surface melting conditions
2. Velocity limit studies for determining the maximum velocity history permissible if the maximum allowable thermal stress is not to be exceeded.

A number of maximum temperature studies have been completed, and the necessary data have been obtained to generate a series of graphs which define the velocity and time-to-surface-melting for all materials, thicknesses, and launch angles considered in this study. These graphs (of which Fig. 1 is an example) were generated considering straight-line trajectories employing linear velocity-time histories.

A computer program, capable of computing the velocity history which must not be exceeded if thermal stress failures are to be avoided, has been developed and has been "proven in" by several check runs. The program has been used to generate the data shown in Fig. 2. The dashed curves in this figure represent data computed by the new program. The solid line has been superimposed to represent the velocity limit beyond which thermal stress failures will occur.

A considerable effort has been expended in defining the electrical limitations of the radome materials. This work has resulted in establishment of a criterion for the limit evaluations and the establishment of rapid calculation methods. Utilizing the data from the maximum temperature studies described above, work is now beginning on generating actual electrical limitation results.

FUTURE PLANS

In the immediate future the radome limitations work will entail examining the velocity-time plots for surface melting (see Fig. 1) for their validity as limits when other than straight line velocity-time histories are considered. Other velocity-time histories, such as those defined by a high acceleration boost and moderate acceleration sustain system will be considered. In addition, a large number of velocity limit graphs indicating thermal stress limits (Fig. 2) will be generated for defining the maximum velocity which can be flown before a thermal stress failure will result. A large number will be necessary since each material, thickness, and launch angle must be considered separately. Work will also continue on defining the electrical limitations.

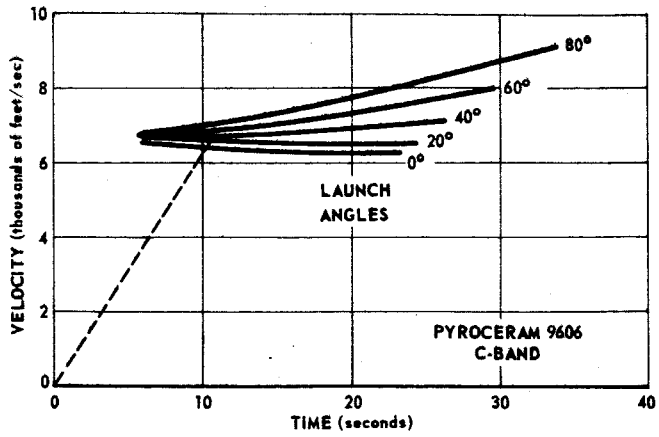

Fig. 1 Time-to-Surface-Melting - Von Karman Radome. (76518)

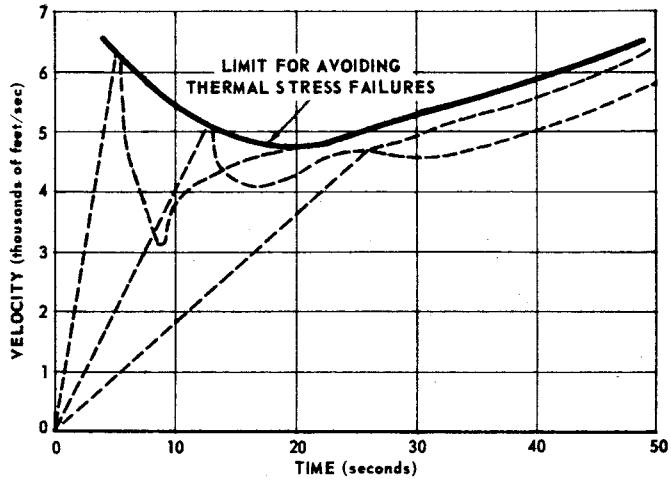

Fig. 2 Velocity Limit of Pyroceram 9606, C-Band, 20° Launch Angle. (76519)

BACKGROUND

A need was recognized by the Bureau of Naval Weapons, RMGA, for definition of the environmental limits of the three basic radome materials in use today: alumina, fused silica, and Pyroceram 9606. Thus, an effort was funded to define these environmental limitations. Prior to the work described in this re-

port, effort has been expended in the following areas:

1. Determination of the effect of boundary layer transition on thermal stress.
2. Determination of the difference between the results of one-dimensional and two-dimensional studies.
3. Definition of the properties of the three radome materials as a function of temperature up to the softening or melting point (see Ref. 1).

The results of these items have been reported in previous progress reports.

DISCUSSION

The maximum temperature studies defining the surface melting conditions were performed utilizing the calculation techniques described in Refs. 2 and 3. These references describe a computer program which will simultaneously analyze the temperatures and thermal stresses in radomes. The value of a series of graphs such as shown in Fig. 1 is that the time-to-surface-melting can be predicted for any of the three materials, any of the four bands, any feasible acceleration, and any launch angle desired. Each of the graphs is based upon straight-line (linear altitude-versus-range history) trajectories.

As an example of the use of the graphs, consider Fig. 1. Suppose it is desired to determine the time-to-surface-melting for a Von Karman Pyroceram 9606 C-band radome flown on a straight-line trajectory having a 20° launch angle and a linear velocity history as indicated by the dashed line in Fig. 1. The time-to-surface-melting is easily read from the graph to be 10.6 seconds. The velocity at initial surface melting is 6600 fps. It is expected that this series of graphs will be extremely useful since a large amount of data can be presented in only 12 graphs; one for each of the three materials and its four bands.

The results shown in Fig. 2 were generated by the velocity-limit computer program which computes the thermal stresses resulting from an initial velocity history and upon reaching a pre-defined allowable stress automatically converts to defining velocities as a function of time that will maintain the thermal stress at the maximum allowable level. The dashed curves in Fig. 2 represent actual output from this program. The solid line superimposed on the upper limits of the dashed curves represents the maximum velocity which must not be exceeded if a thermal stress failure in the radome is to be avoided. This plot can be used by first matching material, band, and the launch angle of interest with the proper plot. One then plots the particular velocity-time history on the graph. If the particular velocity-time history of interest does not exceed the solid curve, no thermal stress failure will result.

A significant effort has been spent on the electrical aspects of the radome limitations work. To date this effort has been devoted to determining the criteria by which the limits will be defined and developing rapid computational techniques for generating actual results.

REFERENCES

1. D. L. Coble and L. B. Weckesser, "Electrical, Mechanical, and Thermal Properties of Alumina, Fused Silica, and Pyroceram 9606" (Unclassified), APL/JHU EM-3926, 24 November 1964.
2. D. W. Fox, H. Shaw, Jr., and J. Jellinek, "Numerical Approximations in Heat Transfer Problems and Usage of IBM 7090 Computer for Solutions" (Unclassified), APL/JHU CF-2954, 17 May 1962.
3. R. P. Suess, Additions and Improvements to the APL IBM 7094 Heat Transfer Computer Program (Unclassified), APL/JHU TG-602, September 1964.

RESEARCH AND EXPLORATORY DEVELOPMENT I II/IIb
Radome Structures A33BBE
Support: RMGA (BuWeps)
R. M. Rivello
April - June 1965

RADOME STRESSES

The aerodynamic heating associated with high-speed flight induces large thermal stresses in the structures of interceptor missiles. Conditions are particularly critical in the radome of these vehicles, where heat-transfer rates are high and the ceramic materials used behave in a brittle manner. As a result, it is necessary to develop analytical methods which accurately predict the radome thermal stresses.

SUMMARY

Techniques for computing the thermal stresses in laminated radomes similar to that shown in Fig. 1 have been investigated. The methods studied are based upon shell theory, thick-walled cylinders combined with membrane theory, and concentric thick-walled cylinder theory. The latter was concluded to be the most appropriate and is being programmed for machine computation. Laminated radome configurations that have been studied to date indicate that the critical stresses occur in the axial direction when the ratio of the radius to thickness is small.

FUTURE PLANS

Tests will be made on laminated cylinders and cones using quartz lamps as a heat source to substantiate the theoretical results. As soon as the method is programmed and checked out, it will be used in studies to determine the optimum configurations for laminated radomes. It will also be used to determine the importance of the temperature dependence of the modulus of elasticity in homogeneous radomes with thermal gradients.

BACKGROUND

The work reported is part of a larger program to develop hypersonic structures and establish the limitations of radome materials. Slip cast laminated radomes are currently being developed by several companies. The greater electrical bandwidth and lower cost advantage which these radomes have in comparison to solid configurations have been discussed in Ref. 1. It has been necessary to develop analytical methods for predicting the thermal stresses in these laminated designs to establish their limitations and determine their structural merit relative to homogeneous solid wall construction.

DISCUSSION

The greatest thermal stresses in ogival radomes appear to occur in the region where the aerodynamic flow undergoes a transition from laminar to turbulent conditions (Ref. 2). The ratio of the radius to the wall thickness at this point is usually so small that significant errors result if thin-shell theory is used to predict the stresses. The theory of elasticity solution for thermal stresses in a thick-walled cylinder (Ref. 3) has been found to be in acceptable agreement with limited test results on aerodynamically heated radomes (Ref. 4). It would be expected that the critical stresses in laminated radomes would also occur in the transition region and that they could be predicted by a modification of the thick-walled solution.

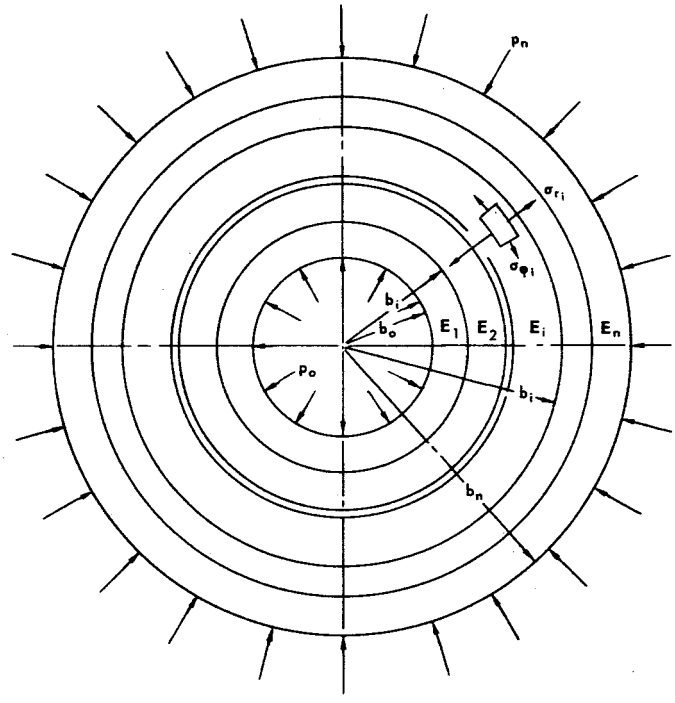

BOUNDARY CONDITIONS: $\sigma_{r_1}(b_o) = -p_o$, $\sigma_{r_n}(b_n) = -p_n$
$\sigma_{r_i}(b_i) = \sigma_{r_{i+1}}(b_i)$, $i = 1, 2, \ldots, n$
$u_i(b_i) = u_{i+1}(b_i)$, $i = 1, 2, \ldots, n$

Fig. 1 Geometry of Laminated Cylinder. (76526)

The theoretical methods which are being studied for computing the stresses in laminated cylinders are as follows:

1. Nonhomogeneous thin-shell theory,
2. Thick-walled cylinder core with membrane faces, and
3. Multiple concentric thick-walled cylinders.

The first of these theories is the most simple

and is able to handle the variable elastic modulus of the laminated cylinder. However, it does not give the radial stresses (which may be important in producing delamination) and is very inaccurate for the small ratios of radius to thickness which occur near the nose of an ogive. The theory for the thick-walled cylinder core with membrane faces results in a closed form solution, but the expressions for the stresses are lengthy and time consuming in hand calculation. The results are in reasonably good agreement with the third (and most accurate) method which is not suitable for hand calculations.

The concentric thick-walled cylinder approach has been chosen for use in further radome studies because of its greater accuracy and generality and is currently being programmed for machine computation. It is best explained by referring to Fig. 1. The laminated cylinder is divided into an arbitrary number of concentric cylinders with a constant modulus of elasticity within each region. The stress and deflection equations from Ref. 3 for a thick-walled cylinder are applied to each of the concentric cylinders. These equations contain two constants of integration for each of the concentric cylinders. These are evaluated by equating the radial stresses, σ_r, and the displacements, u, at each of the interfaces between the cylinders. The radial stress is also required to equal the applied pressure at the inner and outer radii of the composite cylinder. The axial stresses are determined by satisfying the requirement that the resultant axial force is zero. The method is general and may be used to analyze thick-walled homogeneous cylinders where there is a significant variation for the temperature-dependent modulus through the wall.

To date, studies of sandwich radomes have indicated that the axial stresses are more critical than those in the circumferential direction. However, it may be possible to minimize these stresses by an optimum choice of the densities and thicknesses of the laminates.

REFERENCES

1. D. L. Loyet and R. Yoshitani, "Ceramic Sandwich Radome Design," Proc. of the OSU-RTD Symposium on Electromagnetic Windows, Vol. III, 2-4 June 1964.
2. L. B. Weckesser and R. P. Suess, "Limitations of Radome Materials," Section III/6 Research and Exploratory Development for the Missile Guidance and Airframe Branch, Bureau of Naval Weapons, Quarterly Report, October-December 1964 (Unclassified), APL/JHU, GQR/64-4.(Section also in RQR/64-4.)
3. S. Timoshenko and J. N. Goodier, Theory of Elasticity, McGraw-Hill Book Co. Inc., New York, 1951.
4. R. P. Suess, "Comparison of Theory and Experiment, Radome Temperatures and Stresses," APL/JHU EM-3884, 1 July 1964.

RESEARCH AND EXPLORATORY DEVELOPMENT 111/12
Research and Development in Masers A34BGH
Support: RMGA-8 (BuWeps)
A. W. Nagy
April - June 1965

MASER RESEARCH PROGRAM

The development of a wide band cavity maser technique would have application in communication systems, radar and radio astronomy, and advanced missile systems where very low noise microwave amplification is desirable for improving system performance. Initial experimental efforts have been made at X-band. A continued objective of the program is the extension of any promising results, especially with the zero-field maser technique, to masers operating with paramagnetic powders in little or no magnetic field and possibly in the higher microwave and millimeter wave ranges. Important applications to missile radiometry would be possible in this part of the spectrum.

SUMMARY AND CONCLUSIONS

The main problem at present is the preparation of a ferric corundum powder with optimum iron concentration having maser properties similar to those of the crushed flame grown boule. Since experimental runs have been temporarily suspended because of a move to newer and larger laboratory quarters, activities in this program have been confined to assessment of a new flux melt process for the preparation of iron doped sapphire single crystals and to the design, construction, and test of a special oven with capabilities to 1700°C. The higher temperature required during the second stage calcining of the ferric aluminum sulphates is expected to give the powder samples the increased density and conductivity characteristic of the flame grown boule.

Construction of a second furnace is under way for use in the flux melt process. With regard to temperature, this process is more involved since it requires the programming of a cooling phase of 1° to 2° per hour from the point of maximum melt, about 1280°C. This run requires eight to ten days. Hopefully, large thin single crystals are possible with a wide range of Fe^{3+} concentration. Breadboard circuitry to accomplish this cooling program is being assembled and checked.

Machine calculations on the IBM 7094 of the helix parameters have been almost completed. The practical design of a traveling wave helix structure is now under way.

FUTURE PLANS

Completion of the furnace with capability to 1700°C will permit resumption of the iron sapphire powder dopings via the sulphates and examination of a similar process using equivalent nitrate salts. Completion of the second furnace for the flux melt process together with the hardware for the temperature regulation and cooling program should be accomplished during the coming quarter. It should be noted that the flux melt approach discussed in a previous report is potentially suitable for growing a large variety of doped single crystals and could form the basis for an adjunctive maser materials program essential to the extension of the present maser work into the millimeter wave region. The techniques for growing suitable paramagnetics by this process through an outside commercial source would generally be prohibitively costly.

BACKGROUND AND DISCUSSION

The first phase of the maser program was initiated with the following objectives: (a) optimize the gain-bandwidth product of a reflection cavity ruby maser in single and multiple cavity configurations, and (b) examine the suitability of iron sapphire as a zero field maser material with possible adaptation of the multiple cavity broadband techniques developed in (a). As indicated in previous quarterly reports and the published Refs. 1, 2, and 3, this phase of the maser program has been essentially accomplished. The present phase of the program is concerned mainly with the preparation within APL of a suitable doped Fe^{3+} corundum powder which could be used as a paramagnetic operating either in a cavity or traveling wave maser structure. In the zero field mode a powder paramagnetic would allow novel geometries in slow wave structures and would have some advantages over magnetic field maser operation (Ref. 4). The results of a large number of experimental runs indicate the feasibility of a zero field maser using an iron doped sapphire powder. Thus far the optimum concentration of Fe^{3+} appears to be in the range of 0.01 to 0.025 percent. However, the large amount of pump power required for inversion indicates that the powdered samples are not masering with the characteristics typical of the flame fusion single crystal boule.

REFERENCES

1. A. W. Nagy and G. E. Friedman, "Reflection Cavity Maser with Large Gain Bandwidth," Proc. I.R.E. Vol. 50, December 1962, pp. 2504-2505.
2. G. E. Friedman and A. W. Nagy, "Iron Sapphire Maser with No Magnetic Field," Proc. I.E.E.E. Vol. 51, February 1963, pp. 361-362.
3. A. W. Nagy and G. E. Friedman, "A No-Field Powder Maser," Proc. I.E.E.E. Vol. 51, July 1963, p. 1037.
4. A. W. Nagy and G. E. Friedman, "Zero-Field Maser," APL Technical Digest, July-August 1964, pp. 2-12.

RESEARCH AND EXPLORATORY DEVELOPMENT 111/14
Flame Attenuation Studies A34BGH
Support: RMGA-8 (BuWeps)
R. P. Hockensmith
April - June 1965

FLAME INTERACTION WITH MICROWAVE SIGNALS

The purpose of this program is to develop static test methods that are useful in predicting in-flight solid-rocket-motor flame interaction with microwave signals passing through and around the flame.

SUMMARY AND CONCLUSIONS

Work Area I--There are two areas of work: (a) survey work being done in the field and independent effort towards determining the mechanisms of the flame that alter the propagation of microwave signals in the flame; attenuation, phase, and random variations of attenuation and phase; (b) measuring and analyzing signal change data of selected rocket motors at C- and X-band frequencies, using transportable equipment specially assembled for this mission.

The effects of a rocket exhaust on microwave propagation are not adequately described by simple plasma equations. This is because the plasma structure of the rocket exhaust is complex, turbulent, and not accurately defined. A survey of applicable work in plasma and flame research is presently being conducted. Theoretical and experimental studies at APL are also planned.

Work Area II--Signal level changes at C- and X-band have been measured for a Standard Missile-candidate propellant, designated FDS, using nonfocused microwave antennas located such that propagation through the flame was at angles of 15° and 32° with respect to the missile centerline.

A noise-measurement test was attempted on the same rocket motor. However, acoustical levels at the test area caused the commercial wideband amplifiers to generate noise which exceeded the microwave carrier power level; thus no useful data were obtained. The noise-measuring system was completely redesigned to circumvent the acoustic noise problem.

A sound recording was made for correlation with the noise recording. No correlation was attempted since the noise measurement was unsuccessful.

New equipment has been assembled to measure AM-FM noise that uses a field effect transistor (FET) amplifier ahead of a solid-state amplifier, instead of the tube-model amplifier used on the test described above. This equipment has the capability of measuring FM noise with a 9-cycle deviation at a 1250-cycle rate (49 db) and 100-cycle deviation at a 30 kc rate (55 db). AM noise can be measured to -110 db level below the carrier. It uses solid-state components wherever possible and has other new features to minimize acoustic noise effects.

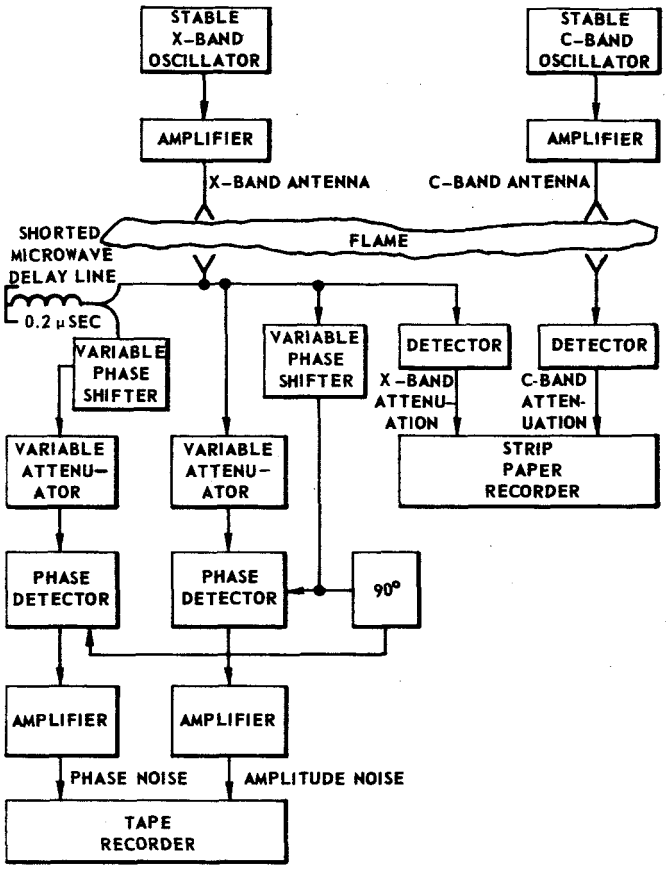

Fig. 1 Existing Noise and Attenuation Measuring Instrumentation. (76660)

A paper was presented at the Interagency Solid Propulsion Meeting in San Francisco on June 10. The paper, entitled, "Effects of Flame Attenuation on Guidance System" was written by B. D. Dobbins and G. T. Munsterman. It was presented by Mr. Dobbins. The purpose of the paper was to familiarize personnel concerned with propellant specifications with basic operation of missile guidance systems, and, more specifically, the effect of flame attenuation, the specification of flame attenuation, and to clarify the meaning of the flame noise specifications.

FUTURE PLANS

Work Area I--Effort toward determining the mechanisms which affect propagation of microwave signals through the solid-rocket motor flame will be continued.

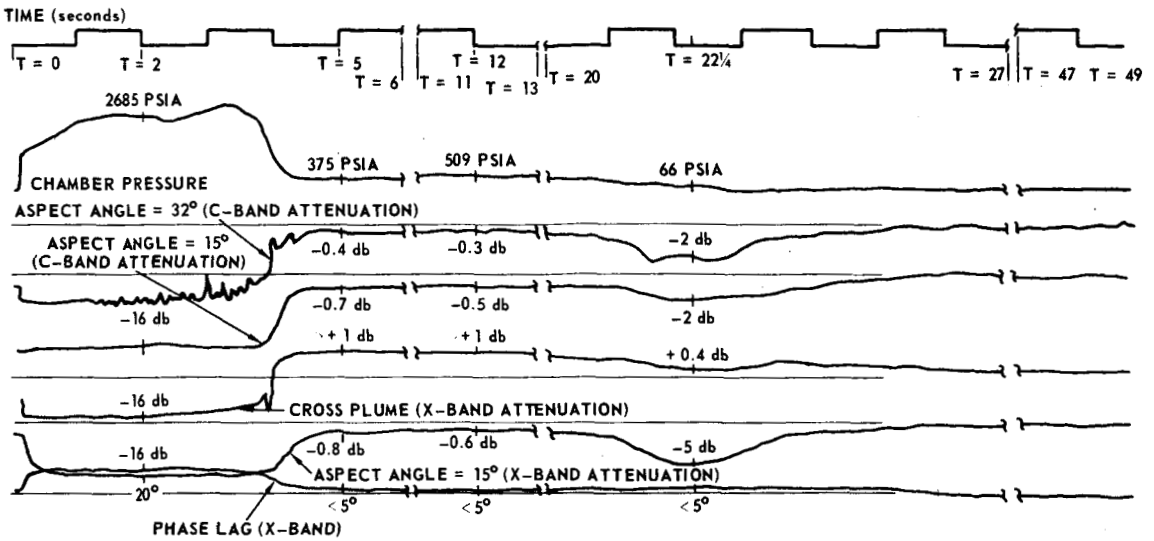

Fig. 2 QA-2 Flame Interference Data. (76681)

Work Area II--Amplitude and phase noise produced by the rocket exhaust of two typical rocket motors flying a ballistic course will be measured in July. The rockets are Standard Missile vehicles specially instrumented for flame attenuation measurements.

Methods of obtaining microwave signal flame interaction data using small seeded alcohol flames will be investigated.

DISCUSSION

Signal level changes of -0.4 db at C-band (32° angle) -0.7 db at C-band, and -0.8 db at X-band (15° angle) were measured on a Standard Missile-candidate sustainer propellant. This propellant was designated as FDS material, motor number QA-2 by Allegany Ballistics Laboratory. The test was conducted at the Allegany Ballistics Laboratory in Cumberland, Maryland.

A dual-band transmitting horn was designed so that the angles through the flame and horn position were common for the two frequencies. A dual-band receiving parabolic reflector antenna was designed to have high gain and reduce the effects of external reflections on the measured data. It is expected that these antennas will be used for any rocket motor tests in which APL can participate in measuring microwave interaction with microwave signals.

New noise measurement equipment has been designed and tested. It is housed in a box measuring approximately 2½ by 3½ by 2½ feet high. Figure 1 is a block diagram of the equipment. It consists of 120 feet of waveguide delay line, three magic tees, two variable attenuators, two phase shifters, two microwave balanced mixers with back diodes, a hybrid coupler, an isolator, and various configurations of transmission line. Following the mixers is a 300-cycle high-pass filter; following the filter, the signal is amplified by a 30-db-gain FET amplifier. The FET amplifier is connected to a 1-mc bandwidth stereo preamplifier having 60-db gain. The output of the stereo is fed into a 300-cycle high-pass filter and dividing network having 0 or -20 db outputs to a tape recorder. Data are tape recorded during rocket-motor firings. The tapes are subsequently analyzed with a laboratory spectrum analyzer to ascertain noise levels. Flame attenuation is also measured and recorded on a visicorder strip recorder.

An example of flame attenuation data for the QA-2 motor is shown in Fig. 2.

REFERENCES

1. R. P. Hockensmith, C. Gambrill, Jr., and H. H. Nall, "Trip Report, Allegany Ballistics Laboratory; Measurements of Microwave Interference Standard Missile-Candidate Propellant FDS, QA-2 Static Firing; April 2, 5, 6, and 7, 1965"(U) (Confidential), APL/JHU BGH-SD/037, 23 April 1965.

RESEARCH AND EXPLORATORY DEVELOPMENT III/15a
Thin Film Microelectronics A35CME
Support: RMGA-8 (BuWeps)
D. Abraham and T. O. Poehler
April - June 1965

THIN-FILM ACTIVE ELEMENTS

The development of a thin-film triode (TFT) for use as an active element in thin-film microelectronic circuitry may provide a degree of reliability in high-radiation intensity backgrounds not yet achieved by other means. It will also eliminate the cumbersome need to attach semiconductor active elements to thin-film passive networks to achieve complete circuits.

SUMMARY AND CONCLUSIONS

Chlorine doping of the cadmium selenide semiconducting film in TFT's has been accomplished in three ways with comparable results. The 40-mil-wide TFT's have had transconductances as high as 20,000 μmhos. CdSe film thickness is monitored during deposition and has been limited to 800Å for most of the last vacuum depositions. Selected devices have been subjected to a continuous operation life testing program which has been underway since February of this year. The DC bias required to maintain an optimum operating condition has drifted slowly upward.

FUTURE PLANS

The life test results mentioned above indicated that a detailed examination of the physical and chemical parameters affecting the semiconductor-dielectric interface must be initiated. It is the surface states at the interface which must be neutralized by the electric field provided by DC bias. As a direct consequence of the observed drift in the required DC bias, it is concluded that stable devices cannot be produced until the interfacial condition is clearly understood and stabilized. Attention must then be focussed on this aspect of the TFT.

DISCUSSION

In addition to the substrate surface doping followed by diffusion, mentioned in the last quarterly report, chlorine doping has been accomplished by the addition of either sodium chloride or ferrous chloride to the CdSe prior to its vacuum evaporation. Table I illustrates the results obtained with the various doping materials. Concentrations by weight of these compounds in CdSe ranging from 1 to 5 parts per thousand have all been used with success. Many other halogen salts would probably be equally suitable. The only limitation which might prove significant is the discrepancy between the vapor pressure of the salt and that of the CdSe in the range of temperatures at which CdSe can be deposited. The situation is not as serious as the above might imply. Should the salt dissociate at low temperature, much of the halogen might react with the CdSe and thus be conserved until the CdSe, in turn, dissociated and evaporated to recombine at the substrate along with the halogen.

Table I

Results of CL Doping Experiments on CdSe TFT's

Specimen	Transconductance (micromhos)	Resistivity (ohm-cm)	Carrier Mobility (cm^2/v-sec)	Doping Method
DU	1000	300	6	$FeCl_3$ surface film (post diffused)
DW	2500	100	3.5	$FeCl_3$ surface film (post diffused)
ED	4000	900	60	$FeCl_2$ coevaporation
EE	1000	30	3	$FeCl_2$ coevaporation
EF	2000	5	7	$FeCl_2$ coevaporation
EH	4000	9000	3	NaCl coevaporation

With the introduction of chlorine doping of CdSe (Ref. 1), a major obstacle to the production of high g_m TFT's has been overcome.

The principal obstacles remaining are directly related to changes in the semiconductor-dielectric interface and the semiconductor itself. Electronic states exist at the interface which have an electric field associated with them which penetrates a finite depth into the semiconductor. If the states are acceptor states, the associated electric field is such as to prevent an applied field from modulating the semiconductor conductivity until a sufficient DC bias is applied to overcome the field caused by the interfacial states. The density of the surface states is a function of time and temperature. The shift in DC bias has been observed to be larger for devices under continuous operation than those which have only been subject to short testing periods. These results are summarized in Table II. The shifts are probably due to the diffusion of an atmospheric constituent, probably oxygen, through the SiO to the interface. The heating resulting from device operation (Ref. 2) would increase the diffusion rate, explaining the comparatively large change in those devices under continuous operation. Also compatible with the hypothesis is the observation that experimenters using thinner SiO films have observed rapid deterioration of device characteristics. This is attributable to the exponential dependence of concentration of diffused material on distance from the surface.

Four avenues of attack on this problem appear promising. The first is to find a dielectric through which the diffusion rate is reduced. The second is to overcoat the devices with a thick film to increase the effective distance for diffusion. The third is to saturate the interface with states which would prevent any further changes from taking place. The fourth is to find some way of passivating the surface of the semiconductor. An experimental program will be conducted in an attempt to find a practical and effective means of accomplishing one of the above.

REFERENCES

1. D. Abraham and T. O. Poehler, Bull. Am. Phys. Soc., Vol. 10, No. 4, 1965, p. 533.
2. D. Abraham and T. O. Poehler, J. Appl. Phys., Vol. 36, No. 6, June 1965, pp. 2013-2020.

Table II

Life Test Results for CdSe TFT's

Specimen*	V_g (initial) (volts)	V_g (final) (volts)	Continuous Operating Time (hours)	Specimen**	V_g (initial) (volts)	V_g (final) (volts)
DJ 7	3.8	6.0	2496	DJ 4	3.0	6.0
DM 3	4.5	7.5	2496	DM 10	4.5	6.5
DN 6	3.0	5.8	2496	DN 4	3.0	6.0
DO 7	4.5	6.8	2496	DO 4	4.5	5.5
DW 9	2.5	5.6	2496	DQ 2	2.5	5.0
DR 4	4.0	5.9	2496	DR 2	4.5	5.5
DS 4	3.0	9.5	2496	DS 7	3.0	8.0
DT 4	1.5	8.5	2496	DT	1.5	7.5
DU 7	2.6	10.5	2040	DU	2.5	9.0
DV 4	3.9	11	2040	DV	4.5	8.5
DW 5	4.7	10.5	1872	DW	4.5	9.0
DX 6	3.2	10	2304	DX	3.5	7.5
DY 6	5.0	11	2040	DX	4.5	10.0

* Specimens aged subject to continuous operation.

** Specimens aged without applied power.

RESEARCH AND EXPLORATORY DEVELOPMENT 111/15b
Thin Film Microelectronics A35CME
Support: RMGA-8 (BuWeps)
D. D. Zimmerman
April - June 1965

THIN-FILM RESISTOR STUDIES

A study of thin film vacuum deposited resistors is being conducted to determine the optimum process parameters for producing thin film resistors with high yield, stability, and precision. Through investigation of the electrical, physical, and thermal properties of these resistors, progress toward the improvement of passive thin film resistors for use in missiles and missile systems is being achieved.

SUMMARY AND CONCLUSIONS

A technical paper was prepared and delivered at the Fourth Annual Microelectronics Symposium of the IEEE, St. Louis Section, May 24, 1965, on "Evaporated Single Element Metal Film Resistors." The paper was published in the proceedings of the symposium. The experimental processes used to investigate the properties of thin film resistors and the resulting resistor characteristics were discussed in this paper. The major conclusion drawn in the paper is that thin film resistors made from the single element metals, aluminum, chromium, tungsten, and rhenium can be made to reliably satisfy almost all the needs for resistors in thin film microelectronic circuit applications.

Thermal pulsing of resistors can be used to trim thin film resistors to a value within specified tolerances. An automatic thermal pulser was fabricated during this quarter and put into service.

A universal precision resistor probe was designed for use in conjunction with the automatic thermal pulser. It will be fabricated as soon as the drawings are completed.

Life tests on rhenium resistors have passed the 10,000-hour mark with 100 milliwatts of power applied. Resistors with sheet resistance values up to 5000 ohms/square have shown a stability under load of less than 1 percent change. Sheet resistance values between 5000 and 25,000 ohms/square have changed in value less than 4 percent under load for 10,000 hours. Nine rhenium resistors with sheet resistance values ranging from 27,000 to 55,000 ohms/square have been on shelf-life test for 13,000 hours. The resistance increase observed during this test ranges from 0.4 percent to 1.1 percent. Rhenium resistors which were coated with magnesium fluoride failed catastrophically within a 3-month period of shelf-life testing.

The resistor life test component hours accumulated to date is summarized in Table I.

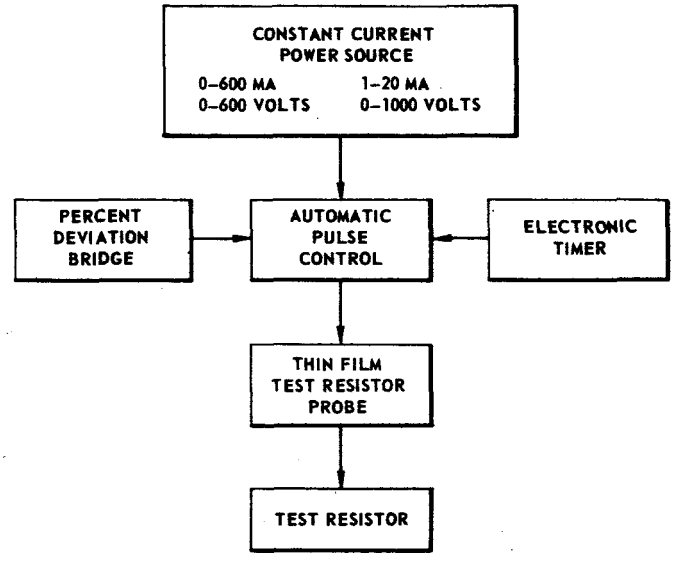

Fig. 1 Block Diagram of Automatic Thermal Pulser for Thin Film Resistor Trimming. (76538)

Table I

Total Component Hours of Resistor Load Life Tests

Resistor Material	Component Hours
Tungsten, Molybdenum, Rhenium with MgF_2	1.58 million
Chromium	1.19
Rhenium with SiO	.36
Total	3.13 million

FUTURE PLANS

Studies of thin film resistors will continue in support of the prototype production effort. Load-life and shelf-life tests of rhenium resistors will be continued.

A design of an electrical test module for 1-inch-square substrates will be developed to accommodate breadboard packaging of 3 to 5 substrates into a unit for testing prior to final assembly in a configuration closely simulating the final package.

BACKGROUND

The usefulness of thin film resistors in microelectronic circuits is enhanced by ultimate control of the process parameters which affect precision, yield, stability, and reproducibility. A comprehensive study has been undertaken to investigate the electrical, mechanical, and thermal characteristics of thin film resistors. The objectives of this study are to identify and optimize these fabrication process parameters. The first phase of this work was devoted to evaporation of chromium resistors on glass microscope slide substrates coated with a silicon monoxide protective film.

The second phase of the chromium resistor work was similar to the first phase and was completed using substrates of Corning glass number 7059 and aluminum conducting lands. Studies of resistors in 500° C air environment were made.

A third phase of resistor studies was introduced, using rhenium metal as the evaporated thin film resistor material. The study of chromium and rhenium resistors is continuing with the use of the electron bombardment evaporation technique.

Solutions to variations in resistor tolerance on a single substrate are being developed through a study of the optical density gradients of thin films.

Automatic thermal pulsing is now being used to trim the thin film resistors to values within specified tolerances.

DISCUSSION

The automatic thermal pulsing equipment which was fabricated and put into service during this quarter consists of a constant current power source to provide the electrical power for the thermal pulse; a decade resistance bridge to measure the resistor value; and an electronic timer to determine the length of time of the pulse and measure cycles. Also, the necessary switching functions are provided by relays and associated circuitry. The constant current source is designed for digital selection of direct current over the range of 1 to 600 milliamperes in one milliampere steps with 0.1 milliampere steps below 20 milliamperes. Resistance measuring is provided by a Wheatstone bridge with a digital selection range from 1 to 100,000 ohms. The percentage deviation readout is accurate to 0.05 percent. The electronic timer has two separate adjustments for selecting the measure and pulse cycles independently over a range of time from 1 to 100 seconds. A simplified block diagram of the automatic thermal pulsing equipment is shown in Fig. 1.

RESEARCH AND EXPLORATORY DEVELOPMENT 111/15c
Thin Film Microelectronics A35CME
Support: RMGA-8 (BuWeps)
L. A. Twigg
April - June 1965

PRODUCTION AND PROTOTYPE FABRICATION

The purpose of this effort is to fabricate prototypes of thin film microelectronic circuits for use in Navy missiles and missile systems. The technology applied in the fabrication of these circuits is the product of the Microelectronics Group's research and development program on thin-film microelectronics components.

SUMMARY AND CONCLUSIONS

One unit of the direct coupled operational amplifier (DCOA) has been completed and is operating satisfactorily. Five units of substrate No. 1 are ready for thermal trimming. Five units of substrate No. 2 are ready for thermal trimming. Production on substrate No. 3 has begun. Thermal trimming is providing a fabrication facility for obtaining close value resistors and higher production yields.

Preliminary assembly has been completed on the new vacuum evaporation carrousel for prototype and production work. Both mechanical and electrical debugging are under way.

FUTURE PLANS

Five units of substrate No. 3 will be completed, and additional DCOA packages will be ready for test.

The new prototype and production carrousel should be ready for installation in the production vacuum unit.

DISCUSSION

Close control of the various component design parameters in the present thin-film production system has been most difficult. This is due, by and large, to inherent incapabilities of the system when circuit and component production of this caliber is considered. But, as in all progressive research work, capabilities as well as shortcomings of equipment always raise questions and often supply answers that would have been otherwise overlooked or by-passed.

Because of the physical inability within the system to correlate monitor values with circuit resistances, a major effort was expended to establish as precise control as possible over evaporation rate, times, currents, temperature, etc. These steps resulted in a greater number of circuits with components in the ±10 to 15 percent range, still too far from the design values, and too low a yield, but a step in the right direction. The thermal pulsing program was initiated to determine the degree of correction possible of filmed and overcoated circuit resistors and to study the gains and losses accrued in the process. The thermal pulsing program has been very successful with most favorable results on rhenium and chromium resistors. The thermal trimming electronics and instrument design is reported in Thin Film Resistor Studies.

The basic gains in the thermal trimming operation can be described as follows: (a) 2 to 3 Kohm chromium thin-film resistors of a 250 ohm/square sheet resistivity have been decreased in value by as much as 10 to 15 percent. For these values, trimming requires an approximate power dissipation of some three to four watts; (b) 100 to 200 Kohms rhenium thin film resistors of a 5000 ohm/square sheet resistivity may be decreased in value as much as 30 to 35 percent by dissipating about 4 to 8 watts in repeated steps and more or less maintaining the same power dissipation as resistance decreases, until the resistor reaches design value or stabilizes. Should the resistor stabilize before final desired value is reached, it is necessary to further increase the current to affect a further decrease in value. It should be noted that the maximum power dissipation will produce a red glow in the resistor path and, at this writing, no adverse affects have been noticed when resistors are thus treated; however, should the color approach the orange portion of the spectrum, serious damage to the resistor and the substrate itself may result. The glass substrate will often crack owing to the very large temperature difference in such a small zone.

A circuit read-out station has been designed and installed within the production facility. This station provides a means for measuring the actual value of the unprotected resistors while still at deposition temperature. This facilitates effecting a change should the value be much larger than can be brought within tolerance by trimming. This unit has just been completed and is presently under test. Upon discovery of too high a value, an immediate second deposition can be made to further lower the resistance value to within reach of the thermal trimming phase. This monitoring or read-out step and the second deposition, if necessary, can all be accomplished without breaking vacuum and necessitating another pump down. The internal circuit read-out station also permits continuity check of capacitors which, if fabricated first and checked, may eliminate the subsequently wasted time and materials in depositing resistors on a substrate containing imperfect capacitors.

A technique has also been developed in this quarter for the salvaging of predrilled and machined substrates on which unusable circuits have been deposited. Chemical removal proved to be very damaging to the 7059 borosilicate glass substrates. A means of physical removal was investigated. A 1.0 micron alumina powder was applied, with water, to a felt padded lap and the circuit was removed by polishing. No adverse effects were noted when a second circuit was deposited on the salvaged substrate.

This simple operation, if proved to be completely successful, will save much of the fabrication time consumed and the cost involved in the selection, machining, and precision drilling of the substrates, which heretofore has been lost when circuits were not within tolerance and were discarded.

RESEARCH AND EXPLORATORY DEVELOPMENT III/15d
Thin Film Microelectronics A35CME
Support: RMGA-8 (BuWeps)
G. A. Hillman
April - June 1965

EVAPORATION MASK FABRICATION

The trend toward tighter tolerances, larger aspect ratios, and smaller patterns for increasing component packing densities in thin-film microelectronics makes it necessary to improve methods of artwork preparation, microphotography, and metal-mask fabrication.

The thin-film evaporation mask research and development effort is directed toward improvement in techniques of high quality mask fabrication with respect to: line width, sharpness of edges, thinness of edges, and mechanical durability under prolonged use.

SUMMARY AND CONCLUSIONS

Investigation of techniques for reducing the amount of encroachment or overplating which takes place during evaporation mask electroforming has been continued. It was found that the overall encroachment can be reduced from an average of about 0.75 to about 0.40 mil per aperture by using a double-dip coating of a new high-solids-content, positive working resist.

Employing the new resist makes it possible to deposit resist films greater than 1 mil in thickness. The thickness ranges from 28 to 32 microns. Since the masks are electroformed to only a mil in thickness, the degree of encroachment is reduced.

The fact that the encroachment is not eliminated by depositing microimages of greater than 1 mil in thickness seems to indicate that after developing, the resist microimage is not uniformly thick and that its sides are not perpendicular to the matrix surface.

Quality of aperture edges of masks electroformed using the high-solids-content resist and the low-solids-content resist appears to be essentially the same (Figs. 1 and 2).

FUTURE PLANS

Investigation of the new high-solids-content photoresist will be continued. Effort will be directed toward optimizing the conditions of application, exposure, and development of the resist in order to determine whether it is possible to produce uniformly thick microimages in which the edges are perpendicular to the matrix. If such microimages can be produced, the encroachment or overplating which takes place during evaporation mask electroforming should be eliminated.

BACKGROUND

The development of a technique for electroforming evaporation masks directly onto mask holders was undertaken because it was felt that the problems of support and registration would be simplified in comparison to other electroforming approaches. A nickel sulfamate electroforming bath was chosen because the resulting nickel deposit is exceptionally low in tensile stress (Ref. 1).

Adoption of the stainless steel matrix in place of the low-temperature-melting alloy used earlier for in situ electroforming has simplified the problem of separation of mask from matrix. It has also made it possible to fabricate masks which exhibit a high-quality smooth finish.

The investigation of the possibility of reducing encroachment or overplating by increasing the thickness of the resist image was undertaken in an effort to solve the problem without resorting to more complicated techniques such as step plating.

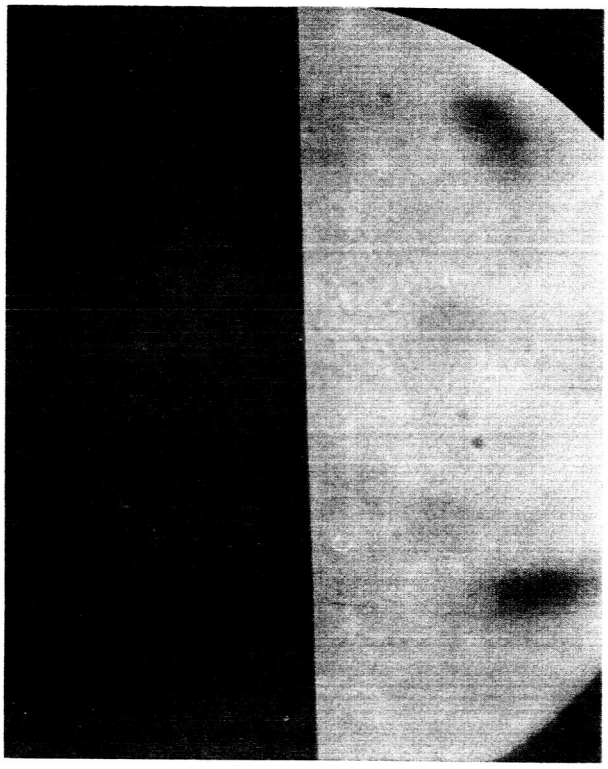

Fig. 1 Aperture Edge of Mask Electroformed Using High-Solids-Content Resist. (76539)

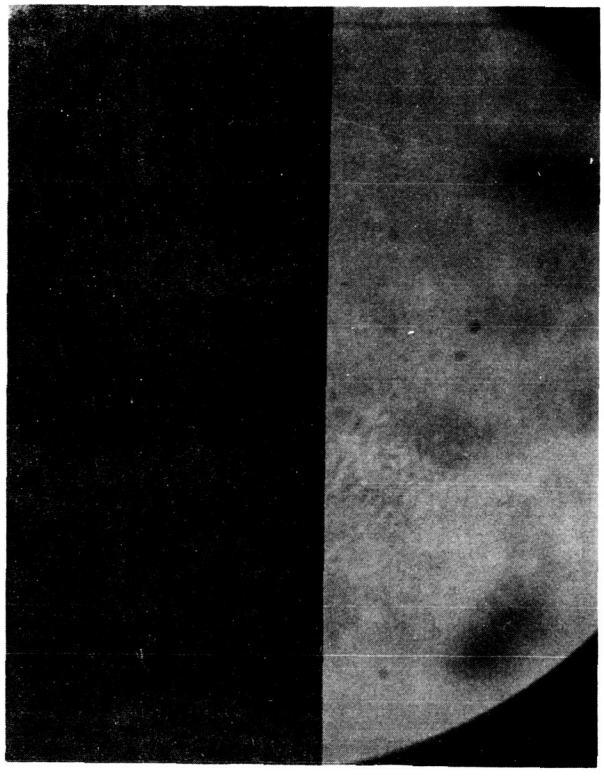

Fig. 2 Aperture Edge of Mask Electroformed Using Low-Solids-Content Resist. (76540)

In general, effort is directed toward reducing the number of photographic processing steps in the mask fabrication procedure since each reduction results in masks of higher quality.

DISCUSSION

A number of photoresist materials were investigated in an effort to find a method of depositing high-quality microimages of greater than 1 mil in thickness. The materials that were investigated included Kodak Photo Resist (Type 2), a composite coating of Kodak Photo Resist (Type 2) over Kodak Metal Etch Resist, Shipley AZ-1340 positive working resist, and Shipley AZ-340 high-solids-content positive working resist.

Various methods of applying the resists were used, such as whirling and pouring in single and double coatings. Thickness measurements were made of the microimages using a Shefield electronic micrometer.

The thickest microimages deposited were 2.5 mils using a composite coating of Kodak Photo Resist (Type 2) over Kodak Metal Etch Resist. The edge definition was poor. The other resists, with the exception of Shipley AZ-340 high-solids-content positive working resist, yielded microimages of less than 1 mil in thickness regardless of the method of application. It was possible to deposit a microimage of good quality with respect to sharpness of edges and dimensions by using a double dip coating of Shipley AZ-340 resist. The thickness of the coating ranged from 28 to 32 microns. A 1-mil-thick mask was electroformed using this coating. It had an average overall encroachment of 0.4 mil per aperture, as compared to 0.75 mil per aperture for state-of-the-art masks.

Microscopic examination of the mask after separation from the matrix indicated that encroachment of approximately 0.2 mil occurred on each edge of an aperture. It appears, therefore, that the sides of the resist microimage are not perpendicular to the matrix surface. This may be due to a drop off in density at the edges of the microimage on the photographic plate which is used in exposing the sensitized matrix.

A study of the condition of the edges of the resist microimage will be undertaken. A number of samples will be prepared at different exposure times using a chromium pattern deposited on a glass plate 2 inches square instead of a photographic plate (Ref. 2). The density of the edges of the resist microimages will be determined with a recording densitometer.

If it is possible to produce sharp microimage edges which are perpendicular to the matrix using metallized plates, they will be adopted in place of the Kodak high resolution plates.

REFERENCES

1. Symposium on Electroforming, ASTM Technical Publication Number 318, 1963, p. 19.
2. R. C. Ingram, "Photolithographic Masks for Integrated and Thin Film Circuitry," Semiconductor Products, March 1965, p. 40.

RESEARCH AND EXPLORATORY DEVELOPMENT I II/15e
Thin Film Microelectronics A35CME
Semiconductor Microelectronics A35CME
Support: RMGA-8 and RREN-4 (BuWeps)
V. Uzunoglu and G. J. Veth

MICROELECTRONIC SYSTEM DEVELOPMENT

The Microelectronics Circuit Design Project within the Microelectronics Group engages in various tasks for the Bureau of Naval Weapons (BuWeps) which are not undertaken elsewhere. These activities are directed toward the application of all forms of microelectronics – thin film, semiconductor, and hybrid.

SUMMARY AND CONCLUSIONS

The microelectronic AC summing amplifiers, modulator/demodulators, and gyro temperature controllers were received from General Electric Ordnance Division to conclude APL subcontract 181456. These circuits were spot checked and the data compared to the data obtained by G. E. Though the circuits in general fall short of the contract specifications, in terms of the magnitude of the task, the time schedule, and the cost, G. E. obtained satisfactory results.

A visit was made to Melpar to check on the progress of an all thin film AC summing amplifier they are fabricating for BuWeps (RREN-4). One unit has been fabricated and is working as a breadboard. This unit will be forwarded to APL for evaluation after it has been encapsulated and checked out.

During the testing of field-effect transistor input stages in the particle detector breadboard, the performance observed suggested that these field-effect transistors could be used to fabricate a useful phase-lock loop arrangement with a single source if they were properly connected with two other particle detector circuits, a feedback pair and a semiconductor delay element.

DISCUSSION

Six each, summing amplifiers, modulator/demodulators, and gyro temperature controllers were received from General Electric Ordnance Division. All the units were checked to see if they were operative, and the units upon which G. E. obtained data were spot checked to verify G. E.'s data.

Summing Amplifier--Gains on this unit were lower by a factor of 20 to 60 than the initial contract specifications, (open loop current gains are 150 to 450 instead of 10,000). Because of this low amplifier gain, many of the characteristics which are functions of gain, such as the sensitivity measurements, are not as meaningful. These low amplifier gains are relatively constant with temperature, and could approach the specified gain of 1.0 ± 0.03 percent if either the input or feedback resistors were tailored.

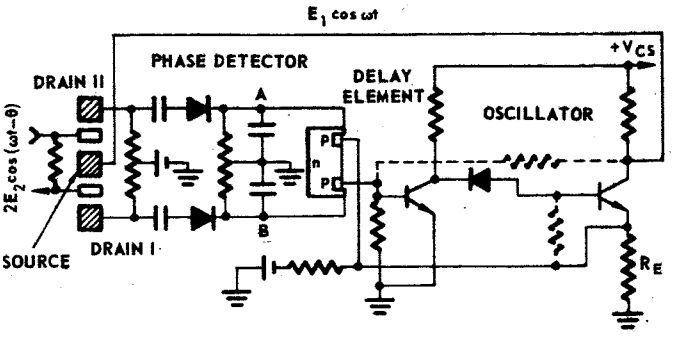

Fig. 1 Complete Phase-Lock Loop Circuit. (76541)

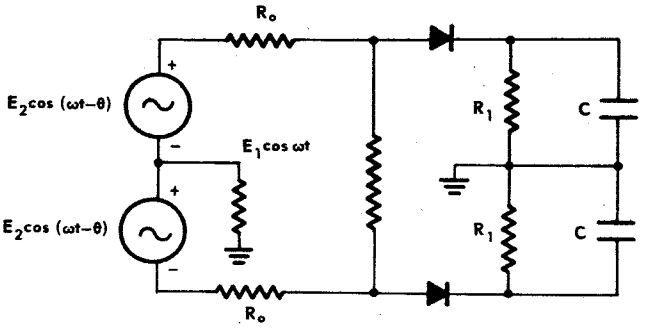

Fig. 2 Equivalent Circuit of the Phase Detector. (76542)

Modulator/Demodulator--Essentially, this circuit meets most of the initial contract specifications except for the temperature drift. The temperature drift of the output is about two orders of magnitude greater than the initial specification. The offsets of the units are kept within specification by proper selection of a conventional resistor in the amplifier.

Gyro Temperature Controller--This circuit is the best of the three circuits in terms of the initial contract specifications. At a given ambient temperature these circuits are capable of holding the gyro temperature to the ±0.2 percent specified, but their nominal temperatures vary to ±10°F of the nominal 190°F specified. Assuming it is the variation in temperature rather than the absolute temperature which is important, this circuit performs reasonably well. The nominal temperature varies about ±1°F in the chamber enclosing the circuit and gyro for ambient temperature

changes of ±100°F. This variation is dependent on the gyro temperature chamber thermal design and the chamber used was not of the best design with respect to the circuit mount.

Correction of the problems existing in the three circuits would require circuit redesign more than fabrication refinement. Use of these circuits would require acceptance of the characteristics as is, with only relatively minor improvements resulting from fabrication refinements.

Actual data on these circuits in the form of a final report issued by the Ordnance Department of the General Electric Company are available through the Microelectronics Group.

Phase-lock loops, which ordinarily use balanced transformers, oscillators and voltage sensitive elements to control the voltage, can be simplified using semiconductor elements such as shown in Fig. 1. A phase-lock loop generally consists of a phase detector comprising two field-effect transistors with a common source, a delay element, and a two-stage oscillator. The input signal is applied to the two gates of the phase detector and this is compared to a signal of $E_1 \cos\omega t$ taken from the output of the oscillator. The difference in phase of these two signals is detected as a DC voltage across A-B of the phase detector, which in turn controls the field across the delay element. Any variation of the field will be reflected as a variation in phase shift or delay to the oscillator signal taken across the output of the oscillator. Thus, the output of the delay element synchronized through the variation of the field will control the frequency of oscillation of the oscillator. The equivalent circuit of the phase detector is shown in Fig. 2.

It can be shown that the output of the phase detector is varying as a function of $\cos\theta$; θ equals the phase difference. Thus, by applying a field across the delay line as a function of $\cos\theta$, we are able to vary the frequency of oscillation according to this function. In this case, the locus of oscillation frequencies will be a function of $\cos\theta$, assuming that the delay element introduces a variation proportional with $\cos\theta$. Although this technique introduces a perfect control on the oscillator, the variation of the oscillating frequencies will be a function of $\cos\theta$. But, it is always possible to have a delay line which introduces a linear delay with $\cos\theta$.

The delay element consists of a semiconductor region with two diffusions. (See previous APL/JHU quarterly reports on microelectronic system development for discussion of delay element.) The two outside ohmic contacts on this element are the control field application points. The diffused area on the left is used to inject the minority carriers of the oscillating amplifier, while the right hand junction is used to collect the minority carriers.

The oscillator is a double-diffused, direct-coupled, two-stage amplifier with two positive inherent feedbacks which cause the oscillations. The positive feedback paths are shown in a dotted pattern in Fig. 2. The output of the oscillator is fed back through R_E and the delay element to the input of the oscillator.

Calculations indicate this circuit to be feasible with present techniques; however, more extensive experimental verification would be needed.

RESEARCH AND EXPLORATORY DEVELOPMENT III/16a
Semiconductor Microelectronics A35CME
Support: RREN-4 (BuWeps)
W. Liben
April - June 1965

MICROELECTRONICS ENGINEERING HANDBOOK

Since microelectronics is a relatively new art, there is a serious shortage of textbooks on all phases of microelectronics which may be used for education and training of electronic engineers. To remedy this situation, the preparation of a volume on microelectronics fabrication methods and a second volume on microelectronic circuit and system design procedures has been undertaken.

SUMMARY AND CONCLUSIONS

The first volume on fabrication consists of seven chapters. It has been completed, and 250 copies will be printed in July.

FUTURE PLANS

The second volume in microelectronics circuit design will be started in July; the material preparation should be completed during the next quarter.

DISCUSSION

The first volume on fabrication consists of seven chapters with the following titles:

Chapter I	Microelectronics
Chapter II	The Physics of Semiconductor Devices and Thin Films
Chapter III	Fabrication of Thin-Film Microelectronic Circuits
Chapter IV	Oxidation, Diffusion, and Epitaxy
Chapter V	Semiconductor Microelectronic Fabrication Technology
Chapter VI	Thin-Film Microelectronic Components
Chapter VII	Components of Semiconductor Microelectronic Circuits

The second volume is tentatively made up of the following chapters:

Chapter VIII	Introduction
Chapter IX	Transistor Theory
Chapter X	Circuit Design
Chapter XI	Logic Circuits
Chapter XII	Radiation Damage
Chapter XIII	Reliability
Chapter XIV	Devices under Development

RESEARCH AND EXPLORATORY DEVELOPMENT I11/16b
Semiconductor Microelectronics A35CME
Support: RREN-4 (BuWeps)
G. J. Veth
April - June 1965

FREQUENCY DIVIDER

This effort is directed toward the design of a semiconductor microelectronic frequency divider employing micropower circuitry. This is an ambitious problem because of the specification for low power and the requirement of high speed.

SUMMARY

With the ultimate goal of this project being the realization of a frequency divider utilizing micropower circuitry, the approaches to micropower circuitry have been investigated with respect to the capabilities of microelectronics generally and the capabilities of our semiconductor fabrication center in particular. Considering the present and near-future capabilities of the semiconductor fabrication center, present efforts are being restricted to the use of minimum power circuits consistent with the triple-diffused, junction-isolation process.

Low-power, bistable multivibrator circuits were fabricated, but improper isolation of two steering network diodes kept them from operating in a counting mode. Artwork for the circuit has been corrected, and new circuits are being fabricated.

Investigations in minimum-power-circuit configurations have led to circuit configurations in which power dissipation reductions of up to 25 percent below a binary serial divider appear possible with little or no sacrifice in speed.

FUTURE PLANS

As bistable multivibrator circuits become available portions of the frequency divider will be fabricated. Concurrent with this, investigation will continue in minimum-power circuit configurations compatible with the triple-diffusion junction-isolation fabrication process.

DISCUSSION

The reduction in power dissipation of a conventional discrete semiconductor logic circuit is achieved by:

1. Lowering supply voltages to a minimum consistent with desired logic levels and circuit stability.
2. Increasing all resistances consistent with speed requirements.
3. Employing minimum power circuit concepts such as (a) transistor minimum power circuit configuration, (b) field-effect transistor minimum power circuit configurations, and (c) bipolar and field-effect transistor complementary circuits.

When consideration changes from conventional to microelectronic semiconductor circuits these avenues for conventional circuit power reduction are limited according to the fabrication capabilities available.

Minimum supply voltages are dictated by the thresholds, offsets, and tolerances of the circuit components being used and the desired stability of the circuit with respect to its intended environment. In particular, an investigation of two of the more popular microelectronic forms available -- resistor capacitor transistor logic (RCTL) and diode transistor logic (DTL) -- indicates that a higher supply voltage is required for DTL than RCTL owing to the presence of the level shifting diodes in DTL. The only restriction placed on lowering of supply voltages by the fabrication technology is with respect to the tolerances on components, especially resistors. In the construction of conventional circuits, 5 to 10 percent resistor tolerances are common, whereas in semiconductor integrated circuits 15 to 20 percent tolerances are more common for reasonable processing yields.

Increasing circuit resistance is limited by the maximum speed of operation and by the leakage currents in junction-isolated circuits. In junction-isolated circuits, the ohms/square of the resistors are generally limited by the active element of the circuit. For circuits using bi-polar transistors the ohms/square is in the range of 100 to 1000. Thus, to increase a circuit resistance, the length of the resistors must be increased. This increases the total leakage current into or out of the resistor. As the leakage current is increasing, the signal current is decreasing until a point is reached where the static stability of the circuit is marginal or where the leakage power dissipation is increasing faster than the circuit power dissipation is decreasing.

Two approaches are available to reduce the leakage currents associated with junction-isolated resistors. One is to deposit metal film resistors over the circuit oxide, and the second is to use oxide isolation instead of junction isolation. The first has been used by CBS Laboratories to produce micropower DCTL circuits. These two techniques, besides significantly reducing leakage currents, also reduce the parasitic capacitances associated with the resistor and therefore increase the maximum frequency of operation of a circuit.

In considering minimum power circuit configurations, complementary logic types are attractive. At present, complementary bipolar or field-effect transistors are not being effectively fabricated in semiconductor integrated circuits. The inclusion of complementary structures would require an evaluation of the complementary structures possible in integrated circuits with respect to active device

requirements for use in micropower complementary circuits. This requires the ability to fabricate a variety of complementary structures. In terms of fabrication complexity, additional diffusions are required to make complementary structures over single-type structures with additional controls on the oxide characteristics and thickness if metal-oxide-silicon (MOS) field-effect transistors are being fabricated.

Integrated circuits employing only field-effect transistors are capable of lower power dissipations than bipolar transistor circuits, but are not capable of as high an operating speed. Optimization of field-effect transistors requires diffusion schedules which are different from those used for making bipolar transistors besides requiring control of oxide characteristics and thickness when considering MOS field-effect transistors.

Since the present effort in the CME semiconductor fabricating center is directed toward establishing a reliable triple-diffusion process capable of producing a micropower transistor, many of the avenues to micropower circuitry as discussed must be ignored until the capabilities of the fabrication section are extended. Thus the frequency divider is being designed using minimum power circuits consistent with the triple-diffused junction-isolation process.

In this connection, a new division technique developed by NASA that uses bipolar transistors and that promises about a 25 percent power dissipation reduction compared to a straight serial binary division chain is being investigated.

First attempts at fabricating the initial astable multivibrator stage of the frequency divider were unsuccessful. Therefore, it was decided to fabricate one of the other less critical bistable multivibrator circuits capable of binary division. Bistable multivibrator circuits were produced which operated as static flip-flops, but would not operate in a counting mode. Subsequent investigations disclosed that two of the diodes in the steering network of the circuit were not properly isolated, thus inhibiting proper operation of the steering network. This was corrected by an isolation mask change. More circuits are now being fabricated.

RESEARCH AND EXPLORATORY DEVELOPMENT III/17
Radiation Damage Studies A35CME
Support: DASA through RMGA-8 (BuWeps)
R. A. Freiberg
January - June 1965

NUCLEAR RADIATION STUDIES

This effort is to assist the Missile Guidance and Airframe Branch, Bureau of Naval Weapons, with their study, supported by the Defense Atomic Support Agency (DASA), on the effects of transient nuclear radiation on missile electronics (TRE).

SUMMARY

Activities supporting this program for the six-month period through June are listed below:

During the week of January 18 to 22, insulated-gate thin-film cadmium selenide transistors (TFT's) from Melpar were irradiated with a direct electron beam equivalent to a gamma flux of 10^9 to 10^{10} roentgens/sec in the Hughes Linear accelerator (LINAC). A report of these results was furnished to BuWeps for program direction (Ref. 1). This test was preceded by a meeting at Melpar on January 7.

A second series of tests using the Melpar devices was conducted during the week of March 1-5 in the Hughes LINAC to extend the results of the first series. A report on this series has not yet been distributed, but the results have been made known to BuWeps.

On March 12 a DASA Microelectronic Working Group Meeting was hosted at APL. A good portion of the results of the second test series on TFT's was disclosed then.

On March 24 representatives of Naval Avionics Facility, Indianapolis (NAFI) and PID of BuWeps visited APL to discuss the first series results.

On April 5 the Hughes Aircraft Company was visited to review Navy sponsored TRE studies.

On April 7 a paper, essentially on the results of the first thin-film tests, was given at the Navy Microelectronic Conference at Monterey, California.

On April 8, Varian Associates and Physics International, Palo Alto, California, were visited to discuss the linear accelerator and the flash X-ray, respectively.

On April 12 and 13, APL hosted the Second Navy Symposium on the Transient Effects of Nuclear Radiation on Electronics (TRE) at Howard County. All services were represented. A presentation of the up-dated results of the two thin-film tests was given again.

On April 20 a visit was made to the Naval Research Laboratory (NRL) to discuss their TRE problems and to visit their LINAC facility.

On May 12th, a DASA Microelectronic Working Group Meeting called by Rome Air Development Center (RADC) was attended at Fort Monmouth, New Jersey, as a BuWeps representative.

On June 1, 2, and 3 the annual DASA TRE Project Officers meeting was attended at the Pentagon.

FUTURE PLANS

Participation as assistant to RMGA-8 of the Bureau of Naval Weapons will be continued.

DISCUSSION AND BACKGROUND

TRE studies sponsored by RMGA of BuWeps are being conducted by the Hughes Aircraft Company. These studies now are concentrating on testing all-thin-film microelectronic circuits supplied principally by Melpar, Incorporated, for high temperature (<500°C) operation in a nuclear environment. The reported tests have been of an explorative nature for the purposes of assisting BuWeps in program definition. Several important defining results were noted which can be stated qualitatively here.

1. Supposed TFT instabilities proved rather to be the problem of establishing equilibrium which was controlled by modifying instrumentation and experimental procedure.
2. TFT output disturbances during radiation were not causing saturating currents from the device at 10^{10} roentgens/sec and the output essentially followed the radiation pulse time history except for a small tail.
3. A great part of the disturbance was determined to be very dependent upon the surrounding air-pressure, insulation, and device topology.
4. A method of isolating the various contributions to the overall effect has been outlined by using up to nine-device-configuration permutations. Three of these permutations were used in these tests.

The results and analysis have suggested new and modified tests which are being instrumented.

For prior background, the interested reader is referred to Ref. 2.

REFERENCES

1. R. Freiberg, "Radiation Effects on the Thin-Film Field-Effect Device" (Unclassified), APL/JHU report for BuWeps, January 18-22, 1965.
2. R. A. Freiberg, "Nuclear Radiation Studies," Section III/14, Research and Exploratory Development for the Missile Guidance and Airframe Branch, Bureau of Naval Weapons, Quarterly Report, July-September 1964 (Unclassified), APL/JHU GQR/64-3. (Section also in RQR/64-3.)

RESEARCH AND EXPLORATORY DEVELOPMENT 111/19a
Advanced Warhead Supporting Research A42BFM
Support: RMMO (BuWeps)
W. C. Welsh
January - June 1965

GUIDANCE AND FUZE INVESTIGATIONS

The validity of comparative studies of the effectiveness of various high-explosive warheads depends upon realistic assumptions about missile guidance and fuze performance.

SUMMARY AND CONCLUSIONS

To improve effectiveness analyses, the performance of Terrier, Tartar, and Talos missile guidance and warhead fuzing was examined using all available results from missile test firings as the primary source of information.

Miss distance data and time sequence recordings of fuze operation indicate that an assumption of a Gaussian distribution of errors may be inappropriate to descriptions of guidance accuracy or fuze operation. In light of these data, the parameter sigma, σ, customarily used to quantify performance, appears inadequate to describe operational errors.

More satisfactory descriptions of guidance and fuzing error functions are precluded by limitations of the information-gathering-techniques. Significant improvement in quality and detail of information reported from missile tests must be achieved to permit accurate definition of the error functions.

FUTURE PLANS

This phase of the warhead supporting research investigation into guidance and fuze performance is complete. No further studies of performance history are planned.

Continued effort will be directed toward examination of guidance and fuzing concepts as applicable to improvements in effectiveness of current warheads and to innovations required by novel warhead concepts.

BACKGROUND

Though computer simulations are commonly used in warhead effectiveness analyses, the relevance of the simulations is contingent upon appropriate description of system performance. The objective of these studies was to provide up-to-date descriptions of guidance and fuze performance which could be utilized to enhance the efficacy of computer simulations in effectiveness evaluations.

Analysis of data from missile test firings indicated that the instruments for obtaining missile test data and data reduction discrepancies among the reporting agencies effected inaccuracies, inconsistencies, and inadequacies in the data which preclude formulation of well-defined descriptions of guidance and fuze performance. The data from firing tests do not support unqualified use of normal distribution functions to describe guidance accuracy and fuze dispersion; in fact, several other distribution functions, namely a translated normal, a bi-modal normal, a Wiebull, and an exponential also provide at least as good a description of the distribution of guidance errors.

Instrumentation of the missile test firings is currently limited in its ability to provide adequate information pertinent to evaluation of ordnance effectiveness.

REFERENCES

1. W. C. Welsh, "Missile Intercept Accuracy — Improved Tartar, Terrier HT-3/3A, and Talos 6c1/6b1 CW" (U) (Confidential), APL/JHU CLA-1151, 31 March 1965.
2. W. C. Welsh, "Warhead Fuzing Status Report" (U) (Secret), APL/JHU CLA-1152, 1 June 1965.

RESEARCH AND EXPLORATORY DEVELOPMENT 111/19e
Advanced Warhead Supporting Research A42BFM
Support: RMMO (BuWeps)
R. L. McCally
April - June 1965

EXPLODING-WIRE SHOCK INTENSITY

Exploding wires are being considered for use as initiators of intermediate and secondary explosives. The initiation mechanism of an exploding wire, however, is not well understood. Leopold (Ref. 1) feels that the cause of initiation must be something other than shock; while the results of Muller, Moore, and Bernstein (Ref. 2), using loosely packed RDX, were characteristic of shock initiations. A study of the thermal aspects of initiation is being made (Ref. 3); however, it is felt that a concurrent experimental program to study the shock waves from exploding wires is necessary. The combined results of these studies should give a set of criteria for an exploding wire to be a good initiator.

FUTURE PLANS

Work on this project was recently started. At this time the experimental equipment is being assembled.

Obviously the first question to be answered is whether the shock is strong enough to cause initiation. Seay and Seely (Ref. 4) found that 2.5 kilobars is the minimum shock pressure that will initiate loosely packed (1.0 gm/cc) PETN. Secondly, methods of maximizing the shock strength must be found. To accomplish this, each of the parameters that affect shock strength will be studied separately. These parameters can be broken into two, not entirely independent, groups: parameters of the circuit and wire parameters. These are listed in Table I.

Table I

Parameters That Affect Shock Strength

Circuit Parameters	Wire Parameters
Total Energy Stored	Length
Rate of Energy Deposition	Diameter
Resistance	Material
Capacitance	
Inductance	

Transparent materials, probably liquids, will be used for the first experiments because the shock can be viewed as it passes through the material and as it leaves. The materials used will have densities between one and two grams per cubic centimeter because most explosives have similar densities. The idea here is to approximate an explosive by a nonreactive material. Eventually several materials of varying densities will be studied. It will be interesting to see if Lin's theory (Ref. 5) for strong cylindrical shock waves in gases holds for liquids and solids. His theory predicts:

$$R = S(\gamma)\left(\frac{E}{\rho_o}\right)^{\frac{1}{4}} t^{\frac{1}{2}},$$

where R is the radius of the shock front at time t, E is the energy in the shock, ρ_o is the ambient density, and $S(\gamma)$ is a function only of $\gamma = C_p/C_v$. Thus, if Lin's theory holds, a plot of $(2R)^2$ versus t would be a straight line.

BACKGROUND

Bennett (Refs. 6 through 8) has done a great deal of work on the shock waves produced in air and other gases by a wire explosion, but no record has been found of quantitative measurements of the shocks in liquids or solids. Baird (Ref. 9) observed shock waves in glass from the explosion of an embedded wire; but, he made no measurements. Therefore, this may be a useful area of study.

Shock waves are described by the Rankine-Hugoniot equations expressing conservation of mass, momentum, and energy, respectively

$$\rho_o U = \rho\,(U - u)\,,$$

$$P - P_o = \rho_o\, U\, u\,,$$

$$E - E_o = \frac{P + P_o}{2}\left(\frac{1}{\rho_o} - \frac{1}{\rho}\right),$$

where u is the particle velocity, U the shock wave velocity, ρ the density, P the pressure, and E is the specific energy. The subscript o refers to the unshocked material immediately ahead of the shock front and no subscript refers to the shocked material behind the wave. Thus a shock can be completely described by its velocity, the particle velocity, and the density of the unshocked material.

The particle velocity cannot be measured directly; however, it can be obtained by measuring the free surface velocity (v_{fs}) as the shock exits the material. Then:

$$v_{fs} = u + u_r ,$$

where u_r is the particle velocity due to the rarefaction wave propagating back into the material from the surface. In general:

$$\frac{u_r}{u} \approx 1 ,$$

and, therefore, $u \approx \frac{1}{2} v_{fs}$.

This approximation has been investigated by Walsh and Christian (Ref. 10) and found to be an excellent one; viz., accurate to within 1 percent and more typically to within 0.5 percent.

An STL image converter streak camera will be used for the velocity measurements.

REFERENCES

1. Howard S. Leopold, III, The Effects of Wire Diameter on the Initiation of PETN by Exploding Wires, NOL TR 64-2.
2. G. M. Muller, D. B. Moore, and D. Bernstein, "Growth of Explosion in Electrically Initiated RDX," J. Appl. Phys., Vol. 32, No. 6, 1961, p. 1065
3. R. L. McCally, "Initiation of Explosives," Section III/19c, Research and Development Programs Quarterly Report January - March 1965 (Unclassified), APL/JHU U-RQR/65-1.
4. G. E. Seay and L. B. Seely, Jr., "Initiation of a Low-Density PETN Pressing by a Plane Shock Wave," Third Symposium on Detonation, held at James Forrestal Research Center, Princeton University, September 26-28, 1960, NOL (White Oak) and ONR, p. 562.
5. Shao-Chi Lin, "Cylindrical Shock Waves Produced by Instantaneous Energy Release," J Appl. Phys. Vol. 25, No. 1, 1954, p. 54.
6. F. D. Bennett, "Cylindrical Shock Waves from Exploding Wires," Phys. of Fluids, Vol. 1, No. 4, 1958, p. 347.
7. F. D. Bennett, Energy Partition in Exploding Wire Phenomena," Phys. of Fluids, Vol. 1, No. 6, 1958, p. 515.
8. F. D. Bennett, "Shock Producing Mechanisms for Exploding Wires," Phys. of Fluids, Vol. 5, No. 6, 1962, p. 891.
9. K. M. Baird, "Shock Waves in Glass," Nature, Vol. 160, No. 24 (1947).
10. John M. Walsh and Russell H. Christian, "Equation of State of Metals from Shock Wave Measurements," Phys. Rev. Vol. 97, No. 6, 1955, p. 1544.

RESEARCH AND EXPLORATORY DEVELOPMENT 111/19f
Advanced Warhead Supporting Research A42BFM
Support: RMMO (BuWeps)
S. D. Raezer
April - June 1965

EXPLODING-WIRE RESEARCH

Long exploding wires (12 inches and longer) are being considered as a means of line initiation of explosives. The aim is to avoid the use of sensitive primary explosives as initiators, achieve directional explosive patterns, and generally improve initiation and detonation of explosive charges in guided missile warheads. The work is proceeding in cooperation with theoretical analysis of the detonation process in solids and comparative warhead analysis.

Information on small exploding wires of various diameters and materials is abundant but not usually in a form which would allow accurate extrapolation of electrical energy requirements to long wires. What is needed is a simple means of predicting energy requirements for long exploding wires from information acquired from exploding shorter wires.

SUMMARY AND CONCLUSIONS

A correlation has been established experimentally between the electrical energy required to just melt and also to just burst No. 40 copper wires of various lengths, and the length of the wire. The correlation is shown in Fig. 1. The tests were performed using two different sets of electrical circuit constants. The energy to just melt and also to just burst the wire was computed. The results are given in Table I. The conditions of "just melted" and "just burst" were identified by the "card-print" technique described below.

FUTURE PLANS

It is planned to extend the above work to a range of wire materials. Tabulations of the parameter R as a function of H for homogeneous heating along with correction factors for non-homogeneous heating should allow a rapid comparison of the effectiveness of different materials as used with specific electrical circuits.

In addition to this work, apparatus has been constructed for the exploding of 12-inch wires and for testing their potential as detonators of secondary explosives by direct experiment. Also, some continuation of the work on trigger gap characteristics (Ref. 1) and amplification of spurious transients resulting from the negative resistance properties of the trigger arc (Ref. 2) is planned.

BACKGROUND

Exploding wire research to date has included review of the literature on the subject,

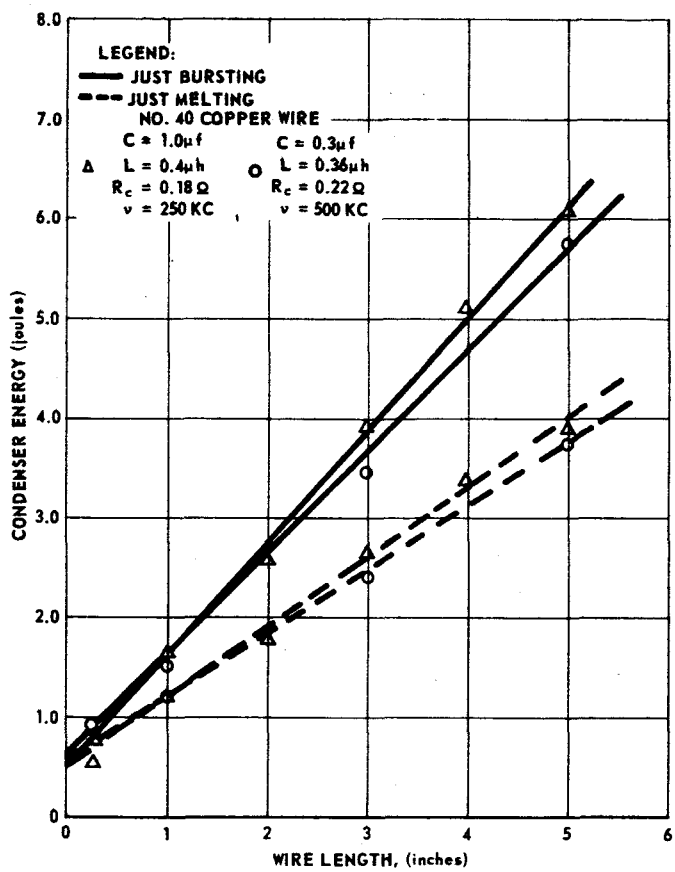

Fig. 1 Circuit Energy versus Wire Length. (76504)

with particular regard to measurement techniques and electrical circuitry. Comprehensive theories are unavailable as a result of the complexity of the overall exploding wire system. Present efforts at APL have centered on obtaining systematic data which will serve as a guide for future refined measurements. For this purpose, a simple adiabatic, homogeneous exploding wire model has been postulated for which the state of the wires may be described in terms of two parameters S = S (R, H) where R is the average resistivity throughout the transition from initial to final state and H the energy released in the wire per unit mass. Under these conditions, the relationship between total circuit energy

Table I

No. 40 Copper Wire

C	r_c	L	D	ρ	H	R	State	International Critical Tables data: H	International Critical Tables data: R
μf	ohms	μh	in.	gm·cm^{-3}	cal·gm^{-1}	μohm·cm		cal·gm^{-1}	μohm·cm
1.0	0.18	0.40	0.0031	8.89	148	4.9	melt	155	~5.0
					236	7.9	burst	264	--
0.30	0.22	0.36	0.0031	8.89	137	5.0	melt	155	~5.0
					233	7.8	burst	264	--

$$U = 1/2\ C(V_i^2 - V_f^2)\ ,$$

where

U = total circuit energy,
C = condenser capacity,
V_i = initial condenser voltage, and
V_f = final condenser voltage,

and wire length, ℓ, corresponding to a given state, S, should be expressible in the form

$$U = \alpha + \beta\ell\ , \qquad (1)$$

where $\alpha = \dfrac{r_c A^2 \rho H}{R}$,

and $\beta = \dfrac{R\alpha}{r_c A}$.

Here r_c is the external electrical circuit resistance, A the wire area, ρ the initial density of the wire, and R and H the aforementioned "state parameters."

One simple means of identifying the state S is afforded by the "card-print" technique. If the wire is exploded in contact with a white file card, at low energies the resultant patterns are identifiable and characteristic of a particular energy state. Other such linear indicators can probably be found for identifying higher energy states. Identification of the thermodynamic state S will be helpful in comparing metals and in studying time dependent processes within the metal and the heat transfer mechanisms.

REFERENCES

1. S. D. Raezer, "Spark Gap Characteristics," APL/JHU BFM-001, 5 March 1965.
2. S. D. Raezer, "Controllable Microsecond Time Delay in Air Gap Thyratrons" (unpublished report).

RESEARCH AND EXPLORATORY DEVELOPMENT 111/23
Adaptive Stabilization Computer A62CLM
Support: RMWC (BuWeps)
A. G. Carlton and L. M. Spetner
April - June 1965

ADAPTIVE STABILIZATION COMPUTER

The Adaptive Stabilization Computer program is one of research directed toward the development of a computer to predict ship motion. The prediction will be optimal in the sense that it will tend to minimize the variance of the error and will be based upon measurements of the ship orientation with respect to a stable platform. The computer is intended to adjust its own parameters automatically in order to maintain the prediction optimal under a wide variety of external conditions.

SUMMARY AND CONCLUSIONS

A new procedure has been developed for predicting an unknown stationary process. The essential new feature is the demonstration that any finite-order sampled stationary process can be described by a finite-order difference equation. The parameters of this difference equation can be estimated and then used to obtain an optimum prediction of the process. If the process is Gaussian, then a procedure is available that yields the optimum prediction conditioned on the past data. A technique has also been developed to take account of observational errors.

FUTURE PLANS

Computer simulations of the optimal-prediction procedure will be run in order to check on the dynamic features of the prediction as well as the estimation of the parametric description of the process. Theoretical investigations will also be made of these dynamic features in order to lead to an understanding of the prediction problem for nonstationary processes.

DISCUSSION

If one lets the discrete random process $\xi_o, \ldots, \xi_n$ represent the uniformly sampled values of a stationary, continuous, Gaussian, random process whose power spectral density is the square of the ratio of two polynomials, such that the denominator is of order k, and the numerator is of order less than k, then the sequence $\{\xi_n\}$ satisfies the difference equation

$$\xi_n = g' x_{n-1} + h' v_n , \qquad (1)$$

where the vectors x_{n-1} and v_n are given by

$$x'_{n-1} = [\xi_{n-1} \cdots \xi_{n-k}] \qquad (2)$$

$$v'_n = [\omega_n \cdots \omega_{n-k+1}] , \qquad (3)$$

and where the ω's are independent Gaussian random variables having zero mean and unit variance.

The vectors g and h,

$$g' = [\gamma_1 \cdots \gamma_k] \text{ and} \qquad (4)$$

$$h' = [\eta_1 \cdots \eta_k] , \qquad (5)$$

are taken to be random variables. For convenience the (2k)-component vector f is defined as

$$f' = [g'h'] = [\gamma_1 \cdots \gamma_k \ \eta_1 \cdots \eta_k] , \qquad (6)$$

and its conditional probability density $p(f|x_n)$ can be sequentially estimated as new data are accumulated.

One may define the following:

$$P = \begin{bmatrix} \eta_1 & \eta_2 & \cdots & \eta_{k-1} \\ & \eta_1 & \cdots & \eta_{k-2} \\ & & \ddots & \\ \bigcirc & & & \eta_1 \end{bmatrix} , \text{ a } (k-1) \times (k-1) \text{ matrix;} \qquad (7)$$

$$Q = \begin{bmatrix} \eta_k & & & \bigcirc \\ \eta_{k-1} & \eta_k & & \\ \vdots & & \ddots & \\ \eta_2 & \cdots & & \eta_k \end{bmatrix} , \text{ a } (k-1) \times (k-1) \text{ matrix;} \qquad (8)$$

$$D = I + P'Q^{-1'}Q^{-1}P, \quad \text{a } (k-1) \times (k-1) \text{ matrix;} \qquad (9)$$

$$B = P' \, Q^{-1'}Q^{-1}, \quad \text{a } (k-1) \times (k-1) \text{ matrix;} \qquad (10)$$

$$J = \begin{bmatrix} 0 & & & \\ & \ddots & & \bigcirc \\ 1 & & \ddots & \\ & \ddots & \ddots & \\ \bigcirc & & .1 & 0 \end{bmatrix} , \text{ a } k \times k \text{ matrix;} \qquad (11)$$

$$R = \begin{bmatrix} J & 0 \\ 0 & J \end{bmatrix} , \text{ a } (2k) \times (2k) \text{ matrix;} \qquad (12)$$

$$D^* = \begin{bmatrix} 1 & 0 \cdots 0 \\ 0 & \\ \vdots & D \\ 0 & \end{bmatrix} , \text{ a } k \times k \text{ matrix;} \qquad (13)$$

$$\left.\begin{aligned} \alpha_o &= 1 \\ \alpha_\ell &= \sum_{j=1}^{\ell} \gamma_j \alpha_{\ell-j}, \quad \ell = 1, \ldots, m \end{aligned}\right\} \qquad (14)$$

$$b_n' = [(\xi_n - g'x_{n-1}) \cdots (\xi_{n+2-k} - g'x_{n+1-k})]$$

a (k-1)-component vector; (15)

$$q_n' = [0 \ (D^{-1}Bb_n)'], \text{ a k-component vector;} \quad (16)$$

$$y_n' = [x_n' q_n'], \text{ a (2k)-component vector.} \quad (17)$$

Then the conditional probability density $p(f|x_n)$ is $p(f|x_n) = \text{const} \times \exp\{-\frac{1}{2}(h'D^*h)^{-1}$

$$[(f-\hat{f}_n)' S_n^{-1} (f-\hat{f}_n) + \lambda_n]\}. \quad (18)$$

As a new measurement, ξ_{n+1}, is made, the parameters of $p(f|x_n)$ are adjusted according to

$$S_{n+1} = S_n - \frac{S_n y_n y_n' S_n}{1+y_n' S_n y_n}, \quad (19a)$$

$$\hat{f}_{n+1} = \hat{f}_n + S_{n+1} y_n (\xi_{n+1} - y_n' \hat{f}_n), \text{ and} \quad (19b)$$

$$\lambda_{n+1} = \lambda_n + \xi_{n+1}^2 + \hat{f}_n' S_n^{-1} \hat{f}_n - \hat{f}_{n+1}' S_{n+1}^{-1} \hat{f}_{n+1}. \quad (19c)$$

If $\hat{f}_n' S_n^{-1} \hat{f}_n \gg 1$, the conditional probability density $p(f|x_n)$ of Eq. (18) may be taken to be a Gaussian so that $\hat{f}_n$ becomes the optimum extimate of f.

The optimum prediction of ξ_{n+m} based on measurements up to the n-th time step is the conditional expectation $\langle \xi_{n+m} | x_n \rangle$, and is given by

$$\langle \xi_{n+m} | x_n \rangle = \sum_{j=1}^{m} \left[\int \alpha_{m-j} \, f' \, p(f|x_n) df \right] R^j y_n,$$

where α_{m-j} are the appropriate functions of the components of f as given by Eq. (14).

For an autoregressive process, when all the η's are zero except η_1, a procedure has been developed to allow prediction even when the observation of ξ_n is contaminated by noise ϵ_n.

$$\xi_n = g' (x_{n-1} - \epsilon_{n-1}) + \omega_n + \epsilon_n.$$

The best estimate of the noise ϵ_n turns out to be

$$\hat{\epsilon}_n = \frac{\langle \epsilon_n^2 \rangle}{\langle \tilde{\zeta}_n^2 \rangle} \tilde{\zeta}_n \quad (20)$$

where $\tilde{\zeta}_n \triangleq \xi_n - \hat{g}_n' \hat{x}_{n-1}$,

and where the estimate $\hat{g}_n$ is obtained sequentially as is $\hat{f}_n$ above.

REFERENCES

1. A. G. Carlton, "Adaptive Prediction," APL/JHU CLM-115, 28 April 1965.
2. L. M. Spetner, "Optimum Prediction of a Noise Process Having Random Parameters," APL/JHU CLM-116, 28 April 1965.
3. A. G. Carlton, "Adaptive Prediction with Random Observational Errors," APL/JHU CLM-118, 20 May 1965.
4. L. M. Spetner, "Further Considerations on the Optimum Prediction of a Noise Process Having Random Parameters," APL/JHU CLM-120, 18 June 1965.

Section IV
HIGH TEMPERATURE RESEARCH

Hypersonic Gas Dynamics--Collection of experimental data on which to base a better understanding of the fluid-dynamic processes in rocket nozzles was continued. In these studies, a small-scale solid-propellant rocket motor is used to simulate conditions encountered in full-scale firings. Surface temperatures and temperature profiles made throughout 25° and 12-1/2° molybdenum insert nozzles in gas flows generated by a 2500°K nonaluminized propellant show that the nozzle flow is definitely turbulent and that the computed heat transfer coefficients agree reasonably well with those predicted. Analysis of spectrometer emission and absorption data as a means of accurately determining the static temperature of propellant gases should prove satisfactory (IV/1).

HIGH TEMPERATURE RESEARCH IV/1
Hypersonic Gas Dynamics R11BFM
Support: ARPA
W. P. Dickens, H. J. Unger, and F. K. Hill
April - June 1965

ROCKET NOZZLE FLUID DYNAMICS

High-temperature gas generated by the burning of a solid propellant forms a simple fluid system as it passes through a nozzle into supersonic flow. The primary objective of this study has been the experimental investigation of such a system with the principal efforts focused on the study of local heat-transfer rates in the rocket nozzle and the chemical reaction rates and specie concentrations of the reacting gases. These experimental data are essential to developing a better understanding of the fluid dynamic processes involved in such fluid systems: a knowledge of the mechanics and chemistry of nonequilibrium gas flows, the effects of gaseous and nongaseous states of propellant flows on rocket nozzle systems, and the collection of data vital to accurate predictions of nozzle heat flux rates.

SUMMARY AND CONCLUSIONS

Surface temperatures and temperature profiles have been made throughout 25° and 12½° molybdenum insert nozzles in gas flows generated by a 2500°K ARP propellant. The data show that the nozzle flow is definitely turbulent and, except in the immediate region of the throat where a region of flow separation is believed to exist, the computed heat transfer coefficients agree reasonably well with those predicted by the empirical equation of Bartz (Ref. 1) for turbulent heat transfer in a nozzle.

The analysis of spectrometer emission and absorption data as a means of accurately determining the static temperature of propellant gases indicates that this method should prove quite satisfactory once the emissivity of the source can be better determined.

FUTURE PLANS

Further analysis of the 12½° and 25° nozzle heat transfer data will be made, and a closer examination will be given to the nozzle throat region where flow separation possibly exists. Future plans will include an attempt to measure surface temperatures in the DGV nozzle and a comparison of the heat transfer data obtained with that from ARP propellants. Additional applications of the scanning spectrometer for use with both propellants are being studied.

BACKGROUND

Two ABL manufactured propellants have been used in the rocket tunnel to generate the gas flows under investigation--an ARP propellant burning at 2500°K at pressures of 1100 to 1200 psia and a DGV (aluminized) propellant providing a supply pressure of 1300 to 1400 psia at a combustion temperature of 3770°K. Special experimental techniques and instrumentation have been developed to overcome the severe environmental conditions of these gas streams, and nozzle boundary-layer surveys (temperature and pressure), nozzle-throat heat-transfer measurements, and spectrographic studies of the emission and absorption of the gas flow throughout the nozzle have been reported (Refs. 2,3,4, and 5).

The investigation of heating rates in the rocket nozzle was begun in the test section where the usual boundary layer probe techniques could be employed. In the vicinity of the nozzle throat, however, these methods were unsatisfactory as a result of the high temperatures and thin boundary layer, and the technique of directly monitoring nozzle surface temperatures by means of transistorized optical pyrometers was developed (Refs. 6 and 7). More recently these pyrometers have been replaced by smaller more adaptable silicon photodiode pyrometers.

Extensive measurements of surface and insert temperatures at the throats of 25° solid molybdenum and molybdenum insert nozzles have been made and heating rates determined (Ref. 3). Similar investigations throughout the entire throat region were begun with both 12½° as well as 25° nozzles and adaptations of the instrumentation for use with DGV propellants is being studied (Ref. 4).

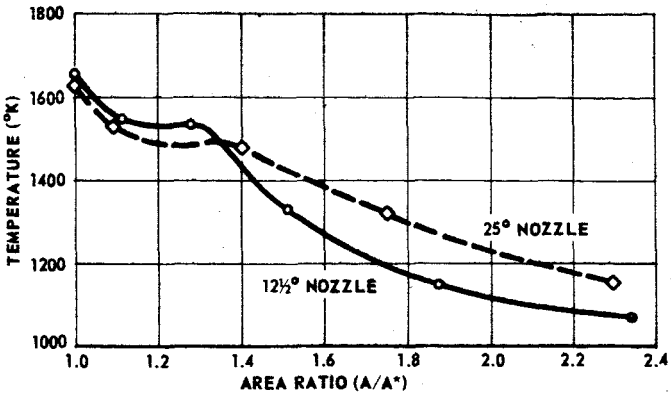

Fig. 1 Surface Temperatures in 25° and 12-1/2° Nozzles. (76510)

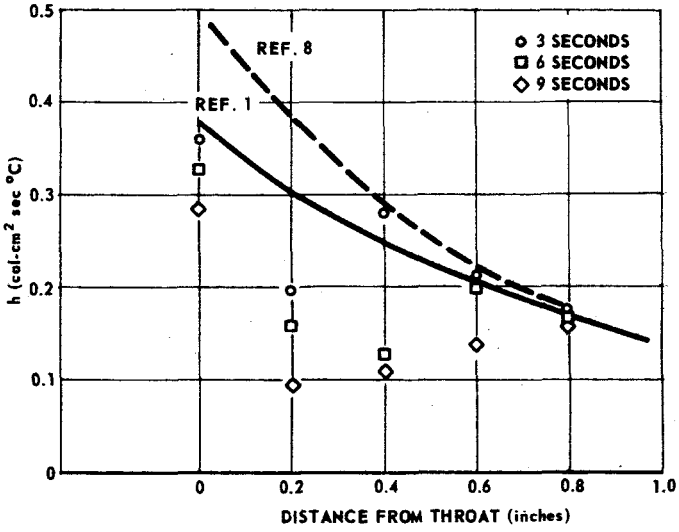

Fig. 2 Heat-Transfer Coefficient versus Distance from the Throat of a 25° Molybdenum Insert Nozzle. (76511)

DISCUSSION

Surface temperature data obtained by means of miniature optical pyrometers are shown in Fig. 1 as a function of area ratio. The data are from both 12½° and 25° molybdenum insert ARP nozzles having throat diameters from 0.628 to 0.630 inch. In addition to surface measurements, temperatures throughout the nozzle inserts have been surveyed by means of both thermocouples and pyrometers. By extensively surveying at a given cross section (0.2 to 0.025 inch from the nozzle surface) accurate determinations of temperature gradients were obtained. In Fig. 2, the heat transfer coefficient at various stations in the 25° nozzle, calculated from a one-dimensional heat transfer assumption, is shown. While heating rates as high as 20 to 30 Btu/in^2/sec are obtained just after ignition (Ref. 3), comparison with various empirical turbulent heat transfer relationships (Refs. 1 and 8) shows rather good agreement after 3 seconds. The drop in heat transfer and surface temperature observed just downstream of the nozzle throat is possibly a result of a region of flow separation thought to exist throughout the throat of the 25° nozzle. Further analysis of this possibility as well as completion of the 12½° nozzle analysis is under way.

From the spectra obtained in the gas composition measurements with the scanning spectrometer (Ref. 5), it was possible to make calculations of the gas temperature at various nozzle stations. By a comparison of the emission and absorption intensities at a given wavelength and the intensity of a source of known emissivity, gas temperatures may be determined. The results for both the 12½° and 25° nozzles are compared in Table I with values obtained from a kinetic calculation for the ARP propellant (Ref. 9). The static temperatures, computed from the absorption and emission data, tend to be slightly higher than those from the kinetic calculation. This apparently results from the fact that it was necessary to compute the emissivity of the source from measured emission data of the gas at the 0.8-inch-diameter station, assuming that the kinetic calculation for this station was accurate. This was necessary since the Nernst glower source has a broad emission band at 5.2μ and a direct determination of its emissivity has not yet been possible. While there are several spectroscopic methods of determining the temperature of a gas in thermal equilibrium, all are difficult, indirect, and, in general, unsatisfactory at higher temperatures. It would appear that this method of determining gas temperatures should be reasonably accurate once a more exact determination of the source emissivity can be made.

REFERENCES

1. D. R. Bartz, "A Simple Equation for Rapid Estimation of Rocket Nozzle Heat Transfer Coefficients," Jet Propulsion, Vol. 27, 1957.
2. Polaris Long Range Research Quarterly Review (Confidential), APL/JHU TG 412C-4, July 1962.
3. Polaris Long Range Research Quarterly Review (Confidential), APL/JHU TG 412C-6, January 1963.
4. F. K. Hill, H. J. Unger and W. P. Dickens, "Rocket Nozzle Fluid Dynamics," Section IV-1, Aeronautics Division Quarterly Review (Confidential), APL/JHU AQR/64-4, October-December 1964.
5. H. J. Unger and F. K. Hill, "Spectroscopic Measurements of Combustion Gas Composition in Supersonic Flow," AIAA Propulsion Joint Specialist Conference, June 1965.
6. Polaris Long Range Research Quarterly Review (Confidential), APL/JHU TG 412C-5, October 1962.
7. S. A. Elder, "A Completely Transistorized Pyrometer," Temperature - Its Measurement and Control in Science and Industry, Vol. III, Part 2, Reinhold, 1962.
8. D. A. Saunders and P. H. Calder, "Heat Transfer in a Nozzle at Supersonic Speeds," Engineering, V. 1. 174, 1952.
9. A. A. Westenberg and S. Favin, Ninth International Symposium on Combustion, Academic Press, New York, 1963.

Table I

Calculation of Static Temperatures from CO_2 Absorption and Emission Measurements

Nozzle Diameter (inches)	Emission (percent)	Absorption (percent)	Static Temperature (from emission and absorption measurements)	Static Temperature (kinetic calculation)
		12½° Total Angle Nozzle		
0.80	135.7	99.0	1745	1745
1.06	101.5	98.2	1549	1442
1.35	71.8	97.9	1356	1257
1.86	39.0	92.2	1124	1012
2.33	23.4	79.5	1008	920
		25° Total Angle Nozzle		
0.80	205.0	96.6	1738	1738
1.08	119.3	95.2	1402	1417
1.33	98.6	94.5	1310	1245
1.86	47.6	92.5	1041	1026
2.33	29.9	80.6	949	874

Section V
FUNDAMENTAL RESEARCH

Microwave Physics--It has been found that the repulsive short-range exchange forces are solely responsible for the shift in magnetic field in the "diatomic molecule" formed by two colliding Xe atoms (V/1a). As a result of applying the lattice sum method to evaluation of the magnetic dipolar energy of antiferromagnets, the values of the dipolar anisotropy energy and of the five-structure energy have been substantially revised (V/1b). Spectrometric measurements are being made on transition-metal ion-pairs coupled by exchange interactions in an effort to obtain electron spin resonance data which will supplement optical data in this field (V/1c). Electron spin resonance techniques are also being used to study photoexcited organic molecular solids (V/1d).

Plasma Dynamics Research--A theta-pinch gun is being developed to produce dense, hot plasmas. Improvements were made in the gun this quarter, but its shot-to-shot reproducibility is not yet satisfactory (V/2).

Hypersonic Gun Tunnel--The hypersonic gun tunnel provides uncontaminated air flows suitable for testing hypersonic ramjet inlet models. It can also be used as a research tool for investigation of fundamental flow problems, boundary-layer interaction, flow near the leading edge of blunt bodies, and configuration problems at high Mach numbers. The majority of tests conducted during the quarter were preliminary studies of the flow about different configurations to develop future testing techniques (V/3).

FUNDAMENTAL RESEARCH V/1a
Microwave Physics X81RMP
Support: Task X/NOw-62-0604-c
F. J. Adrian
July 1964 - June 1965

INTERPRETATION OF NUCLEAR MAGNETIC RESONANCE IN INERT GASES

Nuclear magnetic resonance studies of the inert gas xenon have yielded some interesting results which depend on the interaction of colliding atoms. For one thing, the magnetic field at a xenon nucleus, which is slightly different from the applied field because of the interaction of the electrons of the atoms with the applied field, increases linearly with the density of the gas (Refs. 1 and 2). Secondly, the nuclear spin relaxation processes, whereby a nucleus dissipates its magnetic energy into kinetic energy, increase in efficiency linearly with the density of the gas (Refs. 2 and 3), indicating that the nuclear spin relaxation occurs only during interatomic collisions. The purpose of this study was (a) to show that the interaction between colliding atoms could account for the observed results and (b) to determine the relative contribution of the attractive Van der Waals interactions and the repulsive exchange interactions to these effects.

SUMMARY AND CONCLUSIONS

The shift in magnetic field was computed for a "diatomic molecule" formed by two colliding Xe atoms. It was found that the repulsive short-range exchange forces were solely responsible for this effect. When an average was taken over all types of collisions, the following value was obtained for the magnetic field shift (Ref. 4): $\Delta H = 2.85(10)^{-7}\ H\rho$, where H is the applied field and ρ is the density in amagats. This was in order-of-magnitude agreement with the observed result (Refs. 1 and 2): $\Delta H = 4.3(10)^{-7}\ H\rho$. This result also gave a final accounting of the problem of nuclear spin relaxation in Xe^{129}. This is because Torrey (Ref. 5) had previously shown that any mechanism which could account for the observed magnetic field shift in terms of pairs of colliding Xe atoms would also produce a magnetic coupling between the nuclear spins and the rotational angular momentum of the colliding pair which would be large enough to account for the observed nuclear spin relaxation of this isotope.

For the isotope Xe^{131}, whose nucleus has an electric quadrupole moment, a much more effective relaxation mechanism is the interaction of the electric quadrupole moment with the collision-deformed electronic charge cloud of the atom. Again a pair of colliding Xe atoms were treated as a rotating "diatomic molecule" whose nuclear electric quadrupole interaction permitted the nuclei to relax by exchanging energy with the rotational angular momenta of the colliding atoms. The calculation showed that the contributions of the exchange and Van der Waals interactions to the nuclear quadrupole coupling constant were of opposite sign, and that the exchange contribution was six times larger than the Van der Waals contribution at a typical collision distance of 4Å. An average of the single collision transition probabilities over all types of collisions gave the following result for the relaxation time (Ref. 6): $T_1 = 22/\rho$ sec. This is in good agreement with the experimental value (Ref. 3): $T_1 = 26/\rho$ sec.

FUTURE PLANS

It is hoped that these results will aid in the interpretation of current experiments on the liquid and solid phases of xenon in terms of the detailed structure of these phases. How much of this work will be done at the Applied Physics Laboratory, however, will depend on the extent of the theoretical work done by the groups at Washington and Rutgers Universities who are conducting the experiments.

BACKGROUND

Nuclear magnetic resonance is based on the fact that all nuclei of nonzero spin have a magnetic moment. In an external magnetic field, such nuclei have two or more quantized orientations with correspondingly different magnetic energies. The transition energy between two nuclear magnetic energy levels for magnetic fields in the kiloersted range lie in the radio-frequency region of the spectrum. Such nuclear spin transitions may be stimulated and detected by placing the sample in the tank coil of an oscillator operating at the resonant frequency.

One interesting feature of these experiments is that, because of the interaction of the external field with the electrons of the system, the magnetic field at the nucleus is invariably slightly different from the applied field. For an isolated spherical atom, the effect of the applied field is to induce a Larmor precession of the electrons which produces a small field at the nucleus of opposite sign to the applied field (diamagnetic shift). This effect is of little importance, however, because it is virtually independent of the state of aggregation of the atom. When an atom forms a molecule, collides with another atom, or otherwise has its spherical symmetry disturbed, the magnetic field may also admix virtual excited states into the ground-state wave function of the system. These excitations lead to electronic currents which produce a small additional magnetic field at the nucleus which usually has the same sign as the applied field (paramagnetic shift). The paramagnetic shifts are of great interest because they depend critically on the outermost or

valence electrons of the atoms, and, thus, are a tool for investigating the charge distribution in those electronic orbitals which determine chemical binding, interatomic forces, etc. Although a pair of colliding Xe atoms do not form a chemical bond, the overlap of their orbitals during a collision provides a path for the flow of a magnetic-field induced current between the atoms. This current produces the relatively large pressure-dependent paramagnetic shift observed in this gas.

Nuclear-spin relaxation is an integral part of nuclear magnetic resonance, because, as a nucleus absorbs energy from a radio-frequency oscillator it must dissipate this energy into other energy modes (translation, rotation, vibration, etc.) of the system. If it cannot do this, the resonant nuclear magnetic energy levels quickly become equally populated and absorption of radio-frequency energy stops before a detectable amount of energy can be absorbed. Since the energy of the nuclear transitions is very small compared to energies of translation, rotation, etc., these motions act as a constant temperature bath into which the nuclear spin system may dissipate any excess energy and remain in thermal equilibrium. However, the coupling between the nuclear spin system and the other energy modes is often quite weak so that the time required for a saturated nuclear spin system to regain thermal equilibrium (relaxation time) is often quite long. This difficulty is especially acute in xenon gas because conservation of angular momentum requires that a change in nuclear spin orientation be balanced out by a change in the angular momentum of some other motion of the system. Since an isolated spherical Xe atom has no other angular momenta, the nuclear spin transitions which lead to relaxation can occur only during collisions.

REFERENCES

1. R. L. Streever and H. Y. Carr, "Nuclear Magnetic Resonance of Xe^{129} in Natural Xenon," Phys. Rev., Vol. 121, No. 1, 1961, pp. 20-25.
2. E. R. Hunt and H. Y. Carr, "Nuclear Magnetic Resonance of Xe^{129}," Phys. Rev., Vol. 130, No. 6, 1963, pp. 2302-2305.
3. D. Brinkmann, E. Brun, and H. H. Staub, "Kernresonanz im Gasformigen Xenon," Helv. Phys. Acta, Vol. 35, 1962, pp. 431-436.
4. F. J. Adrian, "Theory of the Nuclear Magnetic Resonance Chemical Shift of Xe in Xenon Gas," Phys. Rev., Vol. 136, No. 4A, 1964, pp. A980-A987.
5. H. C. Torrey, "Chemical Shift and Relaxation of Xe^{129} in Xenon Gas," Phys. Rev., Vol. 130, No. 6, 1963, pp. 2306-2312.
6. F. J. Adrian, "Quadrupolar Relaxation of Xe^{131} in Xenon Gas," Phys. Rev., Vol. 138, No. 2A, 1965, pp. A403-A409.

FUNDAMENTAL RESEARCH V/Ib
Microwave Physics X81RMP
Support: Task X/NOw-62-0604-c
J. C. Murphy, J. O. Artman, and S. Foner
July - December 1964

MAGNETIC DIPOLAR FIELDS IN ANTIFERROMAGNETS

In a previous study on the spectral properties of ruby, the electric potential at a lattice point was evaluated by summing up the potentials caused by all other lattice ions. This lattice sum method has been extended and applied to the evaluation of the magnetic dipolar fields in some antiferromagnetic substances. Such an approach yields directly the knowledge of the magnetic dipolar energy which is an important part of the total magnetic anisotropy energy of an antiferromagnet. If the total magnetic energy is already known from some other source, then the difference between the total and the dipolar field energies can be interpreted as the fine-structure energy, which is a physically significant quantity but is at present neither directly measurable by experiment nor readily amenable to theoretical calculations.

BACKGROUND

Consider a transition-metal ion oxide such as Cr_2O_3 or α-Fe_2O_3. It is isomorphous in crystal structure as corundum (α-Al_2O_3). Each oxide crystal is composed of two coupled antiparallel magnetic systems or sublattices, having the unpaired electron spins directed along the hexagonal or c-axis. The net magnetization for the whole crystal is very nearly zero below a certain critical temperature – the essential feature of an antiferromagnet. But because of the difference in the patterns of spin orientations in the crystal, the magnetic structure of Cr_2O_3 is distinctly different from that of α-Fe_2O_3.

For a given set of crystalline lattice and metal ion parameters and a specific magnetic structure known for a certain antiferromagnet, the magnetic dipole field (H_Z or D_Z) and the dipolar anisotropy energy (K_{MD}) can be computed by the following expressions:

$$\frac{H_Z}{n} = D_Z = \mu_B \sum_i P_i (3\cos^2\theta_i - 1)/R_i^3$$

$$K_{MD} = \frac{3}{4} n^2 \mu_B D_Z$$

where H_Z is the magnetic dipole field along the z-axis (parallel to the c-axis), n is the number of μ_B (Bohr magneton) per dipole, D_Z is the dipolar field per n, P_i specifies the orientation of the i^{th} dipole (+ or -), and R_i and θ_i define the i^{th} dipole location with respect to

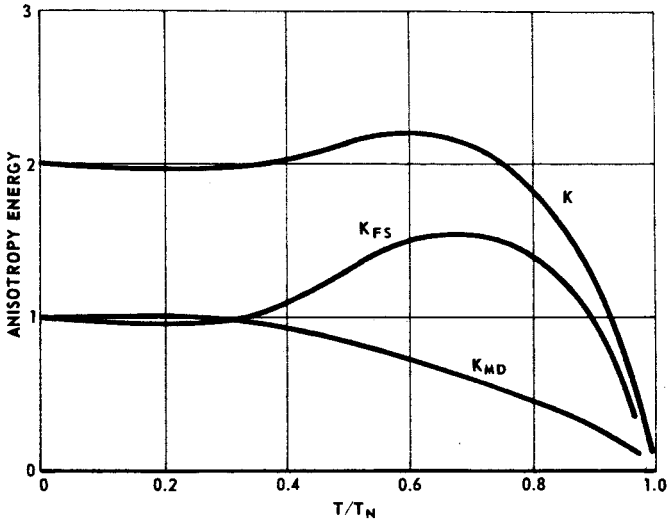

Fig. 1 Anisotropy Energy (in Units of 10^5 erg/cm^3) versus Reduced Temperature T/T_N for Cr_2O_3. (76543)

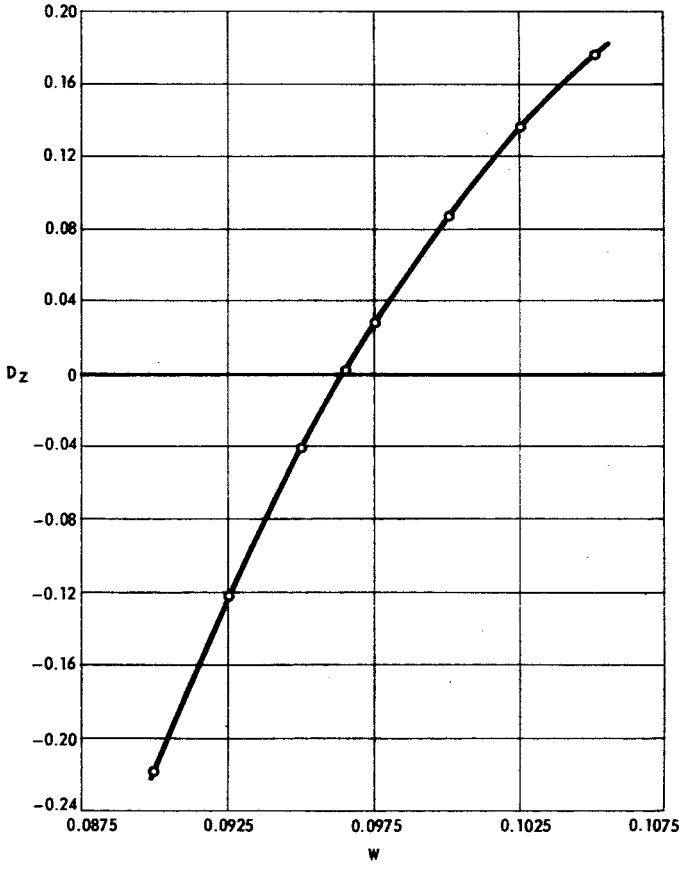

Fig. 2 D_Z in Units of Kilogauss/(Number of μ_B per Dipole) versus W for Cr_2O_3. $A_o = 4.9607$ Å, $C_o = 13.599$ Å, W(presently accepted) = 0.0975. (76544)

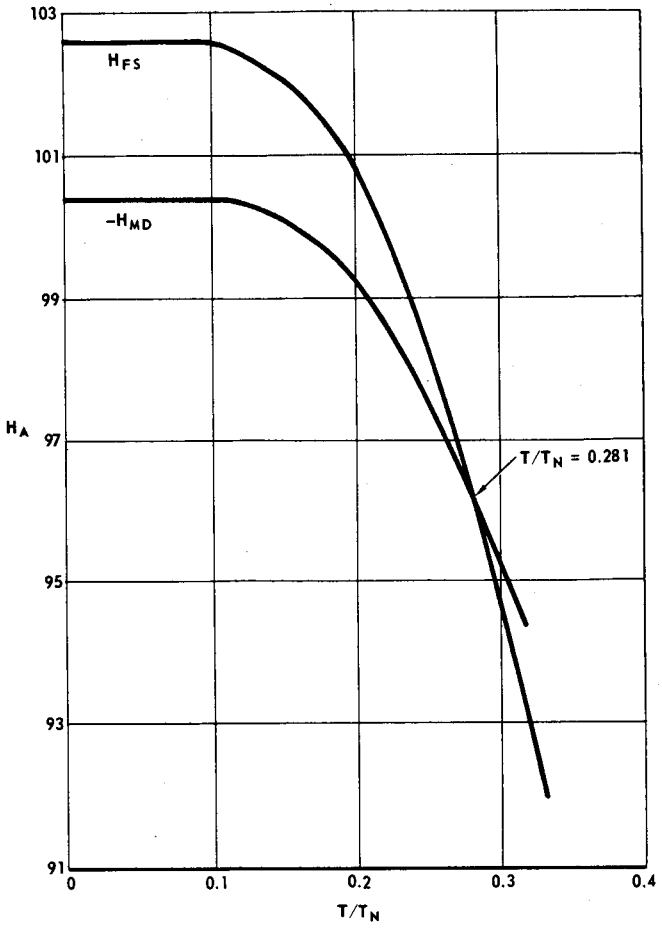

Fig. 3 Plot of the Temperature Variation of the Effective Magnetic Fields Due to Magnetic Dipolar Energy (H_{MD}) and Fine Structure Energy (H_{FS}). Units of 10^2 Gauss Are Used. $H_A = H_{MD} + H_{FS}$. $H_A = 0$ at $T/T_N = 0.281$. (76545)

the reference site. In computing for the lattice sum of D_Z, the machine computation programs (Ref. 1) developed previously for the lattice sum of the electric potential were used to considerable advantage, thus insuring appropriate averaging and satisfactory convergence.

The results for the computation of K_{MD} can be profitably used for the interpretation of the total magnetic anisotropic energy, K, in terms of its components by the relation $K = K_{MD} + K_{FS}$, where K_{FS} denotes the fine-structure energy which is a result of spin-orbital coupling and crystalline environment. The quantity K can be measured in an antiferromagnetic resonance experiment which is usually done at very high magnetic fields and millimeter or submillimeter frequencies. Under these conditions, K_{FS} can be expressed as $K - K_{MD}$, which is the difference between the experimentally obtained anisotropy and the theoretically calculated magnetic dipolar energy. Figure 1 shows the results of K_{FS} for Cr_2O_3, as a function of temperature, when deduced from the information on K and K_{MD}.

SUMMARY AND CONCLUSIONS

Two rather significant results (Refs. 2 and 3) were obtained from the calculation of K_{MD} and the corresponding interpretation of $K_{FS} = K - K_{MD}$ for the following two cases:

1. Cr_2O_3. The magnetic structure, in the geometric sense, of this antiferromagnet is almost cubic. As a consequence, the results for the computation of D_Z show a very high sensitivity with respect to W, which is a special position parameter for the metal ion, as shown in Fig. 2. Thus, $K_{MD} = 0.0088$ cm^{-1}/ion for the presently accepted value of $W = 0.0975$, whereas $K_{MD} = 0.059$ (which is six times higher than the present value) for a previously assumed value of $W = 0.105$. This drastic revision in the calculated value of K_{MD} means a correspondingly large revision of the deduced value for K_{FS}. Recent experimental results of Rubenstein and Krebs (Ref. 4) on their Cr^{53} nuclear magnetic resonance work appear to support the present conclusions.
2. α-Fe_2O_3. In this case the calculated value for K_{MD} and the deduced value for K_{FS} are, at low temperatures, almost equal in magnitude but opposite in sign. Moreover, the variations of K_{MD} and K_{FS} with temperature T (or T/T_N, where T_N is the Neel temperature) are expected to be different because of their different functional dependences. The computed results actually show there is a definite temperature across which the quantity K would change sign, corresponding physically to the flip over of the spins. This situation is shown in Fig. 3 which gives the value $(T/T_N)_{flip} = 0.281$ in rather good agreement with that of 0.274 as concluded by other types of investigations.

FUTURE PLANS

This work is considered to be completed.

REFERENCES

1. J. O. Artman and J. C. Murphy, "Lattice Sum Evaluations of Ruby Spectral Parameters," Phys. Rev., Vol. 135, No. 6A, 1964, pp. 1622-1639.
2. J. O. Artman, J. C. Murphy, and S. Foner, "Magnetic Anisotropy in Antiferromagnetic Corundum-Type Sesquioxides," Phys. Rev., Vol. 138, No. 3A, 1965, pp. 912-917.
3. J. O. Artman, J. C. Murphy, and S. Foner, "Magnetic Anisotropy in Antiferromagnetic α-$(Cr_{1-f}Al_f)_2O_3$," J. Appl. Phys., Vol. 36, No. 3, Part 2, 1965, pp. 986-987.
4. M. Rubenstein and J. Krebs, "Magnetic Dipolar Fields in Antiferromagnets," Physics Letters, Vol. 12, 1964, p. 302.

FUNDAMENTAL RESEARCH V/1c
Microwave Physics X81RMP
Support: Task X/NOw-62-0604-c
J. C. Murphy and J. Bohandy
July 1964 - June 1965

ELECTRON SPIN RESONANCE IN TRANSITION-METAL ION-PAIRS COUPLED BY EXCHANGE INTERACTIONS

Considerable work has been done in recent years on the study of the microwave and optical properties of isolated transition-metal ions in a nonmagnetic host crystal, especially in the case of Cr^{3+} ions in α-Al_2O_3(ruby). In contrast, there has been relatively little work done in the case where the paramagnetic ions couple together in the form of ion-pairs through the exchange interactions between them. The importance of the latter study has been widely recognized (Ref. 1) and there is an increasing amount of work (Refs. 2 and 3), mostly optical, which has appeared in the field. In the present study, an attempt has been made to observe experimentally the pair phenomena by the technique of electron spin resonance. It is hoped that by using this technique some new information about the ion-pairs can be obtained which ordinarily would not be readily accessible to optical investigations.

SUMMARY AND CONCLUSIONS

Consider first an isolated transition-metal ion (like Cr^{3+}) in a crystal (like α-Al_2O_3). The influence of the crystal field at the site of the ion can be described under such conditions by a fine-structure energy written as $\mathcal{H}_{FS} = DS_Z^2$, where D is a constant depending upon the spin-orbital characteristics of the ion and the nature of the crystalline environment, and S_Z is the Z-component (along the c-axis) of the electron spin angular momentum. Next, suppose the concentration of the transition-metal ions is increased from the range of 0.01 percent by 10- to 100-fold. As may be seen in Fig. 1, there is a fair probability that some of the adjacent sites will be occupied by these ions. We can thus have pairs of ions labeled by their site positions as ab, ac, bc, ad, etc. The two ions in each pair are bound together by

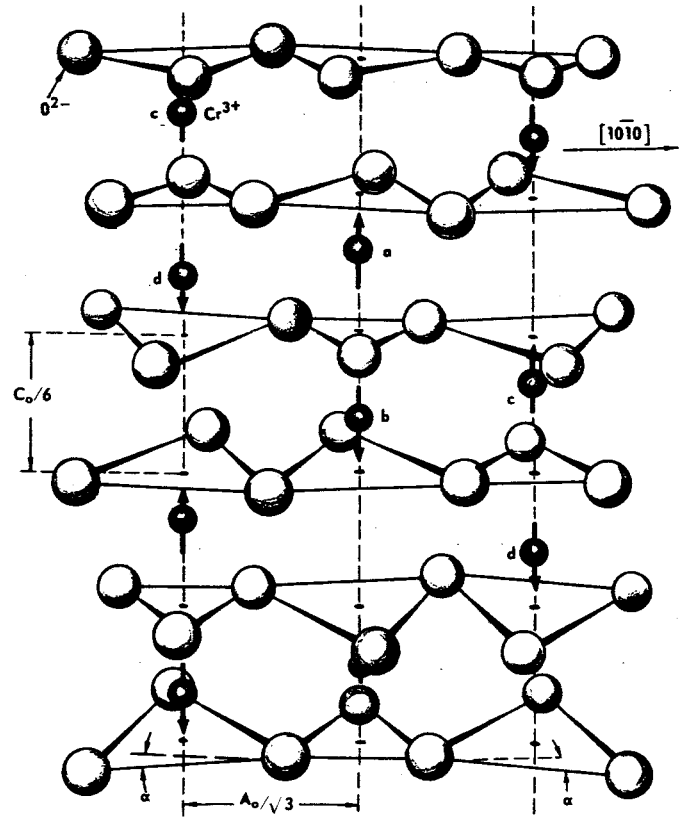

Fig. 1 α - Al_2O_3 Crystalline Lattice Structure, with A_o and C_o as Lattice Parameters. Sites Occupied by Metal Ions Are Denoted by a, b, c, d. They Are Ordinarily Occupied by Al^{3+} Ions but Can Be Occupied by Cr^{3+} Ions by Substitution. Arrows Indicated on These Ions Denote Spin Orientations (all along the Hexagonal Axis which Is the c-axis) for a Cr_2O_3 Crystal Corresponding to 100 Percent Substitution. (76546)

an "exchange" interaction energy which may be written as $-J\,\vec{S}_1\cdot\vec{S}_2$ where J is the exchange energy coefficient (known as the "exchange integral") and $\vec{S}_1$ and $\vec{S}_2$ represent the angular momenta of the individual ions. The net effect of this exchange coupling is that the ion-pair appears to behave as a unit with the total angular momentum $\vec{S} = \vec{S}_1 + \vec{S}_2$. There is also a fine-structure energy $\mathcal{H}_{FS} = D(S_{1Z}^2 + S_{2Z}^2) = D(S_Z^2 - 2S_{1Z}S_{2Z})$ and a magnetic energy $\mathcal{H}_H = g\mu_B\vec{S}\cdot\vec{H}$ (g = g-factor, μ_B = Bohr magneton) when an external magnetic field ($\vec{H}$) is applied to the crystal. Thus, we have the expression for the total Hamiltonian of the ion-pair as follows:

$$\mathcal{H} = -J\vec{S}_1\cdot\vec{S}_2 + D(S_{1Z}^2 + S_{2Z}^2) + g\mu_B(\vec{S}_1 + \vec{S}_2)\cdot\vec{H}$$

with $\vec{S} = \vec{S}_1 + \vec{S}_2$.

The solution of the aforementioned Hamiltonian would give values to the various energy levels for the ion-pair. If we assume $|J| \gg |D|$, as it is true for many cases of interest, then the energy scheme is largely determined by the 2S + 1 levels with intervals defined in terms of |J|. There is also a fine structure to each S-level which is determined by the splitting caused by spin-orbital and crystalline field effects. In addition, the presence of an external magnetic field will cause a complete removal of all remaining degeneracies in energy and make all levels vary their energy values in certain ways.

The "spin" energies of the kind described above are present in each electronic level for the ion-pair. The transitions between different electronic levels are generally in the optical range with spectral line structures determined by the differences in the fine-structure energy levels. If, however, we consider only the ground electronic energy state, then the transitions in each S level may generally be in the microwave range (the transitions between different S-levels are usually forbidden and their frequencies, if present, are often in the infrared range).

It is also interesting to consider the effect of an external electric field (in addition to the magnetic field) on the microwave transitions between states of exchange interaction coupled Cr^{3+} pairs in Al_2O_3. This system is quite appropriate for such studies since it is one of the few cases in which exchange coupled pairs have been studied by microwave spectroscopy and a crystalline pseudo-Stark splitting for isolated Cr^{3+} ions has been detected. It is expected in analogy with the case of isolated Cr^{3+} ions in Al_2O_3 that the application of an electric field to the crystal will change slightly the value of D and hence perturb the spectral location of the observed microwave transition.

SUMMARY OF TEST RESULTS

A set of experiments was conducted at 9.4 Gc on concentrated samples (~ 0.875% Cr) of ruby in which a weak, complicated spectrum attributable to exchange-coupled pairs of Cr^{3+} ions was observed. Upon application of an external electric field, changes in intensity and relative position of some lines of this spectrum were observed. Quantitative measurements were not feasible because of the poor resolution of these lines at this frequency and this concentration. Since the resolution is expected to improve as the frequency of the microwave spectrometer is increased and the concentration of Cr^{3+} is reduced, a new spectrometer was constructed from available components at 16 Gc using 0.2 percent Cr^{3+} samples. The pair spectrum was again observed this time with increased resolution as expected. The general experimental situation relative to spectrometer stability, however, worsens when the electrodes needed for external electric field studies are applied to the sample. To date no unambiguous dependence on external electric field has been observed at 16 Gc. The reasons for this are under investigation.

FUTURE PLANS

In addition to investigating for still better means of resolution and ion-pair spectral identification, other materials for the pair experiment are being investigated to determine if some of them will exhibit a smaller number of lines caused by nonequivalent pairs. This would simplify both the resolution and the line identification problem.

REFERENCES

1. J. S. Smart, "Evaluation of Exchange Interactions from Experimental Data," Ch. 2 of Magnetism edited by George T. Rado and H. Suhl, Vol. III, 1963, pp. 63-114.
2. A. L. Schawlow, D. L. Wood, and A. M. Clogston, "Electronic Spectra of Exchange-Coupled Ion Pairs in Crystals," Phys. Rev. Letters, Vol. 3, No. 6, 1959, pp. 271-272.
3. P. Kisliuk and W. F. Krupke, Exchange Interaction between Pairs of Chromium Ions in Ruby, Report No. TDR-169 (3250-24) TN-2 of Aerospace Corporation, November 1963.

FUNDAMENTAL RESEARCH V/1d
Microwave Physics X81RMP
Support: Task X/NOw-62-0604-c
L. C. Aamodt, A. H. Piksis, and C. K. Jen
July 1964 - June 1965

ELECTRON SPIN RESONANCE IN PHOTOEXCITED ORGANIC MOLECULAR SOLIDS

The excited states of most atomic and molecular systems have lifetimes that are too short to allow these states to be studied by electron-spin resonance techniques. There are certain complex organic molecules, such as naphthalene, however, for which this is not the case. These molecules have been found to have rather long lifetimes – of the order of a second in their triplet states. It is possible, through optical pumping, to populate this energy level sufficiently to allow observation of transitions between its Zeeman components. Investigation of the excited states of these molecules by electron-spin resonance techniques (Ref. 1) provides considerable information that cannot be obtained through optical means; it also provides another point of view for understanding the excited state of matter.

DESCRIPTION OF WORK

Conditions for Observation--When the excited triplet state has a zero-magnetic-field splitting, as it does in naphthalene, large anisotropies result in its resonances at higher magnetic fields. These anisotropies broaden the spectral lines sufficiently so that it is impossible to observe a spectrum if the sample is composed of randomly arranged molecules. The molecules must be arranged in ordered orientations. The needed molecular order can be obtained by putting the molecule into a host crystal having a crystal structure compatible with the inclusion of the guest molecule. Since the lifetime of the triplet state is temperature dependent, it is necessary to perform experiments at reduced temperature. Figure 1 shows an experimental arrangement designed to work at liquid nitrogen temperature. The sample is placed in a microwave cavity which is attached to the lower end of a liquid nitrogen reservoir. The incident and reflected microwave radiation are separated by the microwave circulator mounted above the dewar, and are brought into, and out of, the cavity through the vertical waveguide passing upward from the cavity through the liquid nitrogen chamber. This arrangement frees the region below the cavity for the placement of optical apparatus. An AH-6 high-pressure mercury arc lamp is used to illuminate the sample. The ultraviolet radiation is focused on the sample, and the whole assembly is placed in a DC magnetic field as shown in Fig. 1.

Energy Levels and Magnetic Resonance Transitions--A typical energy level diagram for these molecules is shown in Fig. 2 (Ref. 2). This particular diagram is for naphthalene. Radiation from the ultraviolet light

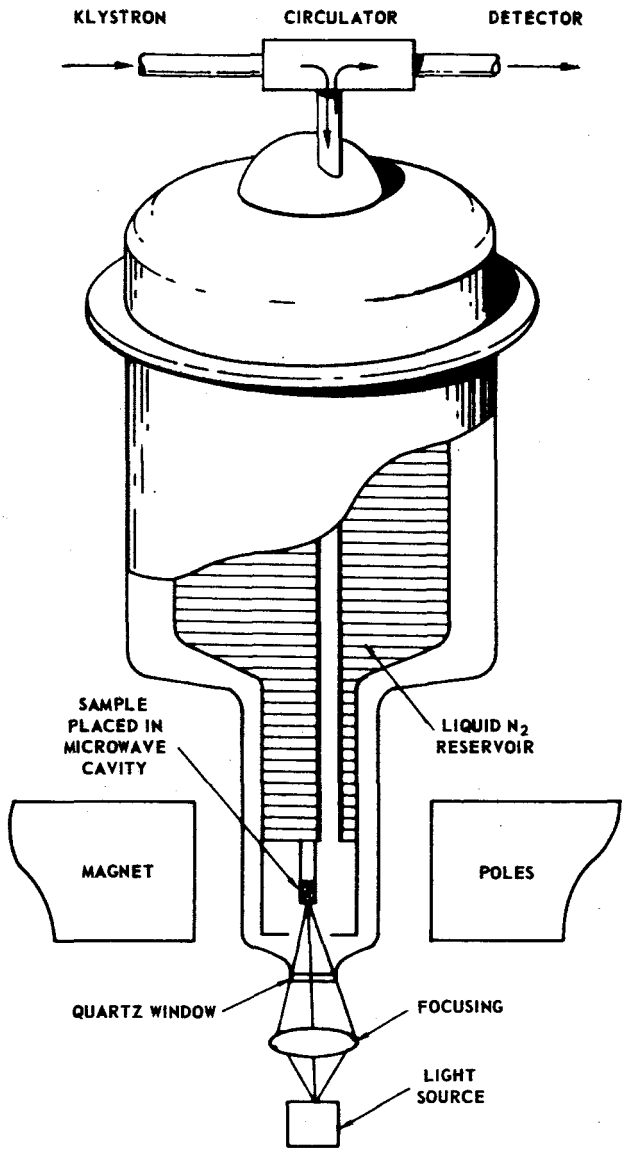

Fig. 1 An Experimental Arrangement in which the Sample Is Contained in a Microwave Cavity, Cooled at Liquid Nitrogen Temperature, Placed in a Magnetic Field, and Irradiated by an Ultraviolet Light Source. (76547)

source raises the molecule from the ground state to the $^1B_{2u}$ and $^1B_{3u}$ excited singlet states. Then, through interactions within the crystal, nonradiative transitions cause the molecule to drop to its lowest excited state, the triplet state $^3B_{2u}$. The dashed line in Fig. 2 indicates the "forbidden" transition that produces the phosphorescent emission characteristic of this molecule. The metastable nature of the triplet state allows the electrons to remain long enough to allow transitions between the Zeeman components of the triplet energy level. These Zeeman energy

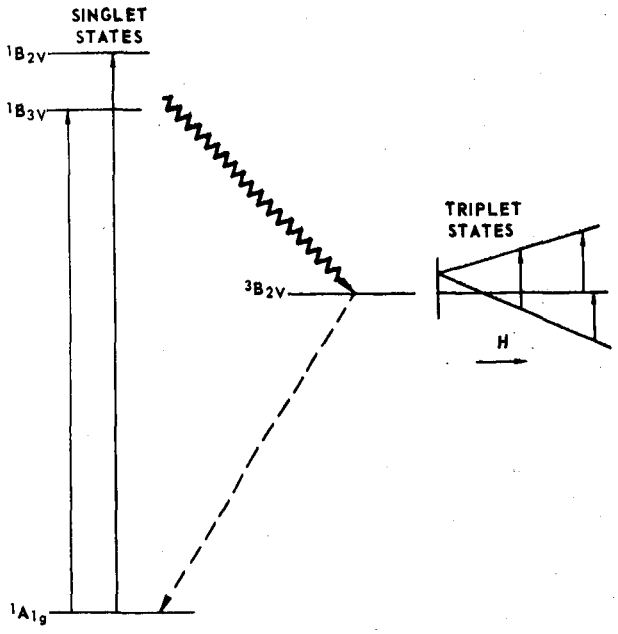

Fig. 2 Energy Levels of the Low-Lying Singlet and Triplet States of Naphthalene Showing Schematically the Zeeman Splitting of the Triplet State for One Particular Molecular Orientation with Respect to the Magnetic Field. (76548)

levels are shown schematically in Fig. 2 for one particular molecular orientation. In actuality, these energy levels are complicated functions of sample orientation relative to the magnetic field because of the presence of the anisotropy energies usually described by the coefficients D and E. This anisotropy causes a mixing of the spin states allowing $\Delta m = 2$ transitions as well as the usual $\Delta m = 1$ transitions. In general, for every relative orientation of the molecule in the magnetic field, three lines can be observed, each at a different magnetic field intensity (as shown in Fig. 2). At one particular sample orientation, however, two of these lines coincide. Under these conditions, a double quantum transition is possible, with the electron being elevated directly from the lowest to the highest Zeeman level, and with the simultaneous absorption of two microwave quanta.

From the anisotropic features of the paramagnetic spectrum, the magnitudes of D and E (and their relative signs) can be determined, and the components of the g tensor can be evaluated. In addition, the orientation of the organic molecule in its host crystal can be ascertained, and, by using different host crystals, the effects of the crystalline field can be determined. The value of D and E reveal the nature, as well as the magnitude, of the excited state internal molecular forces. The paramagnetic hyperfine spectrum, which also can be observed in these molecules when resolution permits, is correlated with the "spin densities" of the unpaired electrons in the excited state.

SUMMARY AND CONCLUSIONS

A cryostat (dewar) has been designed and constructed so that it has all of the features illustrated schematically in Fig. 1 and also fulfills the following technical conditions:

1. The sample should be adequately cooled at the liquid nitrogen temperature when irradiated by the incident light.
2. The sample and the surrounding microwave cavity should be free from mechanical vibration.
3. The microwave magnetic field should be perpendicular to the steady magnetic field as the latter changes its orientation.
4. The conditions of light excitation should not be changed by the rotation of the steady magnetic field.
5. There should be a provision for observing the fluorescent light perpendicular to the direction of the incident light.

All of the above conditions are found to be satisfactorily fulfilled after a test of the performance of the completed cryostat. Preliminary observations of the photoexcited napthalene in durene crystal have been found to agree in all details with the spectra originally observed by C. A. Hutchison, Jr. and B. W. Mangum in their pioneering work (Ref. 1). More observations are being made to check the feasibility of detecting the electron spin resonance (excited by microwaves as before) by measuring the change in intensity of the circularly polarized component of the phosphorescent light emission.

FUTURE PLANS

Work is continuing on this project. Efforts will be made to observe the paramagnetic spectrum of the lowest excited triplet state of the anthracene molecule in a terphenyl host crystal. If the lifetime of this molecule proves too short to use paramagnetic detection, microwave pumping and optical detection will be used to examine the resonance. An attempt will also be made to observe a Zeeman double quantum transition in a naphthalene molecule imbedded in a durene host crystal.

REFERENCES

1. C. A. Hutchison, Jr. and B. W. Mangum, "Paramagnetic Resonance in Naphthalene in its Phosphorescent State," J. Chem. Phys., Vol. 34, No. 3, 1961, pp. 908-922.
2. D. S. McClure, "Electronic Spectra of Molecules and Ions in Crystals," Solid State Physics, Vol. 8, 1959, pp. 1-47.

FUNDAMENTAL RESEARCH V/2
Plasma Dynamics Research X82CPR
Support: Task X/NOw 62-0604-c
R. Turner
January - June 1965

THETA-PINCH PLASMA SOURCE

Most plasma sources used for injection and confinement studies have one or more undesirable features: (a) the impurity level is too high, (b) the neutral gas content of the plasma is too large, or (c) the plasma has a long, low-energy component. Experiments are being continued with a small fast theta-pinch using programmed magnetic fields to produce a dense, hot plasma which, hopefully, will not be as seriously troubled by these disadvantages. The gun's configuration and principles of operation have been described in a previous quarterly report (Ref. 1).

SUMMARY

The gun previously described has been modified to improve preionization, reduce the neutral gas ahead of the output plasma, and to improve the magnetic guide field. The gun now produces a single short pulse of helium plasma with a maximum velocity of 4×10^7 cm/sec, and a maximum transverse energy density (17.5 cm from the pinch region) of 0.3 J/cm. Shot-to-shot reproducibility is presently unsatisfactory. Magnetic probe and photographic measurements indicate that the plasma may become unstable as it leaves the pinch region and may hit the wall between the gun and guide field. An instability or wall contact could easily result in the poor reproducibility and also reduce output.

FUTURE PLANS

The immediate concern is with the lack of reproducibility of output between successive firings of the gun and whether this results from an instability or wall contact. In addition, a continuing effort will be made: (a) to find the conditions for maximum energy output with minimum pulse length, and (b) to determine the plasma density, temperature, and total energy more accurately. An ion and photon energy analyzer has been built and will be installed in the next quarter. A comparison between the actual output and the output predicted by a French hydromagnetic model (Ref. 2) has been started.

DISCUSSION

When the theta-pinch gun was fired into a longitudinal magnetic field of several kilogauss, it produced a single short pulse with a maximum velocity of 10^7 cm/sec, a maximum transverse energy density of 0.25 J/cm, and a particle density of only 10^{12}/cc. Although this output was two to four times greater than the output of a single coil conical pinch gun having 80 percent of the energy of both coils,

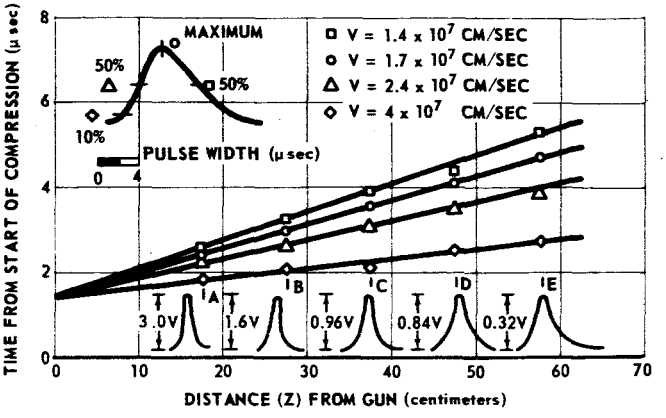

Fig. 1 Plasma Position along Guide Field versus Time. (76587)

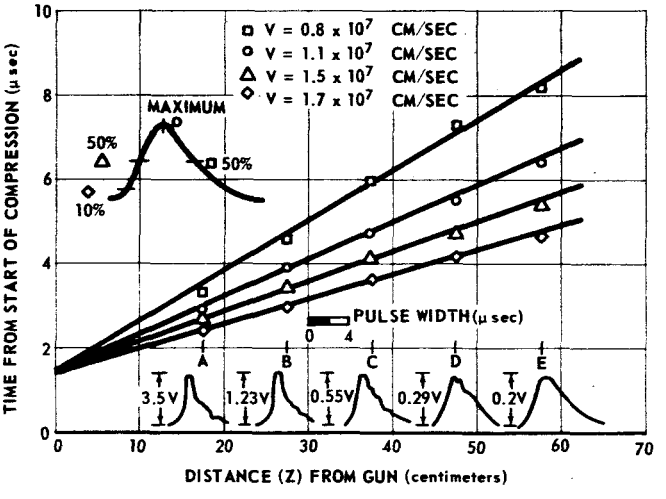

Fig. 2 Plasma Position along Guide Field versus Time. (76588)

there were indications that the plasma was hitting the wall between the gun and guide field and limiting its output. The gun was modified to remove this and other possible sources of trouble. In addition, the method of preionization was changed from an axial discharge to a low-energy discharge through the pinch coils preceding the main discharge, the distance from the gas valve to the pinch region was decreased, and the gas valve power supply was improved. A larger, more uniform guide field was also added. So far, these changes have only produced a slight increase in output.

The output is still critically dependent on the initial gas pressure and is far from reproducible. Magnetic probe measurements indicate that the plasma may still be too close to or hitting the wall between the gun and guide field. High-speed photography indicates that the plasma may be unstable as it leaves the pinch region.

Figure 1 is a plot of distance along the guide field versus time derived from one of the fastest and narrowest output pulses measured. At loop A (17.5 cm from the pinch region) the plasma has a maximum transverse energy density of 0.3 J/cm, which decreases to 0.03 J/cm at loop E (57.5 cm from the pinch region). The total transverse energy and energy density decrease by about 2:1 between loops B and D (a distance of 20 cm). Figure 2 is a similar plot for a more typical output. It is slower, longer, and has a lower energy density, but more total transverse energy. The relative shapes of the measured magnetic loop signals are shown on each figure.

The immediate concern is whether a wall interaction, instability, or variable gas input is responsible for the lack of reproducibility between shots.

REFERENCES

1. R. Turner, "Theta-Pinch Plasma Source," Section V/2b, Research and Development Programs Quarterly Report, October-December 1964, APL/JHU U-RQR/64-4.

2. F. Wallbroeck et al., Nuclear Fusion, 1962 Supplement, Part 2, p. 675.

FUNDAMENTAL RESEARCH V/3
Hypersonic Gun Tunnel Studies X82BFM, A53BFM
Support: Task X/NOw-62-0604-c and RRRE (BuWeps)
R. A. Makofski and R. W. Henderson
April - June 1965

HYPERSONIC GUN TUNNEL

The hypersonic gun tunnel is a relatively inexpensive means for providing uncontaminated air flows suitable for testing hypersonic ramjet inlet models. The apparatus uses unheated, high-pressure gas to compress a smaller volume of air to high temperatures and pressures by means of both shock wave and isentropic flow processes. The engineering application to inlets is of immediate interest; however, the instruments can also be used as a research tool for investigating fundamental flow problems, boundary-layer interaction, flow near the leading edge of blunt bodies, and configuration problems at high Mach numbers.

SUMMARY

The majority of the tests during this period were preliminary studies of the flow about different configurations for the purpose of developing future testing techniques. These tests have, in themselves, provided useful information. In one such run, a plexiglass wedge (11.5° wedge angle, 0.002-inch leading edge) was tested to determine the feasibility of using such materials for inlet models. Examination of the wedge after the run indicated no measurable difference in leading edge thickness, but a slight discoloration was noted on the compression surface downstream of Station 2 (Fig. 1). The schlieren photo (Fig. 1) also shows a definite thickening of the boundary layer downstream of this station, suggesting a transition from laminar to turbulent flow. This is further borne out by the comparison of the local Mach number and Reynolds number at Stations 2 and 2.5 with the transition Reynolds number data of Ref. 1 (Fig. 2).

Figure 3 is a schlieren photograph of the interaction between an incident shock wave and a laminar boundary layer. The intersection of the two leading shock waves may be seen as well as the resulting slip line. The incident shock wave strikes the boundary layer causing it to thicken, and a shock is formed upstream of the interaction. An expansion occurs in the region in which the incident shock strikes the boundary layer causing the flow to turn towards the surface and reattach. Another shock wave forms in the reattachment zone. Measurements indicate an interaction length of more than ten boundary layer thicknesses or about 20 percent of the distance from the leading edge to the beginning of the interaction.

The disturbance occurring at the mid-chord point of a cone, as described in the previous progress report (Ref. 2), has been traced to a blockage effect caused by the sting support. Replacement of this support by a simpler design having less blockage eliminated the disturbance.

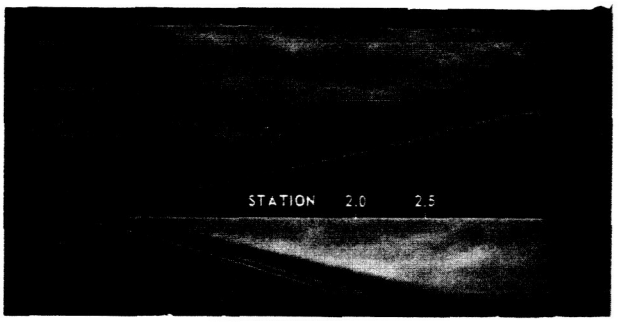

Fig. 1 Schlieren Photograph of 11.5° Plexiglass Wedge in Hypersonic Gun Tunnel.
M ≃ 12, Leading Edge Thickness ≃ 0.002 Inch, Free-Stream Reynolds No. ≃ 1.3 x 10^6/ft, Tunnel Supply Pressure = 720 Atmospheres. (76505)

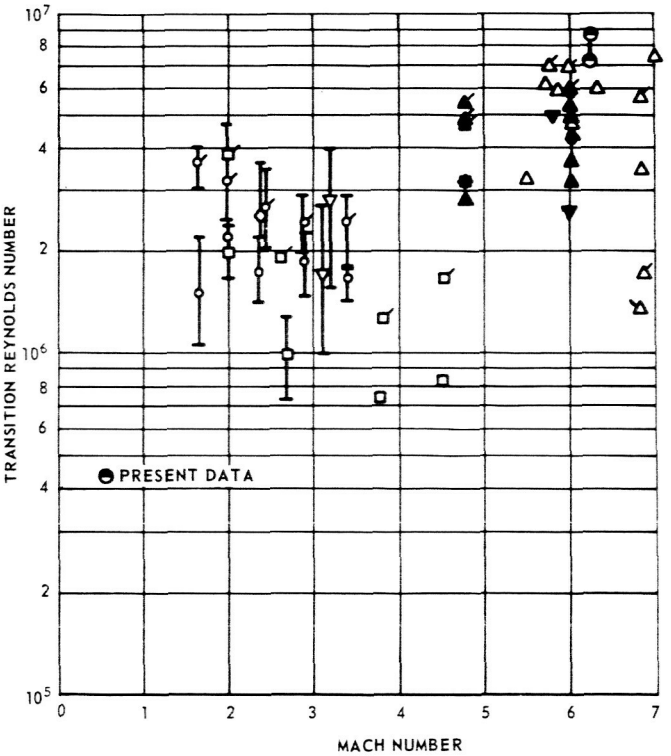

Fig. 2 Transition Reynolds Number as a Function of Mach Number. (This Figure Is Taken from Fig. 3 of Ref. 1.) (76506)

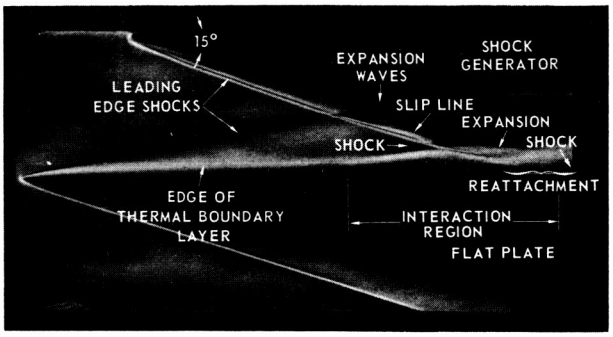

Fig. 3 Schlieren Photograph of Incident Shock Wave-Laminar Boundary Layer Interaction in Hypersonic Gun Tunnel. Mach ≃ 12. Leading Edge Thickness of Flat Plate ≃ 0.009 Inch, Leading Edge Thickness of Shock Generator ≃ 0.012 Inch, Free-Stream Reynolds Number ≃ 1.1×10^6/ft, Tunnel Supply Pressure = 480 atmospheres. (76507)

FUTURE PLANS

The fabrication of the contoured nozzle should be completed and calibrations under way. Further studies of inlet models and other basic shapes will be continued using the present nozzle.

BACKGROUND

The gun tunnel is a relatively inexpensive means of obtaining flows with an enthalpic content greater than available in a conventional wind tunnel. Although a shock tunnel is capable of even higher enthalpies, the gun tunnel has longer testing times than are available in a shock tunnel (2-40 milliseconds versus the order of a few milliseconds in a shock tunnel). The longer running time permits the study of phenomena requiring a finite amount of time to reach equilibrium and allows the use of more economical, commercially-available instrumentation in the experimental programs. Also, the use of a piston in the gun tunnel effectively separates the driver and driven gases preventing the loss of test gas through the interface and the consequent reduction in test time. These advantages have already been demonstrated by gun tunnels in operation in England (Refs. 3 and 4) and Sweden (Ref. 5).

DISCUSSION

One possible means of determining the gun tunnel stagnation temperature is by measurement of the stagnation point heat transfer rate and through theory, e.g. Fay-Riddel (Ref. 6), to infer the stagnation temperature. Previous attempts to apply this method using thin film resistance gauges made of platinum were unsuccessful. This failure was attributed to the high film temperatures which occurred by virtue of the longer tunnel running time and high heat transfer rates and erosion of the gauge. For this reason, subsequent efforts have been directed towards development of a resistance calorimeter employing 0.001-inch platinum foil. Even in this case, the foil temperatures are sufficiently high to require detailed calibration to obtain such properties as thermal conductivity, specific heat, and the thermal coefficient of resistance at temperatures above 100°C. These calibrations are presently under way.

The schlieren system has been adapted for use with a high-speed motion picture camera. To avoid triggering difficulties, the double-diaphragm technique described in Ref. 7 was used. No serious difficulties were encountered with this method.

REFERENCES

1. Paul F. Holloway and James R. Sterret, Effect of Controlled Surface Roughness on Boundary Layer Transition and Heat Transfer at Mach Numbers of 4.8 and 6.0, NASA TN D-2054, April 1964.
2. R. A. Makofski and R. W. Henderson, "Hypersonic Gun Tunnel," Section V/4, Research and Development Programs Quarterly Report, January-March 1965 (Unclassified), APL/JHU U-RQR/65-1.
3. K.N.C. Bray, "An Evaluation of the Hypersonic Gun Tunnel," Hypersonic Flow Research, Progress in Astronautics and Rocketry, Vol. 7, October 1961.
4. R. N. Cox and D. F. T. Winter, The Light Gas Hypersonic Gun Tunnel at A.R.D.E., Fort Halstead, Kent, AGARD Rept. 139, July 1957.
5. Bo Lemcke, "An Investigation of the Stagnation Conditions in the Shock Compression Heater of a Gun Tunnel," Flygtekniska, Forsoksanstalten, Stockholm, FFA Rept. 90, February 1962.
6. J. A. Fay and F. R. Riddel, "Theory of Stagnation Point Heat Transfer in Dissociated Air," J. of Aero. Sciences, Vol. 25, No. 2.
7. R. A. Makofski, "Hypersonic Gun Tunnel Construction" (Unclassified), Section V/20 and "Hypersonic Gun Tunnel Performance Analysis" (Unclassified), Section V/21, Aeronautics Division Quarterly Review (Confidential), APL/JHU SR 7-3, October 1963.

Section VI
SPECIAL LABORATORIES

Environmental Test Laboratory Operation--The Environmental Test Laboratory is equipped with a wide variety of vibrational, thermal, and vacuum equipment for studying environmental effects on the performance of missiles and satellites and their components. Recently, the mechanical stability of the 10,000-pound-force vibration test equipment was improved (VI/2).

SPECIAL LABORATORIES V1/2
Environmental Test Laboratory Operation Y1FBBE
Support: BuWeps on a Use/Cost Basis
I. B. Irving
April - June 1965

ENVIRONMENTAL TEST LABORATORY

The Environmental Test Laboratory (ETL) supports the engineering development and flight-testing program for missiles and satellites at APL and conducts research and development work in instrumentation related to environmental simulation, testing, and protection.

SUMMARY

The mechanical stability of the 10,000-pound force vibration test facility has been improved. An 80,000-pound reinforced concrete mass was poured as a base mount for the shaker and a new "Team" horizontal vibration table. The new table reduces the mechanical cross coupling to the item under test by a substantial amount, thereby improving the accuracy of vibration simulation and increasing the ability to measure the effects of unilateral specimen simulation. This increased stabilization of the system is a protection to the facility and also to the items under test.

FUTURE PLANS

Future plans for the vibration laboratory include the modification of the automatic spectrum density equalizer-analyzer for more reliable operation in random vibration testing and an increase from 12 channels to 36 channels of vibration data recording instrumentation from the Test Laboratory to the BID Data Processing Center. Plans for the space simulation center include proportionate temperature controls for more accurate orbital heat flux exchange simulation.

BACKGROUND

The Environmental Test Laboratory is continually revising its test procedures and practices to keep abreast of the state-of-the-art. It is equipped to perform package level and payload testing on satellites in the simulated environments of space, launching, shock, vibration, and acceleration. These same instruments are also used in the testing of components and systems for the Talos, Terrier, and Standard Missile programs. Instrumentation includes lines to the APL Ground Station for tape recordings and data analysis.

REVIEW OF INSTALLATIONS AND EXPERIMENTS

The "Team" table now installed and in operation is shown connected to the 10,000 pound force vibrator in Fig. 1. Vibration test specifications require that a specimen be vibrated along each of three mutually perpendicular axes. The size and shape of the units to be tested restrict the use of the head of the shaker in its normally vertical position to vibration along only one axis. The slippery table ("Team"), placed in front of the shaker operating at 90° from the vertical, permits the testing of large or heavy speci-

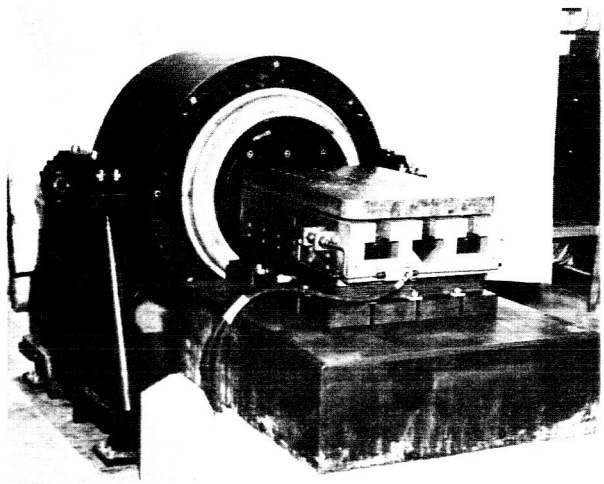

Fig. 1 Team Table Connected to 10,000 Pound Force Vibrator. (76530)

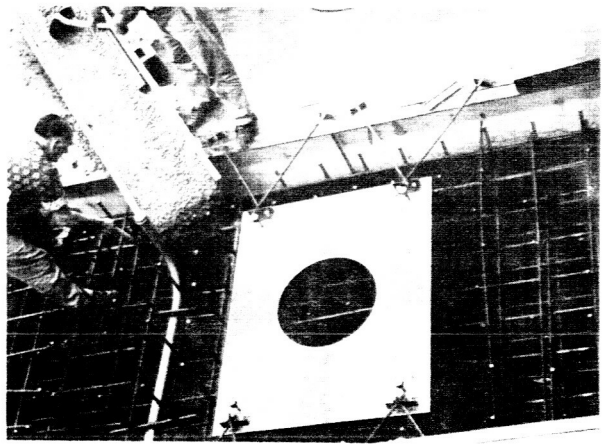

Fig. 2 Pit Being Filled with Concrete. (76531)

mens. The disadvantage of previously used systems of this type were low frequency resonances caused by instability in the mounting and a long coupling link between shaker and slip table as well as high amplitude mechanical cross vibration of the slip table itself. The new unit has been placed on an integral mount with the shaker. This mount is isolated from the surrounding floor and consists of a mass of concrete and reinforcing steel 6 feet deep weighing approximately 80,000 pounds. This pit, being filled with concrete is shown in Fig. 2.

The tracks of the Team table have a 0.001 inch clearance and ride on a slick of oil injected at about 3000 psi. The natural frequency of the system was measured with a balanced 100-pound load. It resonates at 1750 cps showing a mechanical gain of 6 vertically and 1.5 horizontally. This frequency will shift slightly (1250 to 1900 cps) with variations in load and balance, but the mechanical amplitudes of the cross coupling will stay reasonably constant. No measurable low frequency (below 100 cps) cross movement was observed.

This table was first used near the end of June to test the 380-pound GEOS satellite prototype unit with excellent results. Its use is planned for all future satellites.

Section VII
SPECIAL ASSIGNMENTS

Advanced ALBIS--The statistical problem of detecting targets in the background of receiver noise and surface clutter has been solved analytically, and the numerical solutions of the resulting complicated mathematical expressions have been obtained for a number of important specific cases (VII/2).

Plasma Dynamics Research--Fabrication of parts for construction of the multipole field in which to confine a plasma flow and investigate its interaction with the field is nearly complete (VII/4).

SPECIAL ASSIGNMENTS VII/2
Advanced ALBIS Z12BBD
Support: ARPA
E. Shotland
April - June 1965

STUDIES OF TARGET DETECTION BY PULSED RADAR IN A BACKGROUND OF SEA CLUTTER

The detection of targets in the background of land or sea clutter constitutes one of the most difficult problems of search radars. In all cases where the relative target versus radar velocities differ markedly from the relative scatterer versus radar speeds, doppler methods and MTI techniques can be successfully applied to discriminate the target from its background. However, whenever the relative target versus radar velocity occurs at right angles to the line of sight--a situation often encountered when the target flies straight up--the cited methods do not help. Moreover, no appropriate theory is available by means of which this statistically difficult problem can be satisfactorily analyzed. The efforts of the present work were directed toward filling this gap of knowledge.

SUMMARY AND CONCLUSIONS

The statistical problem of target detection in the background of receiver noise and surface clutter was solved in analytical form (Refs. 1 and 2). The mathematical expressions of the results are quite complicated and cumbersome, and a great deal of numerical work is necessary for obtaining practical data. This job has been accomplished for specific, important cases (Figs. 1, 2, 3, and 4).

FUTURE PLANS

It is planned to continue the analytical and computational work pertaining to the general case of radar detection in the background of clutter and to compile the results in tabular and graphical form. This information will be documented in an APL report.

BACKGROUND

J. I. Marcum in a classical paper (Ref. 3) applied the statistical method of Neyman-Pearson to the radar detection theory. The basic objective of this method is to provide an optimum criterion for testing a statistical hypothesis. In the search-radar case, the supposition to be examined is: "a hostile target is present." Marcum solved the problem for targets of fixed magnitude in the environment of flat, wide-band receiver noise. P. Swerling (Ref. 4) extended Marcum's theory to fading targets. The latter are classified into four categories by means of two properties: time rate of fading and statistical distribution of signal magnitude.

However, in general, clutter generates its own characteristic power spectrum which behaves neither like a fading target nor like flat receiver noise. Therefore, the Marcum-Swerling theories are not strictly applicable to the environment of clutter.

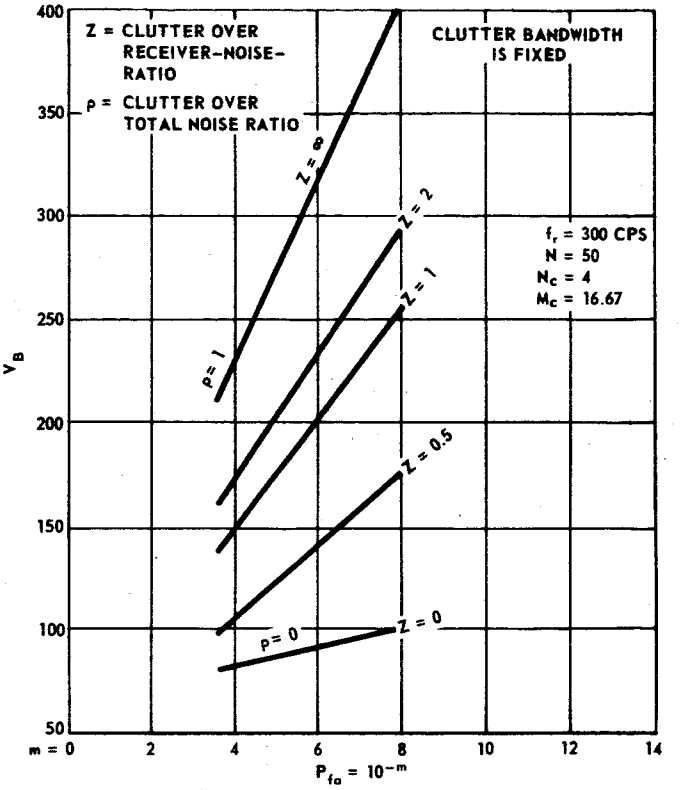

Fig. 1 Threshold Setting (V_B) in Terms of Mean Square Input Noise versus False-Alarm Probability (P_{fa}) for Various Z. (76549)

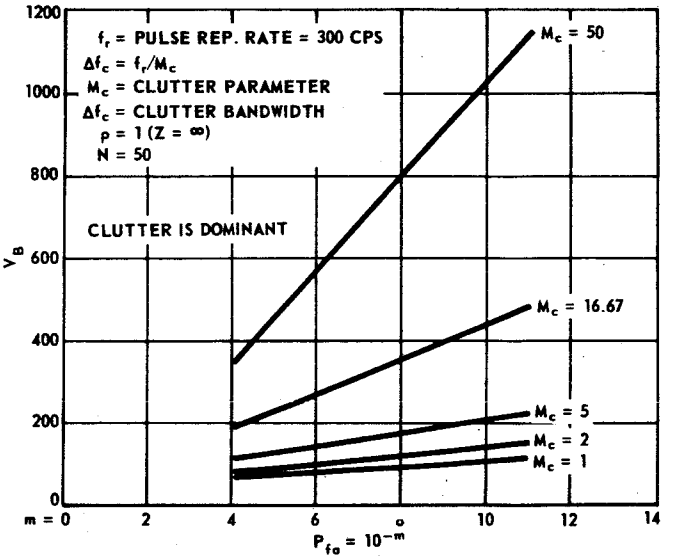

Fig. 2 Threshold Setting (V_B) in Terms of Mean Square Input Noise versus False-Alarm Probability (P_{fa}) for Various Clutter Spectra. (76550)

DISCUSSION

In the present work, a general theoretical model of search radar inputs is introduced which contains the five Marcum-Swerling categories as special cases. Let K represent any general type of input. In a particular case reference is made to one or more targets, receiver noise, land clutter, sea clutter, etc.

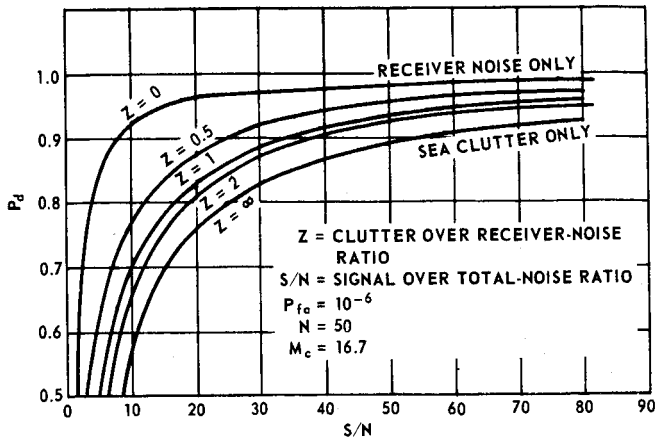

Fig. 3 Detection Probability (P_d) for Target Signal (S) and Total Noise (N). (76551)

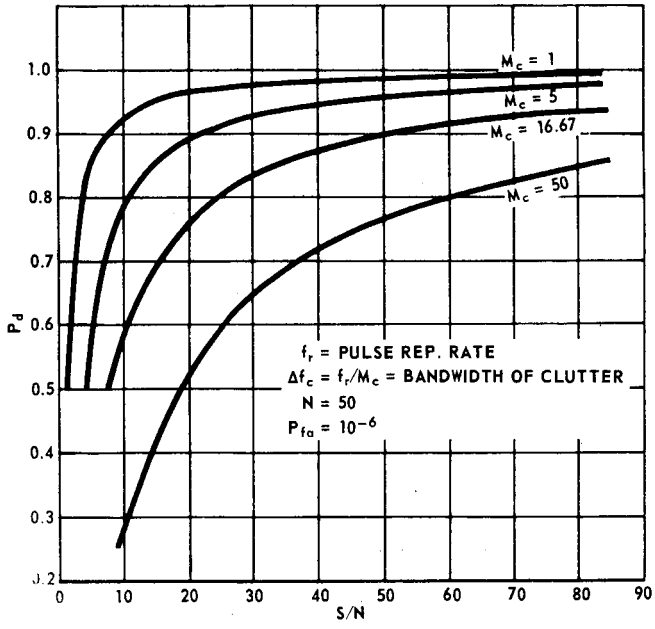

Fig. 4 Detection Probability (P_d) versus Target Signal and Sea Clutter for Various Clutter Spectra. (76552)

Then the general input model can be characterized by a set of coupled numbers:

$$- - - - - - - , (N_K, n_K), - - - - - - - .$$

The first number, N_K, essentially refers to the spectral width of the object (time rate of fading); the second number n_K pertains to its type of signal power distribution. The mathematical problem was solved by generating the characteristic function of the probability density of the total radar signal at the input of the threshold or decision-making device. Besides the numbers (N_K, n_K), the following parameters play an important role. They represent the mean-square voltage component at the input of the detector:

σ_R^2 (for receiver noise),

σ_T^2 (for target signal), and

σ_c^2 (for clutter).

The derived quantities used follow:

$$x = \frac{\sigma_T^2}{\sigma_R^2}$$ (a conventional parameter),

$$z = \frac{\sigma_c^2}{\sigma_R^2}$$ (a new clutter parameter),

$$\rho = \frac{\sigma_c^2}{\sigma_c^2 + \sigma_R^2} = \frac{Z}{1 + Z}$$ (an alternate clutter parameter)

$$S/N = \frac{\sigma_T^2}{\sigma_c^2 + \sigma_R^2}$$ (total signal-over-noise ratio).

The four attached figures present the results of sample calculations in a specific search-radar case. The following additional symbols are used:

$N = N_c \times M_c$	=	Number of pulses integrated during dwell time,
M_c	=	Number of correlated clutter pulses,
N_c	=	Number of uncorrelated clutter groups during dwell time,
f_R	=	Pulse repetition frequency,
$\Delta f_c = \frac{f_R}{M_c}$	=	Clutter bandwidth,
V_B	=	Voltage bias or threshold setting normalized to the total mean-square input noise,
$P_{fa} = 10^{-m}$		False alarm probability,
p_d	=	Single-scan detection probability.

The first two figures depict the threshold setting versus the false-alarm probability for various clutter parameters; the last two figures show the detection probability versus S/N ratio for various clutter parameters.

REFERENCES

1. E. Shotland, "False-Alarm Probabilities for Receiver Noise and Sea Clutter," APL/JHU BBD-1387, 27 October 1964.
2. E. Shotland, "Studies of Target Detection by Pulsed Radar in the Environment of Sea Clutter," APL/JHU BBD-1412, 2 March 1965.
3. J. I. Marcum, A Statistical Theory of Target Detection by Pulsed Radar, Rand Corporation Research Memorandum RM-754, 1 December 1947.
4. J. I. Marcum and P. Swerling, "Studies of Target Detection by Pulsed Radar," IRE Trans. Vol. IT-6, No. 2, April 1960.
5. L. F. Fehlner, Marcum's and Swerling's Data on Detection by a Pulsed Radar, APL/JHU TG-451, 2 July 1962. (Appendix by R. G. Roll and G. T. Trotter.)

SPECIAL ASSIGNMENTS VII/4
Plasma Dynamics Research Z16CPR
Support: NASA
W. Garten, Jr., S. J. Moss, and T. R. Whyte
April - June 1965

PLASMA FLOW IN A MULTIPOLE FIELD

The flow of ionized gas (plasma) and its interaction with magnetic fields are basic areas of plasma research. Control of the state of the plasma, its direction of flow, and its purity are among the broad applications of knowledge in these areas. Specifically, this experiment is concerned with measuring the behavior of a plasma as it enters and flows along the "magnetic channel" created by a multipole magnetic field. Measurements will be made to determine changes in the density and energy of the plasma as it moves down the field and to determine local plasma-field interactions, i.e., electric fields, evidence of turbulent flow, and loss of particles from the stream.

SUMMARY AND CONCLUSIONS

Fabrication of parts for the multipole field assembly is nearly completed. Final assembly will begin once all parts are available. Continued study of the conical gun has included setting up the computation of plasma parameters from magnetic loop data. Initial attempts fo find correspondence of experimental data with these computations have been successful.

FUTURE PLANS

Measurement of the conical theta-pinch gun performance will continue. Once fabrication of the multipole field is completed, tests of the field and its power supply will be carried out. When the gun and the multipole field are ready, studies will be made of the plasma flow in this field at several density-particle energy conditions. If necessary, the theta-pinch gun will be used to extend the available range of conditions.

DISCUSSION

The multipole-field assembly has been designed and most of its parts fabricated (Fig. 1). The outer vacuum wall will be glass, permitting direct optical measurements in the plasma region. The main conductors are of aluminum. This choice of material was made in favor of the greater yield strength of aluminum as against the approximately 25 percent less skin depth for copper conductors. Power for the multipole field will come from 20 kv capacitors coupled to the field conductors through a step-down transformer. The transformer and capacitors are on hand and will be tested with the multipole field assembly when it is available.

Concurrently, the conical gun has been under study to determine its characteristics, such as plasma temperature, density, velocity, etc. A crowbar circuit has been added to the gun since the last report. This prevents current reversal after the second half cycle. This then provides one primary plasma puff which, it has been determined, leaves the gun near the second current maximum.

The analysis being carried out to determine plasma parameters follows closely the work of Waelbroeck et al (Refs. 1 and 2) where the plasma is considered to obey the hydromagnetic equations and have a Gaussian-like distribution of linear particle density. From the signals induced by the plasma in magnetic loops as it passes along the field of a solenoid, this model allows the extraction of the above mentioned parameters.

In an initial test of this model, a third half-cycle plasma puff was analyzed. Emphasizing again that these data are only preliminary, indications are that the fits to the

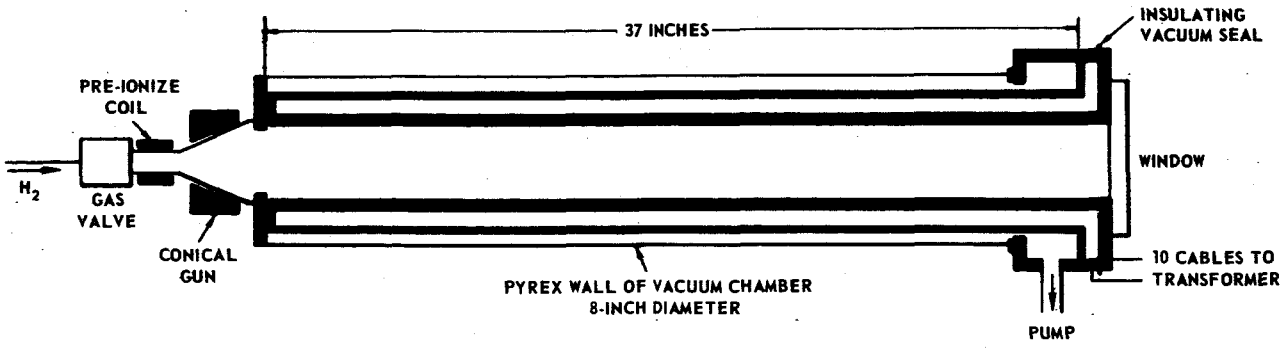

Fig. 1 Multipole Field Apparatus. (76557)

data are good. Some order of magnitudes are listed below:

T_{ion} = 30,000°K,

V_o = 7.2×10^6 cm/sec, and

n = $\sim 10^{16}$ cm^{-3},

where:

T_{ion} = ion temperature,

V_o = velocity of center of mass of puff, and

n = number density of ions.

In the experiment to be performed, the second half-cycle puff will be used, and it is expected that, because of the presence of trapped field, this puff should have considerably higher temperature than the above mentioned, while the velocity of the center of mass should be smaller by a factor of approximately two.

A large portion of this analysis has been carried out with the aid of a computer, and only preliminary results are now available. When this work is completed, an attempt will be made to extend this method to the more complicated configuration of the multipole field.

REFERENCES

1. J. Jacquinot, C. LeLoup, and F. Waelbroeck, Analyse Boucles Magnetiques Compensees, Euratom Report EUR-CEA-FC-217, July 1963.
2. J. Jacquinot, C. LeLoup, J. F. Poffe, and F. Waelbroeck, Analyse Boucles Magnetiques Compensees, Euratom Report EUR-CEA-FC-218, July 1963.

INITIAL DISTRIBUTION EXTERNAL TO THE APPLIED PHYSICS LABORATORY*

The work reported in U-RQR/65-2 was done under Bureau of Naval Weapons Contract NOw-62-0604-c.

APL Task	Supporting Agency	APL Task	Supporting Agency	APL Task	Supporting Agency
A22	BuWeps, RM-2	A42	BuWeps, RMMO	X81	NOw-62-0604-c
A32	BuWeps, RMGA	A62	BuWeps, RMWC	X82;A53	BuWeps, RRRE NOw-62-0604-c
A33	BuWeps, RMGA	P61	Special Projects Office, SP-001	Y1F	Use/Cost
A34	BuWeps, RMGA	R11	ARPA	Z16	NASA
A35	BuWeps, RREN-4 RMGA-8				

ORGANIZATION	LOCATION	ATTENTION	No. of Copies
DEPARTMENT OF DEFENSE			
Dir., Defense Research/Engineering	Washington, D. C.	Technical Library	1
Dir., WSEG	Washington, D. C.		1
Dir., ARPA	Washington, D. C.		1
DDC	Alexandria, Va.		20
Department of the Navy			
Department Offices			
CNO	Washington, D. C.	OP-03EG	1
		OP-34	1
		OP-07T15	1
		OP-701	1
Chief, BuWeps	Washington, D. C.	A-1	1
		DLI-31	2
		F-1	1
		FWAM-2	1
		N	1
		NPMS-35	1
		PWS	1
		R-1	1
		R-12	1
		R-14	1
		RAAE	1
		RM/RM-54	1
		RM-2	1
		RM-3/RMLG	1
		RM-11/RM-12	1
		RMGA	1
		RMGA-8	1
		RMMO	1
		RMMP	1
		RMWC	1
		RREN	1
		RRMA	1
		RRRE	1
		RSWI	1
		SP-00	1
		SP-001	1
		SP-20	1

*Initial distribution of this document within the Applied Physics Laboratory has been made in accordance with a list on file in the APL Technical Reports Group.

INITIAL DISTRIBUTION EXTERNAL TO THE APPLIED PHYSICS LABORATORY

ORGANIZATION	LOCATION	ATTENTION	No. of Copies
Department of the Navy (Cont'd)			
Department Offices (Cont'd)			
Chief, BuWeps	Washington, D. C.	SP-24	1
		SP-43	1
Chief, NavPers	Washington, D. C.	Pers C-123	1
Chief, NavRes	Washington, D. C.	429	1
Commandant, USMC	Washington, D. C.	G-3	1
Naval Attache	F.P.O., New York, N. Y.	Navy No. 100	1
BuWeps Flt Read Rep Lant	Norfolk, Va.		1
BuWepsRep	Silver Spring, Md.		1
BuWeps Flt Read Rep Cent	WPAFB, Dayton, O.		1
BuWepsRep	Mishawaka, Ind.		1
BuWepsRep	Minneapolis, Minn.		1
BuWeps Branch Rep/OAL	Daingerfield, Tex.		1
BuWeps Branch Rep/Pacific	San Diego, Cal.		1
Laboratories			
NOL	White Oak, Md.	Library	1
NRL	Washington, D. C.	2027	1
		463	1
NWL	Dahlgren, Va.	Library	1
NEL	San Diego, Cal.	Library	1
NOL	Corona, Cal.	Doc. Library	3
Facilities			
NPP	Indian Head, Md.	TEL	1
EODF	Indian Head, Md.		1
DTMB	Washington, D. C.	Aerodyn. Lab. Lib.	1
NOMTF	WSMR, N. M.		1
NOTS	China Lake, Cal.	Tech. Library	3
Naval Shipyard	Long Beach, Cal.	Design Divis.	1
NSMSES	Port Heueneme, Cal.		5
Mare Is. Nav. Shipyard	Vallejo, Cal.	Design Divis.	1
Puget Sd. Nav. Shipyard	Bremerton, Wash.	290	1
Schools			
Naval Guided Missile School	Dam Neck, Va.	Library	1
U. S. Naval Academy	Annapolis, Md.	Weapons Dept.	1
Pac. Flt. Training Command	San Diego, Cal.	MISTRAUPAC	1
Naval Postgraduate Sch.	Monterey, Cal.		1
Mare Is. Nav. Schs. Com.	Vallejo, Cal.	Guided Missile Sch.	1
Centers			
Naval Training Devices	Port Washington, N. Y.	Tech. Library	1
NWSO/NAEC	Philadelphia, Pa.		1
NAMC	Philadelphia, Pa.	NAEF (SI)	1
NADC	Johnsville, Pa.	Library	1
Flt. Antiair Warfare Trng. Ctr.	San Diego, Cal.		1
NMC	Pt. Mugu, Cal.	Tech. Library (NO 322)	2
Task Forces			
ComOpTevForLant	Norfolk, Va.		1
ComServForLant	Norfolk, Va.		1
ComOpTevForPac	San Diego, Cal.		1
Department of the Air Force			
Department Offices			
Chief of Staff	Washington, D. C.	AFRST-AS	1
System Command/STLO	Washington, D. C.	RTSAW	1
Laboratories			
Project Rand	Santa Monica, Cal.		1

INITIAL DISTRIBUTION EXTERNAL TO THE APPLIED PHYSICS LABORATORY

ORGANIZATION	LOCATION	ATTENTION	No. of Copies
Department of the Air Force (Cont'd)			
Centers			
Rome Air Dev. Ctr. (RAALD)	Griffiss AFB, Rome, N. Y.	Doc. Library	1
Arnold Engg. Dev. Ctr.	Tullahoma, Tenn.	AEYD	1
Air Proving Grd. Ctr. (PGBPS-4)	Eglin AFB, Valparaiso, Fla.		1
Aeronaut. Chart and Info. Ctr.	St. Louis, Mo.	ACOC	1
AFWL (WLIL)	Kirtland AFB, Albuquerque, N. M.		1
Commands			
HQ, Tactical Air Command (DORQ-M)	Langley AFB, Hampton, Va.		1
Foreign Technology Division	WPAFB, Dayton, O.	TD-Bla, Library	1
Systems Engineering Group (RTD)	WPAFB, Dayton, O.	SEPIR	1
Air Univ. Library	Maxwell AFB, Montgomery, Ala.		1
Continental Air Defense Com.	Ent AFB, Colo. Spgs., Colo.	Directorate of Systs.Dev.	1
Department of the Army			
Offices			
Assistant Secretary/R and D	Washington, D. C.		1
Assist. Chief of Staff/Intell.	Washington, D. C.	R and D Branch	1
Laboratories			
Harry Diamond Laboratory	Washington, D. C.	AMXDO-TIB	1
Engg. R and D Labs	Ft. Belvoir, Va.	Tech. Docs. Ctr.	1
Army Research Office, Duke U.	Durham, N. C.	CRD-AA-IP	1
Nuclear Group, ACDC	Ft. Bliss, Texas		1
Electronics R and D Activity	WSMR, N. M.	SELWS-W	1
Electronics Laboratory	Mountain View, Cal.		1
Facilities			
Aberdeen Proving Ground	Aberdeen, Md.	Library	1
Tank-Automotive Ctr.	Detroit, Mich.	SMOTA-RCS-1	1
Redstone Scientific Info. Ctr.	Huntsville, Ala.	Chief, Docs. Section	5
Commanding General, WSMR	WSMR, N. M.	Technical Library	1
Electronic Proving Ground	Ft. Huachuca. Ariz.	Technical Library	1
Arsenals			
Picatinny Arsenal	Dover, N. J.	Tech. Info. Agency	1
Rock Island Arsenal	Rock Island, Ill.	SWERI-RDI, Doc. Sect.	1
Schools			
Army War College	Carlisle, Pa.	Library	1
Agencies			
Materials Research Agency	Watertown, Mass.	Tech. Info. Ctr.	1
Signal Air Def. Engg. Agency	Ft. Meade, Md.		1
Armor Combat Devel. Agency	Ft. Knox, Ky.		1
Artill. Combat Devel. Agency	Ft. Sill, Okla.		1
Air Defense Combat Devel. Agy.	Ft. Bliss, Tex.		1
U. S. GOVERNMENT AGENCIES			
Security Agencies			
Central Intell. Agency	Washington, D. C.	OCR Stand. Dist.	4
National Security Agency	Ft. Meade, Md.	C3/TDL	1

INITIAL DISTRIBUTION EXTERNAL TO THE APPLIED PHYSICS LABORATORY

ORGANIZATION	LOCATION	ATTENTION	No. of Copies
U. S. GOVERNMENT AGENCIES (Cont'd)			
National Aero. and Space Agy.			
Headquarters	Washington, D. C.	M. J. Aucremanne	4
Scientific and Tech. Info. Agency	Bethesda, Md.	S-AK/DL	1
Chief, Prop. Branch, Aero. Divis.	Washington, D. C.	RAP: N. Rekos	1
Atomic Energy Commission			
Headquarters Library	Washington, D. C.		1
Tech. Info. Extension	Oak Ridge, Tenn.		1
Mgr. AEC Albuquerque Operations	Albuquerque, N. M.		1
DASA Field Command/Sandia	Albuquerque, N. M.	Tech. Library	1